**UNIVERSITY OF CATANIA**

DEPARTMENT OF CHEMISTRY

INTERNATIONAL PhD IN CHEMICAL SCIENCES – XXX CYCLE

---

Alessandra Vittoria Bombace

# ToF-SIMS imaging and data mining approaches for organic structured samples

*PhD Thesis*

*Tutor:*

Prof. Antonino Licciardello

*PhD Coordinator*

Prof. Salvatore Sortino

# Index

# 1 Introduction

The research in the field of material science is fundamental, considering the variety of applications in scientific areas including nanotechnology, metallurgy, biomaterials, and cultural heritage. Many of the most urgent scientific problems that humans currently face, are related to the limits of available materials and how these can be used. Thus, material characterization and investigation are the key for the design and discovery of new structures, and for the advance understanding of causes of injury or damage of the systems.

Not only did the development of materials science permit the advancement of the technology, but these days it is also expanding its applications to the biomaterials field. Some clear examples are tissue engineering constructs, medical or dental implants, prostheses and devices and drug delivery[1]. As well as for technology, the characterization of these materials is essential for biocompatibility studies. Undoubtedly, the investigation of the materials' structures often requires the support of computer modelling and other advanced experimental methodologies[2]. However, breakthroughs in materials science are likely to significantly affect the future of technology and the chemical imaging characterization together with the computational science support can give a real contribution in this direction[3].

Scientists have long relied on the power of imaging techniques to help them see things invisible to the naked eye and thus achieve advance scientific knowledge. For instance, in medicine, techniques such as X-ray imaging and magnetic resonance imaging (MRI) have added a level of insight beyond traditional lab tests into the workings of the human body and identification of disease. But also, microscopy, which has been in use since the sixteenth century, is now powerful enough to detect and track single structures even inside living cells. Despite these innovations, today's demands on imaging have grown well beyond traditional "photographic" imaging.

The new frontiers in microelectronics, disease detection and treatment, as well as cultural heritage study and preservation demand an ability to visualize and understand molecular structures, chemical composition, and interactions and reactions in materials, even below micrometer order. In fact, in many areas, including new material development and understanding of cellular function in disease and health, the great steps forward will depend upon the development of new and innovative imaging techniques. Considering the growing interest towards micro- and nano- structure systems, the importance of high-sensitive techniques became evident, since they show at the same time high lateral resolution able to provide detailed information, but the molecular structure too.

Nowadays, there are new "less typical" scientific fields, which need the support of analysis and characterization techniques such as the cultural heritage field. As a matter of fact, heritage science is

a new interdisciplinary domain of scientific study of heritage, and it involves different human and social sciences, chemistry, biology and engineering disciplines. The term “heritage science” was coined in 2006 and it focuses on enhancing the understanding, care and safeguard of the cultural patrimony allowing it to enrich people's lives, not just today, but also for the future generations[4]. For this reason, material science research on objects of art and cultural heritage is developing fast, even though it presents many practical challenges, and it is still necessary to develop the best methodologies.

However, all the imaging techniques produce extensive quantities of data, categorized as big data, which need to be handled and interpreted. For this reason, the support of the computer sciences is necessary for the imaging data processing, and it is emerging as a novel and an innovative space in computing research and applications. The integration and interaction of the two broad fields of image processing and big data have already shown great potential in various areas[5,6]. Therefore, it is fundamental to enhance the computing applications applied on imaging techniques, in order to achieve a better interpretation and evaluation of the data.

More specifically, the study of systems containing spatially non-homogeneous composition requires the development of techniques able to provide laterally resolved molecular profiling (*3D imaging*). For a best interpretation and comprehension of matter properties, both chemical-physical and mechanical ones, it is fundamental that these analysis techniques pull molecular information out from the samples. As a result, scientists and engineers are constantly pushing the limits of technology in the pursuit of chemical imaging — the ability to visualize molecular structures and chemical composition in time and space — from the smallest dimension of a biological system to the widest expanse of a distant galaxy.

## 1.1 Imaging Techniques

A chemical image is a powerful tool able to yield the molecular information of both homogeneous and non-homogeneous systems, for each spatial coordinate of a sample. Among the techniques used to probe chemical structures we can find electron and X-ray microscopy techniques, and proximal probe techniques (force microscopy, near field, field enhancement), which can furnish a high spatial resolution but cannot give molecular information. Optical imaging techniques such as Raman, infrared [IR], and fluorescence ones and magnetic resonance technique (NMR) can detect the molecule structures or higher-order chemical systems providing chemical images[7]. In contrast to approaches which use higher- energy radiations (X-rays, electrons, etc.), these techniques allow largely non-destructive analyses both under *in vivo* or *in situ* conditions, even with soft matter.

However, they have several weaknesses. In fact, these techniques lack the inherent spatial resolution of the higher-energy approaches. More specifically, magnetic resonance is the lowest-energy method and it uses the longest-wavelength radiation. Thus, since atomic interactions can be measured, very good detail in molecular structure can be defined. But, on the other hand, the detail about the atomic interactions is accompanied by a low intrinsic sensitivity, thus the signal requires extensive averaging over many molecules, which limits the intrinsic temporal and spatial resolution.

*Vice versa*, optical spectroscopy uses radiation at an energy level high enough to measure individual photons easily with modern detection equipment, so imaging data are obtained at an individual molecule level of sensitivity. The inherent temporal and spatial resolutions are also increased proportionately, but the resonance itself is broad because environmental influences are not averaged out within the inherent time scale of interaction between the molecules and this frequency of radiation. As a result, the structural information content of optical spectra is considerably lower than that of magnetic resonance, particularly in the electronic region of the spectrum[3].

As a matter of fact, the long-term technical challenge is to extract the maximum possible information from each type of resonance, combining both technologies in order to provide a detailed structural picture of the chemistry at the molecular level with the spatial resolution of individual molecules and a temporal resolution on the time scale of chemical bonding. Moreover, the use of these techniques requires systems with specific optical properties able to emit characteristic signals attributable to specific molecules.

Mass spectrometry techniques can represent an excellent compromise to overcome the several issues which still affected the other techniques and therefore to provide the best quality imaging in the actual instrumentation landscape[2].

## 1.2 Mass Spectrometry Imaging (MSI)

The impossibility of simultaneously obtaining high molecular sensitivity and coherent time-space resolution, and the necessity of samples with specific optical properties, motivates the importance of studying and developing techniques which can provide images with all kinds of samples. Mass spectrometry imaging can simultaneously deliver the spatial distribution of a wide range of atomic and molecular ions detected from the surface of biological samples and surfaces[2]. By combining high sensitivity with the specificity to detect subtle differences between molecules, nowadays mass spectrometry techniques have become one of the most powerful approaches for imaging.

MS imaging is and will become increasingly fundamental for many aspects of materials science. One example is in the semiconductor industry, where the ability to provide spatial and chemical information on the length scales of current integrated circuit fabrication (50 nm or better) with depth

profiling to provide layer-by-layer maps of the fabricated layers is critical for the constant progress of the computer industry.

Moreover, molecular imaging of biological samples by MS is also foreseen to play a pivotal role in understanding numerous biological processes in fields ranging from neuroscience to cancer research[8]. The fundamental contributions of technology in providing molecular-weight-specific images rapidly, at relatively high resolution and sensitivity, will yield important information in the investigation of cellular processes in both health and disease. As a matter of fact, while the imaging technology can rapidly distinguish protein markers of interest, their identification is still a slow and work-intensive process and MS imaging represent an extraordinary discovery tool for this aim, since it is not necessary to know in advance either the specific proteins or their fragmentation patterns for the identification. Furthermore, it allows the study of drug delivery carriers, combining the detection of the drugs and their exactly distribution inside the carrier systems. Therefore, MS imaging tools promise to promote new discoveries in biology and medicine and a more rapid throughput in the technologies of materials.

Also, cultural heritage science demands new characterization methodologies. In fact, sampling and analytical strategies for unique art objects must provide as much information as possible about the composition, history and condition of the artefacts, while ensuring minimal intervention, i.e., minimal sampling[9]. The pursuit of more accurate data using ever smaller samples has been a significant driving force in this field, and mass spectrometry – with its combination of precision and sensitivity – has become a key tool in the study of works of art since its first applications in museum studies were published in the 1960s[10].

A mass spectrometer needs to be equipped with a computer-controlled sample stage capable of motion about the x-y coordinate plane working in conjunction with a probe capable of producing ions from the sample surface (ionization process). By means of specialized software, the motion of the sample stage can be programmed to allow discrete or continuous *rastering* across the sample area whereby individual mass spectra can be collected and assigned to a defined area (x, y) of the sample creating a pixel. After the data acquisition, a software is used to assemble these pixels into an image where the relative intensity of an ion is displayed as a scaled false colour allowing the visualization of the molecular distribution across the surface of the sample for any given observed mass.

Despite these promising attributes, mass spectrometry was not considered the best approach for imaging in the past and scientific adoption was much slower than other techniques. In part this may be due to the lack of specific workflows to provide an exact identification of the molecules, since so few of the many observed signals can be accurately interpreted. As a matter of fact, theoretically molecules observed in a mass spectrum are among the most abundant in the sample and it is

challenging to identify all the signals, even when it is known in advance which molecules are present. As some articles have highlighted, this still represents a general gap in knowledge, not just for imaging, but the entire mass spectrometry field[11, 12]. On the other hand, the great advantage of MS imaging is its ability to specifically pinpoint masses of interest that can be further investigated, which has been further enhanced by means of computer data treatments. In fact, thanks to the recent development of data science methods now it is possible to collect data from a multitude of different sources, to organize the information, to translate the data into results[13], and it can be today applied to MS imaging dataset.

Thanks to all these promising applications and computational tools, in the last decades the adoption of MS techniques for imaging is going to increase significantly. Figure 1.1 shows the number of publications on mass spectrometry imaging per year from an ISI (Institute for Scientific Information) Web of Science[14].

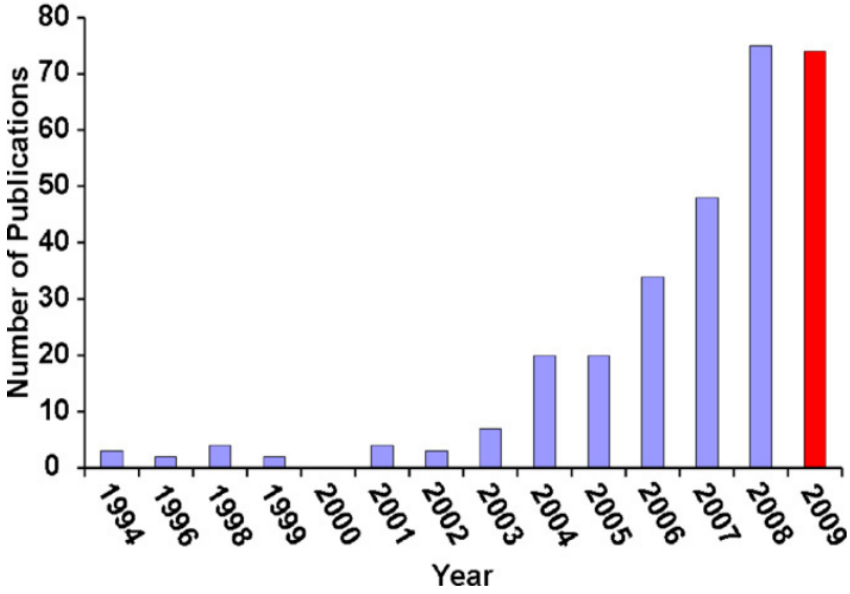


Figure 1.1: : Number of publications per year from an ISI Web of Science search of the topics "imaging mass spectrometry" and "mass spectrometry imaging"[14].

As a part of this scientific landscape, this thesis works presents some ToF-SIMS imaging approaches giving a contribution to the enhancement of the mass spectrometry imaging field.

## 1.3 MSI History and State of Art

Historically, MS imaging studies began with laser microprobe mass spectrometry (LMMS) and laser microprobe mass analysis (LAMMA), commercially available in the late 1970s[15]. LMMS has been used in the analysis of biological samples as well as inorganic samples, wherein a focused UV laser pulsed is used to desorb and ionize solid samples without matrix. The evolution of these techniques

gave birth to MALDI (Matrix Assisted Laser Desorption Ionization). In MALDI experiments, a sample, assisted by a matrix, is mounted on a conductive target plate. A UV or IR wavelength laser beam is used to generate pulsed light which shoots the sample. The energy is first absorbed by the matrix and, via a black box mechanism, transferred to the analyte to induce ionization[16, 17]. Both positive and negative ions are generated by most matrices, however certain matrices will favor positive or negative ion formation. Along the time, this technique was coupled with different mass analysers e.g., time of flight (ToF) and Fourier transform ion cyclotron resonance (FT-ICR)[18, 19].

Contextually, the development of static SIMS in the late 1960s[20], which was combined then with the high-sensitivity of ToF analyser, has given birth to ToF-SIMS a powerful tool for mass spectrometry imaging[21]. In SIMS experiments, samples are mounted on a conductive surface and subjected to etching by a beam of high energy particles. Upon collision with the sample surface, the energy of these primary ions is transferred to the analyte dislodging secondary ions.

The most recent technique is desorption electrospray ionization (DESI) which has been widely studied since its inception in 2004 by Zoltan Takàts et al. [22]. Samples for DESI are mounted on a non-conductive surface where a pneumatically assisted stream of charged solvent droplets is directed at the sample surface. The experiment is performed by the interaction of electrospray generated charged droplets with the sample surface. The impact of the droplets with the surface produces a second generation of charged droplets with dissolved surface molecules. These secondary droplets proceed through an electrospray-type mechanism to form gaseous ions which are directed into an atmospheric inlet of the mass spectrometer[23]. The charge of the ions is determined largely by the solvent used. Figure 1.2 shows the different ionization processes for the three mass spectrometry techniques MALDI, SIMS and DESI.

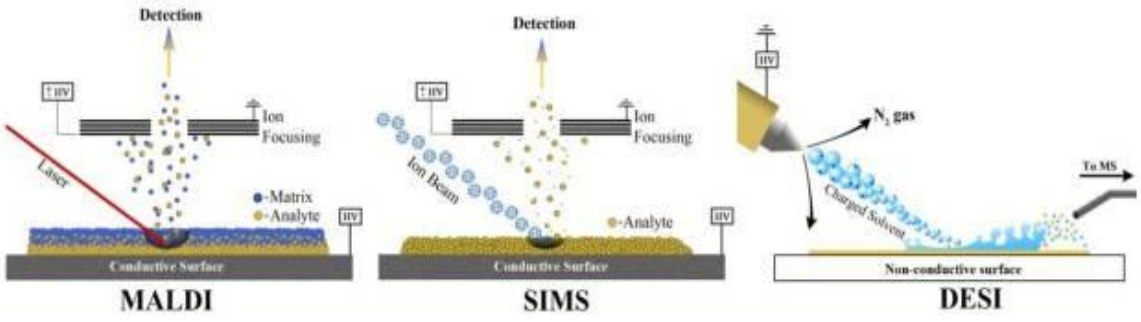


Figure 1.2 Ionization mechanisms for MALDI, SIMS and DESI (picture source[24] )

Up until to the 1970s and 1980s, the use of ToF-SIMS technique was mainly confined to the characterization of inorganic materials. Its application to the study of organic systems was highly

limited by the low yield of secondary ions and by the extensive damaging phenomena and modification of the material due to the chemical reactions induced by the interaction with the primary ions beam[25]. For a long time, the organic material analysis has been possible only using static SIMS conditions that minimize the damaging effect of the surface and allow to obtain information about the molecular nature of the surface itself. On the other hand, static SIMS does not allow studying the composition as a function of the depth, since during the measurement, by definition, only a small part of a monolayer is sputtered.

Therefore, the in-depth investigation of the materials was for a long time carried out with other techniques. Especially in the case of organic materials, other mass spectrometry techniques performed the analyses. As a matter of fact, MALDI and DESI technique families can cover a broader range of biomolecules- including proteins, peptides, and nucleotides. In particular, the ability of detecting proteins brought to a great late success of these techniques in biochemistry and biomedicine field. In fact, nowadays MALDI is the prominent MSI method utilized in bioanalytic research[26].

Despite the great advantages which these techniques offer and their successful applications, the traditional apparatus of MALDI and DESI are only capable of resolving features as small as 20 µm and 100 µm, respectively. Meanwhile, the ToF-SIMS lateral resolution can be below 1µ, offering a complementary perspective to these MSI techniques[27] (Figure 1.3).

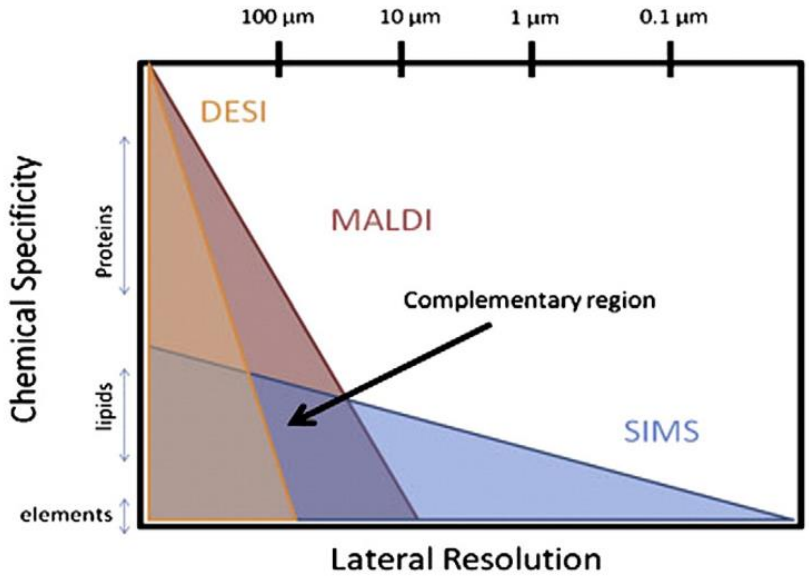


Figure 1.3 : comparison between the lateral resolution and the chemical specificity of MALDI, DESI and ToF-SIMS [27]

For this reason, to enhance the spatial resolution, all the mass spectrometry imaging techniques require a proper handling and preparation of the sample, the selection of correct analysis conditions

and a valid *post-facto* data treatment method. In the several last decades, many instrumentation and techniques upgrades have been developed to improve the quality of the data.

Nevertheless, each mass imaging technique shows specific advantages and disadvantages. As far as DESI is concerned, it has provided influential results across a number of biological samples, thanks to the possibility of ambient surface sampling without sample pre-treatment. This allows the chemical nature of the samples to not be altered, which is especially important for biological samples. On the other hand, this technique is still not able to reach the lateral resolution values of the other MS imaging techniques and it also shows some inherent drawbacks. Additionally, DESI is still incompatible with specific samples[28]. Like many extraction-based approaches, the solvent selection heavily influences the analytes that can be desorbed and ionized from any given sample. The solvent system also impacts the desired spatial resolution of the resulting image since very viscous solvents (such as those with high percentages of organics) rapidly diffuse across a sample. This phenomenon has somewhat limited the technique to solvents miscible with water, precluding some of the more non-polar organic molecules from detection. However, DESI offers a relatively little destruction to the sample. This advantage allows longitudinal studies and real time monitoring, but it may also not permit the identification of structures at the surface of the sample.

In order to partially overcome the spatial resolution limitations of DESI, Julia Laskin et al. developed nanoDESI[29]. The major contribution that this innovation brought to the DESI platform was to create constant droplets from solvent exposed to high voltage using a fused capillary. This allows for a controlled desorption of analytes with the reported spatial resolutions ranging from 10 – 200 microns, depending on the solvent mixture and the molecular source (even though the standard resolution reported in the past for natural products-based sample is 50–200 microns). Nevertheless, the recent papers have shown that high quality high lateral resolution images (with 5 µm spatial resolution) can be accomplished only by means of a laborious post analysis data processing protocol, which needs several postprocessing operations.

Notwithstanding these recent upgrades, DESI still presents several limitations for high resolved spatial imaging, and for this reason MALDI and SIMS are more recommended for high detailed imaging of small objects. In particular, both SIMS and MALDI techniques, especially if coupled with ToF analyser, allow a broad mass range detection ($m/z$ ~1–100,000), that together with the high sensibility and mass accuracy, make them attractive for biology and medicine imaging purposes[30]. Similar to DESI, several strategies were tested in order to achieve high spatial resolution together to high mass resolution also for MALDI and SIMS. To accomplish this aim, the approach involved the more intuitive strategy of decreasing the spot of size of the laser or ion beam. In MALDI, a coaxial

object has been employed to decrease the laser spot size to 1 micron or better[31]. However, fluence considerations limit the applicability of this approach.

An alternative approach to increase the spatial resolution is the *microscope mode imaging* technology[32]. This approach allows to make the obtainable spatial resolution independently from the desorption and ionization spot size. Indeed, the spatial resolution is determined by the quality of the optics components of the instrumentation, which form the image, the x-y position chosen, and the time detector used. These parameters can be more easily controlled in SIMS.

New evolutions of MALDI sources for high mass resolution and high mass accuracy mass analysers, such as FT-ICR and FT-Orbitrap (FT-MS) have been introduced, as well as new ToF analyser, Orbitrap system and ToF MS/MS detector in SIMS. At the same time new generation mass spectrometry techniques were developed, such as NanoSIMS[33]. These new systems allow the separation of ions with the same nominal mass and confident assignment for unambiguous peaks guaranteeing a new level of mass resolution, mass accuracy and transmission.

Among all the new instrumental and technique developments, nanoSIMS shows the highest lateral resolution at a few tens of nanometres. As a consequence, however, it is limited to the collection of elements and only small fragments such as $CN^-$. The strengths of the instrumentation have successfully been exploited by Lechene and co-workers, who have applied stable isotope labelling to develop a 'multi-isotope mass spectrometry' approach[34, 35] on a range of biological samples including stem cell division[34].

MALDI is a well-established technique, but, in contrast with the NanoSIMS, has imaging resolutions at the opposite end of the scale: a few tens of micrometres. The advantage of this technique is that large intact biomolecules with exceptionally large molecular weights (y10 000 Da) can be collected. The technique has therefore been routinely applied for mapping proteins and peptides[36,37]. However, detection below a mass to charge (m/z) ratio of 500 cannot be detected in these systems due to the matrix ions used to enhance the secondary ion (SI) signal.

Considering all the strengths and weaknesses of the mass spectrometry techniques for imaging in the today's landscape, ToF-SIMS imaging seems to be a valid compromise, falling somewhat between the other techniques (and being complimentary to MALDI[38]). A spatial (lateral) resolution of y 200 nm can be achieved in ToF-SIMS, allowing subcellular features to be resolved. This is coupled with good ion detection between up to 1500 Da and possibly up to 2500 Da range. In the light of these considerations, ToF-SIMS is an excellent characterization technique that can address these analysis requirements through both depth profiling analysis and direct 3D chemical imaging.

Despite all the powerful possibilities that this technique can offer, several issues must be resolved to achieve best quality imaging for all the kinds of samples, from the inorganic to the biological ones.

As well as for the other MS imaging techniques, these issues involve the sample preparation, the optimal instrument set-ups, and necessity for a powerful data treatment method able to extract information from low quality spectra and images. In fact, whatever mass imaging technique is chosen, in most cases, a post analysis computing treatment and study is necessary. Examples include the acquired images have not enough counts, or the file data is too big to handle in conventional way, or both. Therefore, computing data treatment is fundamental to extrapolate good results from the datasets.

In this thesis, several examples of ToF-SIMS imaging will be shown, together with the specific necessary sample preparation and data treatment; the ongoing challenges will be also discussed along with recent developments that might offer improved ToF-SIMS imaging prospects soon.

## 1.4 ToF-SIMS Imaging

### 1.4.1 ToF-SIMS sample preparation

As mentioned previously, the sample preparation is a critical step for good analysis and performance for all the mass spectrometry techniques, and sometimes it is crucial for successful detection of desired molecules[39,40]. In order to achieve both more chemical and spatial information from imaging experiments, careful handling and preparation is required. In fact, it is well known that both the choice of matrix and the deposition methodology dictate the molecular weight range observed. Avoiding surface diffusion of analytes in MALDI analyses and the appropriate solvent selection in DESI are crucial for a good mixing of the sample analytes and obtaining convenient dimensions of the drops. As well as for the other mass spectrometry techniques, sample preparation is also key for ToF-SIMS to obtaining high quality data, in order to benefit from the high surface sensitivity that this technique can offer.

Two basic samples requirements are demanded for the analyses: (i) the sample must be compatible with the ultrahigh vacuum (since the analysis occurs at $10^{-10}$ mbar) and (ii) the sample surface presented to the analytical ion beam must be as much flat as possible since the surface roughness will reduce the mass resolution of the analysis. Additionally, due to ToF-SIMS's sensitivity to the surface and its composition, the sample handling procedure must alter the surface in the least possible manner. Otherwise, the integrity of the samples may not be maintained, especially in the case of biological samples[41]. Therefore, surface contaminations must be avoided or at least recognized. The most frequent contamination is from polydimethylsiloxane (PDMS), which in most of the case, once identified can be removed by means of sputtering. Sectioned biological tissue may also contain high levels of $Na^+$ and $K^+$ ions. These native salts must be removed before SIMS analysis, as they can lead

to unreliable secondary ion signals. In these cases, protocols such as *washing* not only can minimize the ion suppression, but it also can allow to enhance the ionization of specific molecules.[39,42]

For biological samples, several procedures have been developed for ToF-SIMS analysis and imaging. Among these, fixation, freeze fracturing, frozen hydration and freeze-drying are the most used[43, 44]. Initially, some of these procedures were deemed unreproducible, but the development of specialist sample stages has improved the results possible via this procedure[45]. Hybrid biomaterials, or in general, porous-like materials pose other problems as they are constructed from a network of interconnected pores. Two methodologies have been assessed by Wang et al.[46] in order to achieve useful SIMS data: "soak and solid" approach, whereby a resin is used to fill the pores and form a flat sample surface, and "mark and map" process, where fiducial marks are made in the regions of interest on scaffold struts using a FIB. For organic and inorganic/organic hybrid scaffolds, the "soak and solid" technique was found to mask compounds of interest, whereas the "mark and map" was the preferred strategy, providing clearer data.

In some cases, to improve the ionization probability of the samples, metal-enhanced and matrix-assisted SIMS have been demonstrated, allowing the detection of a broader range of analytes than unmodified surfaces[47]. In particular, enriching the sample with metals or using a matrix may act to reduce the energy of the chemical bonds between the sample molecules, allowing the transfer into the gas phase of an intact molecular ion of low internal energy. Protonation or cationization can then take place in the selvedge. Alternatively, the matrix may act to reduce the probability of near-surface neutralization of sputtered ions. Moreover, literature reports the capability of SIMS to provide qualitatively useful mass spectra of non-volatile or thermally fragile molecules[48]. The matrix-assisted or metal-enhanced SIMS techniques are relatively simple and sample preparation is more straightforward than in competitive methods. In addition, these methodologies yield spectra which show noteworthy similarities to those obtained by other desorption methods, although the formation of transition metal adducts is at present unique to SIMS.

### 1.4.2 ToF-SIMS imaging issues

SIMS was the first mass spectrometry technique used to generate two-dimensional ion density maps or images from a variety of solid materials and thin sections of biological tissues[49,50]. As is well known, ToF-SIMS involves the bombardment of a sample with a pulsed beam of ions (typically $Bi_n^+$) having energies in the low kiloelectronvolt range (10 to 25 keV). The impact of these energetic ions on the surface of the sample initiates desorption o reionization processes. The bombarding beam can be tightly focused on the surface of the sample in a smaller than 1 $\mu m^2$ area. From a raster of the

surface of the sample, ion density maps or images at specific mass-to-charge (*m/z*) values are generated.

The primary ion energy is transferred to target atoms via atomic collisions, and a so-called collision cascade is generated. Part of the energy is transported back to the surface, allowing surface atoms and molecules to overcome the surface binding energy. The interaction of the collision cascade with surface molecules is soft enough to permit even large and non-volatile molecules with masses up to 10,000 atomic mass units (amu) to escape with little or no fragmentation. Most of the emitted particles are neutral, but a small proportion of these are also positively or negatively charged. Subsequent mass analysis of the emitted ions provides detailed information on the elemental and molecular composition of the surface. The dimensions of the collision cascade are rather small, and the particles are emitted within an area of a few nanometres' diameter. Providing such finely focused primary ion beams, microanalysis with remarkably high lateral resolution (50 nm to 1 μm), can be carried out. To receive chemical information on the original undamaged surface, the primary ion dose density must be kept low enough ($<10^{12/13}$ $cm^{-2}$) to prevent a surface area from being hit more than once. This so-called static SIMS mode is widely used for the characterization of molecular surfaces.

Furthermore, a wide range of various, sputtering ion beams are also available such as $Cs^+$, $Ga^+$, $Ar^+$, $Xe^+$, and $In^+$. These kinds of beams can be used to erode the solid samples in a controlled manner to obtain information on the in-depth distribution of elements. This dynamic SIMS mode is widely applied to analyse thin films, layer structures, and dopant profiles. Cluster ion beams are the most recent sputtering beams, including $Ar_{nn}^+$, $Au_{nn}^+$, $O_2^+$, $SF_5^+$, $C_n^+$ and they tend to be more efficient for desorption and ionization of higher-molecular-weight organic compounds. The molecular range that could be analysed depends on the technique which is chosen for imaging mass spectrometry. With SIMS detectable ions are typically limited to a narrow mass range, below 1 kDa; however, by using cluster ion sources as primary beam it is possible to extend this limit to ~2 kDa[51].

ToF-SIMS is provided with a powerful software to control the whole system and to acquire the data, because of the complexity and rapidity of the required temporal sequences and because of the waste flux of data produced during a ToF-SIMS measurement. Practically, for each position (x, y, z), the value of time-of-flight, signal intensity and sputter time, is noted. In other words, for each point of investigated area and each primary ion pulse, one complete mass spectrum is stored. Once completed the analysis, the software can reconstruct overall spectra (summing each single spectrum) or spectrum of a region of interest (summing the spectra of the pixel included in that area). In this way, it is possible to obtain intensity distribution maps of a selected species on the surface or on a vertical section, basically a depth profile from any selected area. The reconstruction of mass spectra of each point of the whole investigated volume generates a 3D image (Figure 1.4). In fact, it is possible to

execute the retrospective data analysis offline and generate 3D image by saving the complete mass spectrum of each pixel of each image during the depth profiling.

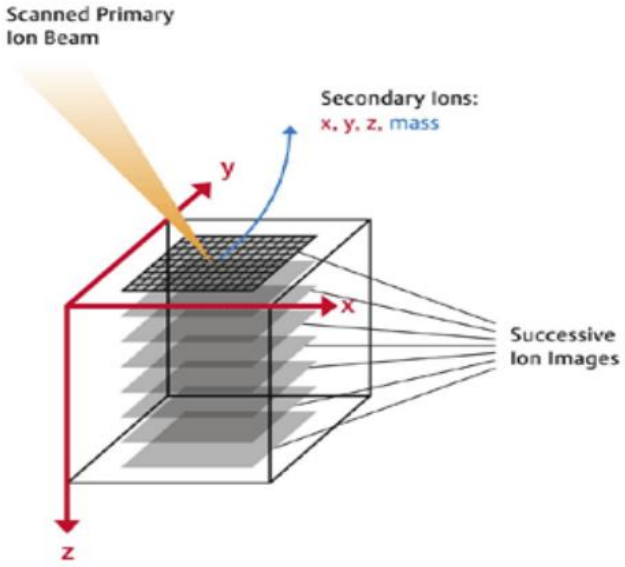


Figure 1.4: parallel acquisition allows the retrospective analysis

In SIMS, 3D imaging is achieved by stacking 2D images (Figure 1.4). There are two methods used to accomplish this result: using a sputtering ion beam to sputter away material without creating significant sub-surface damage (*Dual Beam Modality*) or through a focussed ion beam (FIB) to mill a trench exposing sub-surface material in a plane perpendicular to the top sample surface. In each case, the exposed surface is subsequently reconstructed as mass spectrum of that sample area and the process is repeated to create a 3D image. The first is significantly more popular, since modern ToF-SIMS are normally equipped with different sources and provided with specific software for data reconstruction. The latter method has advantages for hybrid inorganic-organic materials where sputtering yields are strongly different or where there are holes in the sample, which cause strong distortions in an image using the former approach.

Nevertheless, in most cases, the 3D high-resolution imaging is accomplished using a dual beam approach with multiple and sequential cycles of sputtering and analysis. On one hand, this approach has the advantage of decoupling the analysis beam and sputtering beam allowing their individual optimisation, on the other hand, it has a drawback or rather the material sputtered with the second beam is wasted. If an ion dose ratio of 1% (typical value) and similar sputtering rates are assumed (which is reasonable for $Cs^+$ and $C_{60}^+$ or $Ar_{2000}^+$), then around 99% of the material is not analysed. This wastefulness reduces the intensity of the signal and therefore sensitivity in a significant way. If

the dose ratio is increased, the sensitivity could improve, but often this is not possible because of the molecular damage.

As a matter of fact, the erosion process can damage some of the layers below the surface, provoking "mixing and fragmentation" phenomena. These phenomena do not affect significantly inorganic materials while they represent a limit for depth profiling and imaging of organic (both biological and polymeric) materials. If damage accumulation happens into the sample, only an elementary analysis can be performed, losing information about molecular fragments represented for that sample. Until some years ago, organic sample characterization was carried out only by static mode, since the low value of primary beam fluence avoids damage but provides enough sensitivity. Notwithstanding, it does not allow obtaining molecular information along the depth.

Certainly, the advent of cluster and reactive beam has improved ToF-SIMS technique for organic material investigation[52, 53], but several limitations are still to be overcome. In most cases, whatever the scope or the fields, we have to run into analyse exceedingly small objects. From microcircuits with truly little layers of different materials in the microelectronic industry, to the drugs detection in liposomes, mitochondria, and various organelles for biotechnical industry. Due to the small size, only a limited number of ions can be created and measured. Thus, the first big challenge is related to the secondary ion signal intensity.

The ToF-SIMS signal intensity of a generic species A, called $I_A$ (ions/s), is given by Equation 1.1:

$$I_A = I_p \times C_A \times Y_{TOT} \times \alpha_A^{\pm} \times T_A D_A$$

Equation 1.1

where

$I_p$ is the primary ion current flux (ions/s)

$C_A$ is the A species concentration

$Y_{TOT}$ is the total sputtering yield

$\alpha_A^{\pm}$ is ionization probability

$T_A D_A$ are instrumental factors related to transmission and efficiency of detection

When dealing with small samples, the secondary ion intensity $I_A$, is limited by several factors.

The primary method in SIMS to generate more secondary ions is to the increase the dose of the primary ion beam. However, high primary ion doses can damage the sample molecules and prevent their detection. Therefore, the secondary ions are already limited by the low primary ion floods. Second, the limited sample volume indicates a small concentration of the species of interest in the

sample to begin with, i.e., Ca is incredibly low. Third, $Y_{TOT}$ is comprised of many factors, including the specific chemical nature of the material and in many cases, it shows extremely low values. Fourth, the ionization probability for the species of interest is related to the surrounding atoms and therefore the chemical structure of the sample.

One of the most challenging issues which must be solved in ToF-SIMS imaging is obtaining sufficient signal for each pixel. In other words, for a given pixel size there is a finite number of molecules available for analysis because of the relation between the ionization yield and concentration of that molecule in the analysed area. Therefore, in order to achieve statistically meaningful counts, more sputtering time is required for generating sufficient ions. This means that for acquiring a good quality image long analysis times are necessary. Moreover, extra sputtering time can damage the molecules, actually decreasing ionization with time. In some cases, however, the size of the sample is too small, and enough ions cannot be collected even with extended analysis times.

Sputtering yield (Y) is another problematic parameter that influences the signal intensity. The total sputtering yield is defined as the total number of removed atoms (whatever it is their state, isolated or inside molecules, fragments or cluster, and the number of charges) for incident primary ion, and it is peculiar for each material for a defined sputtering beam and energy. This parameter can be easily evaluated from a depth profile of a homogeneous sample, if it is known the total fluence required for eroding a definite thickness (which is estimated through independent measurements). The sputtering yield is defined by the equation 1.2:

$$Y = \frac{dA\rho\frac{N_A}{M}}{I\frac{t}{e}}$$

Equation 1.2

where the numerator represents the emitted atoms number, and the denominator represents the incident ions number; in particular

- d is the thickness of eroded layer of the sample
- A is the investigated area
- ρ is the material density
- M the atomic mass
- I is the employed ionic current
- e is the unitary charge
- t is time necessary to sputter the measured thickness

The sputtering yield is often calculated as volumetric sputtering yield, or rather the eroded volume for incident ion ($nm^3$/ion).

Finally, the sputter velocity is defined as eroded thickness for time unit. For many materials, sputtering yield values are between 0,1 and 10, using low energy monoatomic beam. When the beam hits the sample, it could cause damage, especially for the organic compounds. Indeed, the beam bombarding may induce radical reactions, which lead to significant transformations until the organic material becomes carbon. This phenomenon often provokes the sputtering yield decrease, thereby lowering the signal intensity and making the image reconstruction difficult.

The ionization efficiency is also related to the ionization probability $\alpha_A^{\pm}$, as we can see from the Equation 1. The ionization probability $\alpha_A^{\pm}$ is defined as the fraction of emitted ions positively or negatively compared to the total number of charged or neutral species emitted during sputtering and it is typically less than 0.01 and sometimes even smaller of several magnitude order than this indicative value. This parameter varies from several magnitude order depending on many variables, such as species nature, chemical surrounding, residual gases pressure and primary ion features, provoking dramatic variation on ionization efficiency. Consequently, no quantification is possible. This process is known as *Matrix Effect*[54]. In extreme cases, the ion yield may be completely suppressed. Therefore, it should always be remembered that just because an ion is not detected, it does not mean that the molecule is not there. It is important to note that the *Matrix Effect* affects all the mass spectrometry imaging methods.

Different strategies can be used to increase $I_A$. The first of these strategies is increase the signal- noise ratio. To do this, it is necessary to collect many scans of the same sample area. In this way the noise, which is determined by instrumental factor, will remain constant. Meanwhile, the number of counts comprising the signal peaks will be enhanced, because the ion intensity is a sum of the intensity from all scans. One drawback, however, is the additional time to acquire extra scans, which may preclude this method from some applications (i.e., when data for many samples is desired). The second strategy is to the increase the primary ion current, which is causally related to the secondary ion intensity. Yet, this method is dramatically limited especially for organic species, in both static-SIMS and dynamic-SIMS applications. Static SIMS already puts a limitation on the dose for maintaining the surface, and dynamic SIMS can be affected by molecule damage from too high of a dose. The next strategies focus on the creating a positive matrix effect to increase the ionization probability. These include modifying the sample composition, the changing the primary ion beam, or by gas dosing the chamber. In all three methods, the surrounding environment of the species of interest is altered to enhance ionization. The final approach deals with treatment of the acquired data post-analysis. This approach requires

computing modelling and programs able to handle limited signals and extrapolating to a higher quality result.

When changing the application to imaging mode, all of these ToF-SIMS signal limitations are exacerbated. Indeed, imaging a sample requires a high spatial resolution only achievable with a sharp, low-current primary beam. As a matter of fact, it is necessary a good focusing of the ion beam and enough signal intensity detection from the analysed area in order to give sufficient counting statistics. By Equation 1, it is clear that imaging-mode will suffer a lower secondary ion intensity and obtaining sufficient signal will be even more complicated. The signal intensity may be increased by acquiring data for long time for increasing the dose. However, as previously said, for organic samples the signal intensity is reduced because of ion beam induced damage. Therefore, in most of the cases, the amount of signal that can be integrated is limited. Kollmer[55] introduced the concept of *Useful Lateral Resolution* (L), which defined the resolution that could be achieved with a given signal-noise ratio for molecules with a given disappearance cross-section. Equation 1.2 was later modified[56] for the general case; in this way the *Useful Lateral Resolution* L for a signal-to-noise ratio s is:

$$L(d) = s\sqrt{\frac{A}{\sum_0^d I}}$$

Equation 1.3

where I is the signal intensity which may vary with depth from an area A and d is the thickness of the consumed material. Therefore, if I is constant as material is sputtered then L improves as √d.

As pointed out before, the focusing of the primary ion beam is also an important parameter to achieve a good spatial resolution. The focus of source guns can be improved by using smaller apertures, but this strongly attenuates the beam current and, thus, the number of secondary ions produced. Moreover, if the beam current is too low it becomes impractical to consume enough material in a reasonable time. The only method to enhance the image is through treatment of the data post analysis. Transforming imaging analyses data is not a trivial task due to the dimension of the data. In fact, imaging-SIMS belongs to the well-known definition of big data. Consider first the standard 2-dimensional SIMS image. In this case, each x- y- point contains a mass spectrum and possibly more depending on the number of analyses scans. Therefore, each image is comprised of thousands of mass spectra depending on the number pixels defined at the start of analysis. 2D surface images already represent a large data file. In the case of 3D imaging, the depth dimension increases the file size further by the total number of data cycles selected for the acquisition. Thus, particularly for the case of SIMS imaging, we need to address big data, and utilize the numerical strategies and methodologies to enhance the image files post analysis.

### 1.4.3 Big ToF-SIMS data

Big data is a term for massive data sets having large, more varied and complex structure with the difficulties of storing, analysing and visualizing for further processes or results. The process of research into massive amounts of data to reveal hidden patterns and secret correlations named as big data analytics.

As above mentioned, ToF-SIMS analyses often give origin to big data sets, especially in the case of imaging, which need to be handled through big data analytics methodologies. As a matter of fact, modern ToF-SIMS spectrometers generate hyperspectral image data sets usually containing 128 × 128, 256 × 256, or even a larger number of pixels. For each pixel, a high-resolution mass spectrum is stored, composed by up to several millions of time-of-flight channels. If sputtering is carried out, by alternating imaging cycles with erosion cycles, it is possible to obtain a 3D description of the sample, essentially composed by a stack of 2D images. This leads to a rapid growth of the size of the data sets that must be handled. The amount of stored data can be even larger in recently introduced instrumentation that combines different types of mass analysis, e.g., ToF and Orbitrap.

As said, these kinds of data sets require specific methods of post-analysis treatments. Research into computational methods for ToF-SIMS imaging data, as well as for the other mass spectrometry imaging techniques, has touched upon different aspects, including spectral pre-processing, data formats, dimensionality reduction, spatial registration, sample classification, statistical and differential analysis between the experiments and data-driven[57,58]. From these initial studies many defined data treatment methodologies based on machine learning have been developed. Within these data mining different methodologies, there are clear distinctions between supervised and unsupervised approaches[59]. Supervised methods seek to model a specific recognition task. For example, classification approaches applied to in a digital pathology context can predict tissue classes and tumour labels after having been shown representative example measurements annotated by a pathologist. Unsupervised approaches, on the other hand, are not focused on a particular recognition task, but instead seek to discover the underlying structure within a dataset, uncovering trends, correlations, and associations along the spatial and spectral domains. These methods are generally applied to provide a more open-ended exploratory perspective on the data, without particular spatial areas or ions of interest in mind. The structure they find in the data can be employed for aiding human interpretation but can also serve to reduce the dimensionality and computational load for subsequent computational analyses. Unsupervised methods include, for example, factorization methods such as principal component analysis (PCA) and nonnegative matrix factorization (NMF), but also clustering approaches seeking to delineate underlying groups of spectra or pixels with similar chemical expression, and manifold learning[60,61].

Currently, the most popular approaches for handling and interpretation of ToF-SIMS data are based on multivariate analysis methods. Among these, principal component analysis (PCA) and other related techniques became a sort of standard approach in the ToF-SIMS community[62,63]. PCA is a multivariate procedure, which allows to extract features from a complex set of data. Practically, PCA rotates the data until the maximum variability is projected onto the axes. The main aim is to reduce the dimensionality of a data set while retaining as much information as possible in order to obtain a compact and optimal description of the data set. This approach has been extensively applied successfully to ToF-SIMS dataset of various samples, such as proteins, synthetic polymers, human tissues, or also defects, contaminants and so on.

Despite the PCA applicability, in the case of extremely big datasets or low-counts datasets, due to computational limitations, PCA treatment requires a pre-processing of the data set in order to decrease substantially its size or to extract latent information. Typical pre-treatments can include unit mass binning or peak picking and integration (either manual or automated) and they are often combined with pixel binning[64]. Such pre-treatments can lead to a loss of resolution (both mass and spatial resolution) and, moreover, they can be biased by subjective analyst's decisions and by errors of automated peak search/integration routines. Recently, a few methods for unattended multivariate analysis of raw and unbinned data set have been reported, with the aim of avoiding some of the above-mentioned drawbacks[65,66]. However, the large amount and high-dimensional nature of data generated by mass imaging techniques make automated computational analysis indispensable, preventing the necessity of a pre-treatments that can bring to errors and losses of the data.

For these reasons, developing and designing new approaches for the big data SIMS it is nowadays a priority for the enchantment of this technique. Moreover, in many cases and especially for single pixel data, ToF-SIMS datasets can exhibit extremely low intensity (typically up to 99% of zero-signal channels)[67]. Therefore, methods that take advantage of such scarcity of signal dispersed in a big data set are especially useful to cope with the continuous increase of information collected by means of modern instrumentation.

Nowadays, whichever field, research is affected by several complex problem settings. Such complexity evokes an increasing need for computer applications that show "intelligent behaviour". In fact, these applications are desired to support decision-making, to control processes or to recognize and interpret patterns. Computational intelligence approaches are able to accomplish such tasks.

As well as for other complex data settings, computational intelligence approaches can be applied successfully also for big data SIMS treatment, allowing to extract latent chemical information form ToF-SIMS data from uncompressed and unbinned raw data sets.

## 1.5 Conclusions

In this chapter, the topic of imaging and its applications was introduced. Several techniques were presented with a focus on mass spectrometry. ToF-SIMS was shown as one of the most powerful techniques because it shows several advantages for sample handling, non-destructive analysis of the sample, several equipment possibilities that can be optimized for different samples, reconstruction of acquired data, and post analysis data treatments.

It was moreover discussed that multivariate analysis approaches, employed so far for big data SIMS treatments, can be insufficient for a good data handling, because of several limitations. Computational intelligence approaches can offer a high-performance alternative for such aim. The dissertation in the next chapters will explore the use of ToF-SIMS technique applied to several different “model” samples, exploring all the possibilities that this technique can offer and providing new approaches for sample preparation and post analysis data treatments.

# Outline of Thesis Work

In view of the above-mentioned issues, this thesis work deals with ToF-SIMS characterization and imaging of different kinds of organic "model" samples. These "model" samples have been chosen in order to explore the opportunities this technique can offer and to study which variables or phenomena can undermine the results and the image quality. The samples that have been investigated encompass several organic materials or molecules. They exhibit different composition and structure both in the surface or in the volume and each one of their components can show varied ionization yield. Therefore, they represent an objective and a tangible difficulty for the analysis. A deeper knowledge of materials and molecules allows their use in the best and the most convenient way. Each "model" sample has a different aim and field of application, but all of them require further investigation to reach a deeper comprehension and ultimately utilization. This thesis work demonstrates the potentiality of ToF-SIMS and new capabilities in the post analysis data treatment, to probe a wide range of materials and molecules and advance their understanding. Moreover, some computational approaches for ToF-SIMS data treatment are presented. These approaches show procedures which can be easily automatized and therefore can be applied for several different purposes.

Chapter 2 deals with the Solid Lipid Nanoparticles (SLNs) analysis. The dissertation shows the SLNs potential applications in pharmacodynamics, but at the same time, it points out the lack of a complete spatial and compositional characterization, which may be essential to increase their efficacy. The chapter displays the achieved results of the ToF-SIMS characterization of these systems, in particular the 3D images that for the first time have been acquired for SLNs. Moreover, it is also presented a new approach of solid sample preparation which allows to overcome the aggregation of the particles.

Chapter 3 shows the results of ToF-SIMS application is Cultural Heritage. In particular, textiles from 19$^{th}$ century were characterized by means of ToF-SIMS analysis and imaging in order to find out the chemical nature of the dyes employed for colouring them. The results show that for one sample, it was possible to identify the chemical nature of the dye, and chemical images of the textile were acquired. Moreover, principal component analysis was chosen as post analysis data treatment of the images. The PCA results were able to find out components of different chemical nature and, with the support of the literature it was also possible to unveil a 19$^{th}$ century colouring technique.

Chapter 4 presents the results of the ToF-SIMS imaging of a polymer blend, in particular a PET (75%)- PC (25%) blend. It is shown a thermal ageing experiment, more specifically, on one of the PET-PC samples underwent a temperature ramp from -10°C up to 320°C. The results demonstrate that by mean of ToF-SIMS imaging, it was possible to monitor the domain structured surface of the sample and in this way to identify the modification occurred at different temperature. This experiment

was performed thanks to the ToF-SIMs instrumentation apparatus which easily allows to apply a wide ramp of temperature and therefore, to test the material stability at various temperatures. These kinds of experiments may support the material science research for the design and production of new and more efficient materials made out of immiscible molecules.

In chapter 5 a different approach for polymer recognition is presented. When dealing with low-counts ToF-SIMS datasets, it can be difficult to distinguish spectra belonging to different species. This problem is exacerbated when dealing with polymers, since they can show very similar spectra and a wrong assignment of the peaks can occurred. Generally, it becomes necessary to increase the number of counts by acquiring data for long time. However, does this strategy not only require additional time to acquire extra scans, but also it can cause beam induced damage, especially in the case of organic and polymeric samples. A possible strategy to overcome this issue can be a post-analysis computational approach. As discussed in the introduction, the most popular is multivariate analysis e.g., PCA, which is able, in most of the cases, to distinguish features in samples with different chemical species. However, as stated in the introduction, PCA often requires pre-processing treatments, especially in the case of low-counts datasets. These treatments can bring to loss of data quality. The chapter presents a different approach for polymer recognition based on computer intelligence method: a probabilistic neural network (PNN) was designed and trained to provide a correct classification of four different polymers. It is demonstrated that this neural network can extract latent chemical information from ToF-SIMS imaging data of four different polymers, working on the uncompressed and unbinned raw data set.

Chapter 6 shows that a computer intelligence approach for ToF-SIMS imaging can successfully be applied for identification of contaminants in overlapped fingerprints. This sample represent a truly difficult challenge, since overlapped fingerprints imaging can give rise to an extended massive big data. As a matter of fact, a sample of two fingerprints were analyzed by ToF-SIMS in macroraster modality, acquiring a macroraster of 7000 × 7000 pixels image. This kind of file contains so much information that it is not possible to handle in a conventional way. For this purpose, an unsupervised dimensionality reduction procedure was employed which allows to extract relevant information from big datasets having poor statistics such as those obtained from analyses performed in macroraster modality.

*References*


1. da Cunha MML, Trepout S, Messaoudi C, et al. Overview of chemical imaging methods to address biological questions. *Micron*. 2016;84:23-36. doi:10.1016/j.micron.2016.02.005
2. Buchberger AR, DeLaney K, Johnson J, Li L. Mass Spectrometry Imaging: A Review of Emerging Advancements and Future Insights. *Analytical Chemistry*. 2018;90(1):240-265. doi:10.1021/acs.analchem.7b04733
3. National Research Council -. *VISUALIZING CHEMISTRY : The Progress and Promise of Advanced Chemical Imaging. :*; 2006.
4. Field C, Shenton H. Evidence at The Report of the House of Lords Science and Technology Sub-Committee's Inquiry into Science and Heritage, published November 16, 2006. *HL Paper 256*. 2006;(October):9-287. http://www.parliament.uk/business/committees/committees-archive/lords-s-t-select/heritage/%0Ahttp://www.publications.parliament.uk/pa/ld200506/ldselect/ldsctech/256/256.pdf
5. Kalinin S v., Sumpter BG, Archibald RK. Big-deep-smart data in imaging for guiding materials design. *Nature Materials*. 2015;14(10):973-980. doi:10.1038/nmat4395
6. Dilsizian SE, Siegel EL. Artificial intelligence in medicine and cardiac imaging: Harnessing big data and advanced computing to provide personalized medical diagnosis and treatment. *Current Cardiology Reports*. 2014;16(1). doi:10.1007/s11886-013-0441-8
7. Luker GD, Luker KE. Optical Imaging: Current Applications and Future Directions. *Journal of Nuclear Medicine*. 2008;49(1):1-4. doi:10.2967/JNUMED.107.045799
8. Mohammadreza Shariatgorji PS and PEAndrén. Mass Spectrometry Imaging, an Emerging Technology in Neuropsychopharmacology. *Neuropsychopharmacology*. 2014;Vol. 39:34–49.
9. Jana Sanyova, Sophie Cersoy, Pascale Richardin, Olivier Laprévote, Philippe Walter and AB. Unexpected Materials in a Rembrandt Painting Characterized by High Spatial Resolution Cluster-TOF-SIMS Imaging. *Anal Chem*. 2011;83(3):753–760. doi:doi.org/10.1021/ac1017748
10. Ferreira ESB, Heeren RMA, van den Berg KJ, Maines C, Sutherland K, Higgitt C. Mass Spectrometry of Art and Cultural Heritage. *International Journal of Mass Spectrometry*. 2009;284(1-3):1. doi:10.1016/j.ijms.2009.04.006
11. Arita M. What can metabolomics learn from genomics and proteomics? *Current Opinion in Biotechnology*. 2009;20(6):610-615. doi:10.1016/j.copbio.2009.09.011
12. Duncan MW, Aebersold R CRM. The pros and cons of peptide-centric proteomics. *Nat Biotech*. 2010;Vol. 28:659-664. http//doi.org/10.1038/nbt0710-659

13. B. Sun, M. P. Edgar, R. Bowman, L. E. Vittert, S. Welsh, A. Bowman MJPadgett. 3D Computational Imaging with Single-Pixel Detectors. *Science*. 2013;Vol. 340(6134):844-847.
14. Jonathan Adams, David Pendlebury RP and MS. *Global Research Report Multi-Authorship and Research Analytics*.; 2019. doi:ISBN 978-1-9160868-6-9
15. Gagnon H, Franck J, Wisztorski M, Day R, Fournier I, Salzet M. TARGETED MASS spectrometry Imaging: Specific Targeting Mass Spectrometry imaging technologies from history to perspective. *Progress in Histochemistry and Cytochemistry*. 2012;47(3):133-174. doi:10.1016/j.proghi.2012.08.002
16. H.J. Heinen, S. Meier, H. Vogt RWechsung. LAMMA 1000, a new laser microprobe mass analyzer for bulk samples. *J Mass Spectrom Ion Phys*. 1983;47:19-22.
17. L. van Vaeck, H. Struyf, W. van Roy, F. Adams. *Mass Spectrom Rev*. 13:189.
18. Hillenkamp, F., Unsöld, E., Kaufmann R et al. A high-sensitivity laser microprobe mass analyzer. *Appl Phys*. 1975;8:341–348. https://doi.org/10.1007/BF00898368
19. Amstalden van Hove ER, Smith DF, Heeren RMA. A concise review of mass spectrometry imaging. *Journal of Chromatography A*. 2010;1217(25):3946-3954. doi:10.1016/j.chroma.2010.01.033
20. Benninghoven, A; Rudenauer, F G; Werner HW. *Secondary Ion Mass Spectrometry: Basic Concepts, Instrumental Aspects, Applications and Trends*. (Energy USD of, Information O of S and T, eds.).; 1987.
21. JC Vickerman DB. *Tof-SIMS: Materials Analysis by Mass Spectrometry - 2013*. surfacespectra; 2013.
22. Takáts Z. Mass Spectrometry Sampling Under Ambient Conditions with Desorption Electrospray Ionization. , et al. . *Science*. 2004;306((5695)):471–473.
23. R. Graham Cooks1, Zheng Ouyang, Zoltan Takats JMW. Ambient Mass Spectrometry. *Science*. 2006;Vol. 311(5767):1566-1570.
24. Matthias Holzlechner, Eliseo Eugenin, Brendan Prideaux. Mass spectrometry imaging to detect lipid biomarkers anddisease signatures in cancer. *Cancer Repor*. 2019;2(6). doi:doi/abs/10.1002/cnr2.1229
25. Benninghoven A. Surface analysis by Secondary Ion Mass Spectrometry (SIMS). *Surface Science*. 1994;299–300:246-260. doi:https://doi.org/10.1016/0039-6028(94)90658-0
26. Joseph E. Spraker, Gordon T. Luu LMS. Imaging mass spectrometry for natural products discovery: a review of ionization methods. *Nat Prod Rep*. 2020;37:150-162. doi: https://doi.org/10.1039/C9NP00038K

27. Passarelli MK, Winograd N. Lipid imaging with time-of-flight secondary ion mass spectrometry (ToF-SIMS). *Biochimica et Biophysica Acta - Molecular and Cell Biology of Lipids*. 2011;1811(11):976-990. doi:10.1016/j.bbalip.2011.05.007

28. Thomas M, Heath BS, Laskin J, et al. Visualization of high resolution spatial mass spectrometric data during acquisition. *Proceedings of the Annual International Conference of the IEEE Engineering in Medicine and Biology Society, EMBS*. Published online 2012:5545-5548. doi:10.1109/EMBC.2012.6347250

29. Yin, R., Burnum-Johnson, K.E., Sun, X., Sudhansu K. Dey, Julia Laskin. High spatial resolution imaging of biological tissues using nanospray desorption electrospray ionization mass spectrometry. *Nat Protoc*. 14:3445–3470. doi: https://doi.org/10.1038/s41596-019-0237-4

30. Dollery CT. Intracellular drug concentrations. *Clinical Pharmacology and Therapeutics*. 2013;93(3):263-266. doi:10.1038/clpt.2012.240

31. Koestler M, Kirsch D, Hester A, Leisner A, Guenther S, Spengler B. A high-resolution scanning microprobe matrix-assisted laser desorption/ionization ion source for imaging analysis on an ion trap/Fourier transform ion cyclotron resonance mass spectrometer. *Rapid Communications in Mass Spectrometry*. 2008;22(20):3275-3285. doi:10.1002/rcm.3733

32. Fournier I, Marinach C, Tabet JC, Bolbach G. Irradiation effects in MALDI, ablation, ion production, and surface modifications. Part II: 2,5-dihydroxybenzoic acid monocrystals. *Journal of the American Society for Mass Spectrometry*. 2003;14(8):893-899. doi:10.1016/S1044-0305(03)00347-7

33. Nuñez J, Renslow R, Cliff JB, Anderton CR. NanoSIMS for biological applications: Current practices and analyses. *Biointerphases*. 2018;13(3):03B301. doi:10.1116/1.4993628

34. Steinhauser ML, Bailey AP, Senyo SE, et al. Multi-isotope imaging mass spectrometry quantifies stem cell division and metabolism. *Nature*. 2012;481(7382):516-519. doi:10.1038/nature10734

35. LECHENE C. Electron-Probe Analysis of Cultured Cells. *Annals of the New York Academy of Sciences*. 1986;483(1):270-283. doi:10.1111/j.1749-6632.1986.tb34532.x

36. Stoeckli M, Chaurand P, Hallahan DE, Caprioli RM. Imaging mass spectrometry: A new technology for the analysis of protein expression in mammalian tissues. *Nature Medicine*. 2001;7(4):493-496. doi:10.1038/86573

37. Dilillo M, Pellegrini D, Ait-Belkacem R, de Graaf EL, Caleo M, McDonnell LA. Mass Spectrometry Imaging, Laser Capture Microdissection, and LC-MS/MS of the Same Tissue

Section. *Journal of Proteome Research*. 2017;16(8):2993-3001. doi:10.1021/acs.jproteome.7b00284

38. Touboul D, Roy S, Germain DP, Chaminade P, Brunelle A, Laprévote O. MALDI-TOF and cluster-TOF-SIMS imaging of Fabry disease biomarkers. *International Journal of Mass Spectrometry*. 2007;260(2-3):158-165. doi:10.1016/j.ijms.2006.09.027
39. Kaletaş BK, van der Wiel IM, Stauber J, et al. Sample preparation issues for tissue imaging by imaging MS. *Proteomics*. 2009;9(10):2622-2633. doi:10.1002/pmic.200800364
40. Schwartz SA, Reyzer ML, Caprioli RM. Direct tissue analysis using matrix-assisted laser desorption/ionization mass spectrometry: Practical aspects of sample preparation. *Journal of Mass Spectrometry*. 2003;38(7):699-708. doi:10.1002/jms.505
41. Malmberg P, Jennische E, Nilsson D, Nygren H. High-resolution, imaging TOF-SIMS: Novel applications in medical research. *Analytical and Bioanalytical Chemistry*. 2011;399(8):2711-2718. doi:10.1007/s00216-010-4155-0
42. Seeley EH, Caprioli RM. Molecular imaging of proteins in tissues by mass spectrometry. *Proceedings of the National Academy of Sciences of the United States of America*. 2008;105(47):18126-18131. doi:10.1073/pnas.0801374105
43. Fearn S. Characterisation of biological material with ToF-SIMS: A review. *Materials Science and Technology (United Kingdom)*. 2015;31(2):148-161. doi:10.1179/1743284714Y.0000000668
44. Touboul D, Brunelle A, Laprévote O. Mass spectrometry imaging: Towards a lipid microscope? *Biochimie*. 2011;93(1):113-119. doi:10.1016/j.biochi.
45. Goodwin RJA. Sample preparation for mass spectrometry imaging: Small mistakes can lead to big consequences. *Journal of Proteomics*. 2012;75(16):4893-4911. doi:10.1016/j.jprot.
46. Daming Wang, Gowsihan Poologasundarampillai, Wouter van den Bergh, Richard J Chater, Toshihiro Kasuga, Julian R Jones and DSM. Strategies for the chemical analysis of highly porous bone scaffolds using secondary ion mass spectrometry. *Biomedical Materials*. 2014;9(1).
47. JC Vickerman, D Briggs. *Tof-SIMS: Materials Analysis by Mass Spectrometry*. surface Analysis Research Centre, Manchester Istitute; 2013.
48. Fletcher JS, Vickerman JC. Secondary ion mass spectrometry: Characterizing complex samples in two and three dimensions. *Analytical Chemistry*. 2013;85(2):610-639. doi:10.1021/ac303088m

49. Braun RM, Blenkinsopp P, Mullock SJ, et al. Performance characteristics of a chemical imaging time-of-flight mass spectrometer. *Rapid Communications in Mass Spectrometry*. 1998;12(18):1246-1252. doi:10.1002/(SICI)1097-0231(19980930)12:18

50. Timothy J. Cornish and Robert J. Cotter. High-Order Kinetic Energy Focusing in an End Cap Reflectron Time-of-Flight Mass Spectrometer. *Anal Chem*. 1997;69(22):4615–4618. doi: https://doi.org/10.1021/ac970479m

51. Komatsu M, Murayama Y, Hashimoto H. Protein fragment imaging using ink jet printing digestion technique. *Applied Surface Science*. 2008;255(4):1162-1164. doi:10.1016/j.apsusc.2008.05.262

52. Mahoney CM, Roberson S v, Gillen G. Depth Profiling of 4-Acetamindophenol-Doped Poly ( lactic acid ) Films Using Cluster Secondary Ion Mass Spectrometry. 2004;76(11):3199-3207. doi:10.1021/ac035532n

53. Kozole J, Winograd N. *Cluster Secondary Ion Mass Spectrometrys*.; 2014. doi:10.1007/978-3-319-01360-2_4

54. v. R. Deline, Peter Williams, William Katz, C. A. Evans Jr. Mechanism of the SIMS matrix effect. *Appl Phys*. 33(832). doi: https://doi.org/10.1063/1.90546

55. Kollmer F. Cluster primary ion bombardment of organic materials. *Applied Surface Science*. 2004;231-232:153-158. doi:10.1016/j.apsusc.2004.03.101

56. Vickerman JC. *ToF-SIMS-An Overview*. https://www.researchgate.net/publication/266462581

57. Jones EA, Deininger SO, Hogendoorn PCW, Deelder AM, McDonnell LA. Imaging mass spectrometry statistical analysis. *Journal of Proteomics*. 2012;75(16):4962-4989. doi:10.1016/j.jprot.2012.06.014

58. Piantadosi C, Smart RSC. Statistical comparison of hydrophobic and hydrophilic species on galena and pyrite particles in flotation concentrates and tails from TOF-SIMS evidence. *International Journal of Mineral Processing*. 2002;64(1):43-54. doi:10.1016/S0301-7516(01)00075-8

59. Bishop CM. *Pattern Recognition and Machine Learning*.

60. Lee DD, Seung HS. Learning the parts of objects by non-negative matrix factorization. 2000;401(October 1999):788-791.

61. Oded Maimon,Lior Rokach. *Data Mining and Knowledge Discovery Handbook*. Springer Science; 2005. doi:doi.org/10.1007/978-0-387-09823-4

62. Wagner MS, Graham DJ, Castner DG. Simplifying the interpretation of ToF-SIMS spectra and images using careful application of multivariate analysis. *Applied Surface Science*. 2006;252(19):6575-6581. doi:10.1016/j.apsusc.2006.02.073

63. Nicoletta Giamblanco, Genady Zhavnerko, Nunzio Tuccitto, Antonino Licciardello, and Giovanni Marletta. Coadsorption-dependent orientation of fibronectin epitopes at hydrophilic gold surfaces. *Soft Matter*. 2012;8(32):8370-8378. doi:doi.org/10.1039/C2SM25490E

64. Tyler B. Interpretation of TOF-SIMS images: Multivariate and univariate approaches to image de-noising, image segmentation and compound identification. *Applied Surface Science*. 2003;203-204:825-831. doi:10.1016/S0169-4332(02)00835-8

65. Tanji K, Komatsu M, Hashimoto H. Adaptive three-dimensional wavelet analysis for denoising TOF-SIMS images: Toward digital staining of pathological specimens. *Proceedings - 2011 4th International Conference on Biomedical Engineering and Informatics, BMEI 2011*. 2011;1:100-104. doi:10.1109/BMEI.2011.6098270

66. Milillo TM, Gardella JA. Spatial statistics and interpolation methods for TOF SIMS imaging. *Applied Surface Science*. 2006;252(19):6883-6890. doi:10.1016/j.apsusc.2006.02.164

67. Graham DJ, Castner DG. Multivariate analysis of ToF-SIMS data from multicomponent systems: The why, when, and how. *Biointerphases*. 2012;7(1-4):1-12. doi:10.1007/s13758-012-0049-3

# 2 ToF-SIMS imaging of Solid Lipid Nanoparticles (SLN)

As stated in the introduction, ToF-SIMS can be an excellent technique also in the field of pharmaceutical and medical sciences. In fact, its applications include the investigation of systems for drug delivery, for which it is very important to provide a complete three-dimensional chemical characterization. An example of drug delivery systems, whose use is spreading in the pharmaceutical field, is constituted by the solid lipid nanoparticles (SLNs).

SLNs are a recent pharmaceutical delivery system introduced in 1991 and they represent an alternative carrier system to traditional colloidal carriers, such as emulsions, liposomes and polymeric micro- and nanoparticles. They combine the advantages of lipid emulsion and polymeric nanoparticle systems while overcoming the temporal and in vivo stability issues that trouble the conventional as well as polymeric nanoparticles[1]. These particles can incorporate both lipophilic and hydrophilic drugs and avoid the use of organic solvents (therefore they do not show biotoxicity). Moreover, they allow the possibility of controlled drug release and drug targeting, also increasing the drug stability compared to other carrier systems and have large scale production potential.

The morphology of these systems has been investigated by means of several techniques, such as electronic or atomic force microscopies[2,3,4]. However, these characterization methodologies do not allow to provide a spatial chemical distribution of the components, which is fundamental for a correct forecast of their biocompatibility and bioavailability. For this reason, a ToF-SIMS imaging characterization can be essential to complete the studies around these systems because of the great contribution it provides to the understanding of these drug deliverers. ToF-SIMS was already employed for a general characterization of the SLNs' chemical composition[5]. So far, however, no imaging has been carried out on these systems and literature still misses a complete three-dimensional characterization.

SLNs imaging can represent a very challenging analysis to perform, regardless of imaging technique employed. In fact, these particles are dispersed in a solution and when deposited on a solid substrate they tend to aggregate. When the aggregation occurs, the images display a unique big cluster of particles and no detailed pictures of a single particle are obtained. Therefore, it is necessary to select a solid matrix which allow to stabilize each single SLN, avoiding the aggregation; in this way, it can be possible to investigate a single particle's morphology and, by means of ToF-SIMS, molecular composition. In this thesis, a ToF SIMS analyses and imaging of drug loaded SLNs are presented, by using a solid trehalose stabilizing matrix for the sample preparation.

## 2.1 SLNs chemical composition

As previously stated, thanks to their features, the development of solid lipid nanoparticles is one of the emerging fields of lipid nanotechnology in clinical medicine, as well as in other discipline. In fact, due to their unique size-dependent properties, lipid nanoparticles offer the chance to incorporate drugs and are considered generally well-tolerated, thanks to their composition based on physiologically similar lipids. This last feature allows to enable the pharmaceutical industry to overcome the lack of bioavailability for water-soluble drugs, since lipophilic molecules can be encapsulated and transport via lymphatic delivery is promoted. Therefore, they could be a great promise for attaining the bioavailability enhancement along with controlled and site-specific drug delivery.

In order to perform a clearer understanding of the results, a presentation about the chemistry of these systems is reported. The chemical composition of these systems is constituted by solid lipids with a mean initiate recrystallization (recrystallization can be initiated, e.g. by lyophilisation), typically spherical, with an average diameter between 10 and 1000 nanometres. They have a solid lipid core that can solubilize lipophilic molecules. The lipid core is stabilized by surfactants (emulsifiers). The lipidic composition can include triglycerides (e.g. tristearin), diglycerides (e.g. glycerolbahenate), monoglycerides (e.g. glycerol), fatty acids (e.g. stearic acid), steroids (e.g. cholesterol), and waxes (e.g. cetyl palmitate). As far as the content of emulsifiers is concerned, the choice depends on the charge and the molecular weight of the components to stabilize the lipid dispersion.

As said before, SLNs offer the possibility to incorporate a drug in order to carry it through the body and release it where is needed. There are different models of drugs encapsulation inside the SLNs' structure:

- solid solution model
- drug-enriched shell model
- drug-enriched core model

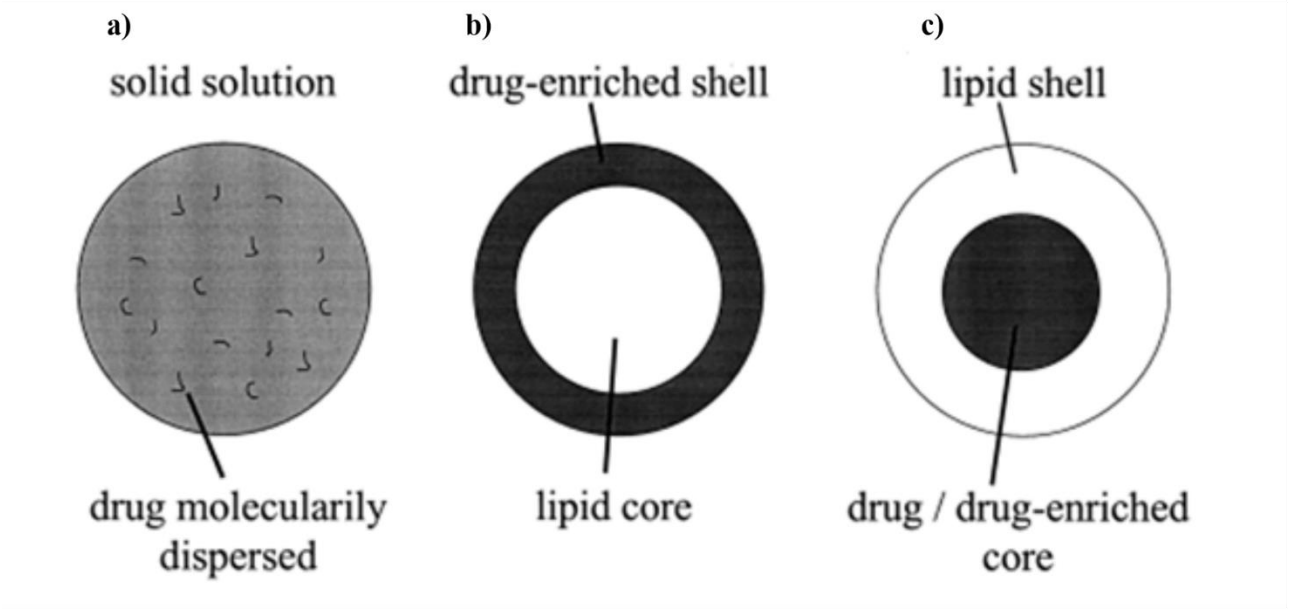


Figure 2.1: schematic depiction of the three models of drug encapsulation for SLNs, a) solid solution model, b) drug-enriched shell model, c) drug/drug-enriched core model.

In the case of the solid solution model (Figure 2.1 a), the drug is molecularly dispersed in the lipid matrix when the particles are produced by the cold homogenization technique using no surfactant nor drug-solubilizing surfactant. The drug must have strongly pronounced interactions with the lipid. In the drug-enriched shell model (Figure 2.1 b) of drug incorporation is concerned, a solid lipid core forms when the recrystallization temperature of the lipid is reached. By reducing the temperature of the dispersion, the drug concentrates in the still liquid outer shell of the SLN[6]. For the drug-enriched core model (Figure 2.1 c) of drug incorporation, the nano emulsion is cooled leading to a supersaturation of the drug, which is dissolved in the lipid melt at (or close to) its saturation solubility and the drug precipitates prior to lipid recrystallization. Further cooling finally leads to the recrystallization of the lipid surrounding the drug as a membrane[7].

The drug incorporation modality is crucial because it is strictly related to the drug release pattern and then its bioavailability. Moreover, the production method of SLN influences the final composition.

For instance, the drug-loaded lipid phase remains primarily in the solid state in the case of production by cold homogenization technique. Drug release is prolonged over several weeks since mobility of the drug molecularly dispersed in colloidal particles is very limited.

Even the particle size – the entire particle size due to the general formulation of the nanoparticle, including the additives such as surfactant/surfactant mixture, the amount of drug incorporated, the structural properties of lipids and drugs chosen – assumes an important role, affecting the drug release rate directly. The release process can be deduced through various parameters, such as the composition and the formulation of SLN, and conditions such as time, production temperature, equipment,

sterilization and lyophilisation. In some cases, the administration of SLNs with a certain structure rather than another could invalidate the therapy for a patient. It is possible to affirm that a chemical characterization of SLNs and their structure is a fundamental tool for the understanding of the chemistry of the drug encapsulation process and the evaluation of the particles' dimensions. Gaining this information can represent an excellent tool for a better design and formulation of this drug carrier system.

## 2.2 ToF-SIMS Imaging of SLNs

### 2.2.1 Prior ToF-SIMS investigations

Seeing as ToF-SIMS is one of the most powerful techniques for the chemical characterization of solids' surface, some research groups have already chosen this technique for the chemical investigation of SLN surfaces. In particular, ToF-SIMS can be extremely useful for evaluating the molecules' migration or in general composition modifications occurred after specific chemical treatments and procedures and to test the time stability of the system.

For instance, in 2016 Hilda Amekyeh et al. [8] investigated the stability of amphotericin B (AmB) and paracetamol (PAR) solid lipid nanoparticles with changes in particle surface chemistry. In particular, the aim of their work was the comparison of the AmB SLNs when challenged by simulated GI media and an identical SLN formulation containing paracetamol. Thanks to the differences between the ToF-SIMS spectra of the pure drugs, drug-free and drug-loaded SLNs, they were able to evaluate the encapsulation efficiency of the particles by following some characteristic diagnostic peaks of the molecules: AmB ($C_{47}H_{73}NO_{17}$, 923.49 g/mol), PAR ($C_8H_9NO_2$, 151.163 g/mol) on the SLNs and the drug-free SLNs. The showed peaks are $[C_{20}H_{27}O_2]$ at m/z 299.20, $[C_{20}H_{29}O_2]$ at m/z 301.22, $[C_{17}H_{21}NO_4]$ at m/z 303.23, and $[C_7H_7O]$ at m/z of 107.05 (Figure 2.2).

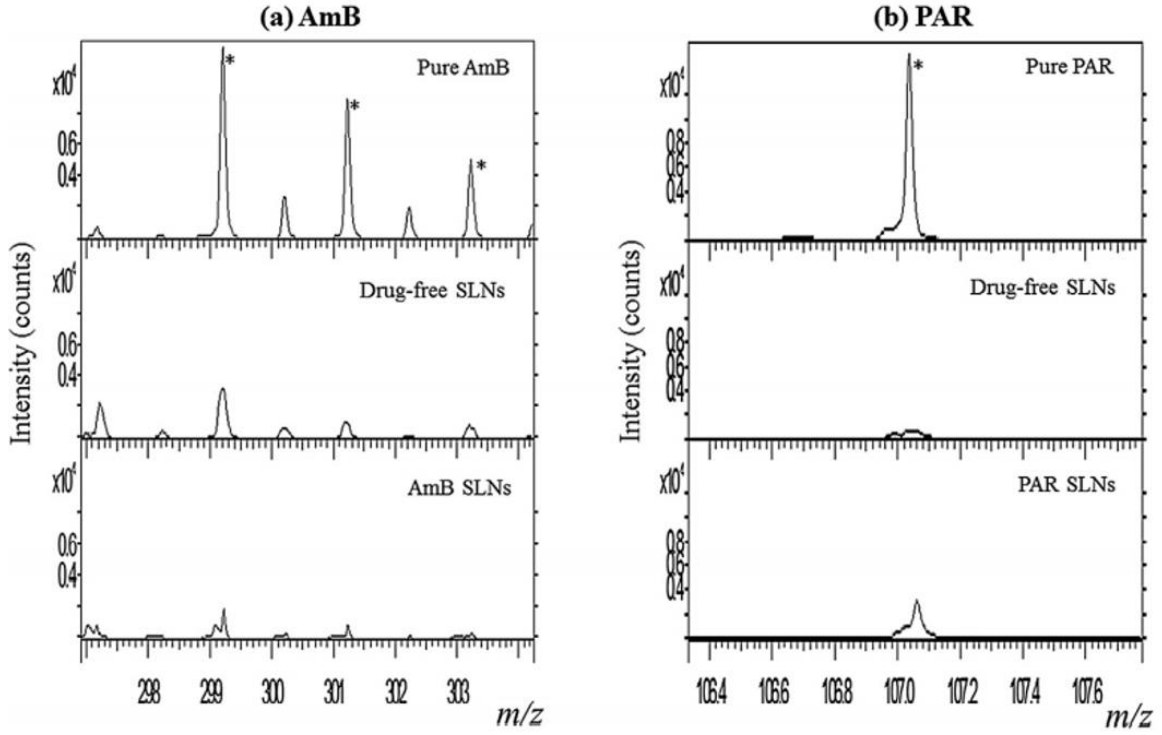


Figure 2.2: Negative ion ToF-SIMS spectra showing pure drugs [(a) AmB or (b) PAR], drug-free SLNs and the respective drug-loaded SLNs. [* = diagnostic peaks][8].

As a matter of fact, by comparing the peak intensities of the diagnostic ions in the pure AmB and the AmB SLNs spectra, the authors found out that the drug was present only in small quantities on the surface of the AmB SLNs. These small quantities could be due to the excipients in the formulation. These results proved the high encapsulation efficiency of 91.2 ± 3.0% obtained for the drug enriched AmB SLNs.

As far as the PAR SLNs is concerned, the authors showed that the intensity of the PAR diagnostic peak was higher on the drug-loaded SLNs than on the drug-free particles, which indicates that the peak intensity is a combination of the drug itself and the excipients. These results, therefore, indicate that there is a little amount of PAR on the surface of the fresh PAR SLNs, unlike the AmB SLNs, which had a negligible amount of AmB on the SLNs. Indeed, the PAR SLNs showed a relatively low encapsulation efficiency of 60.7 ± 0.26%

Via ToF-SIMS analyses, the researchers could also test the stability of the systems in different media. The results are showed in Figure 2.3.

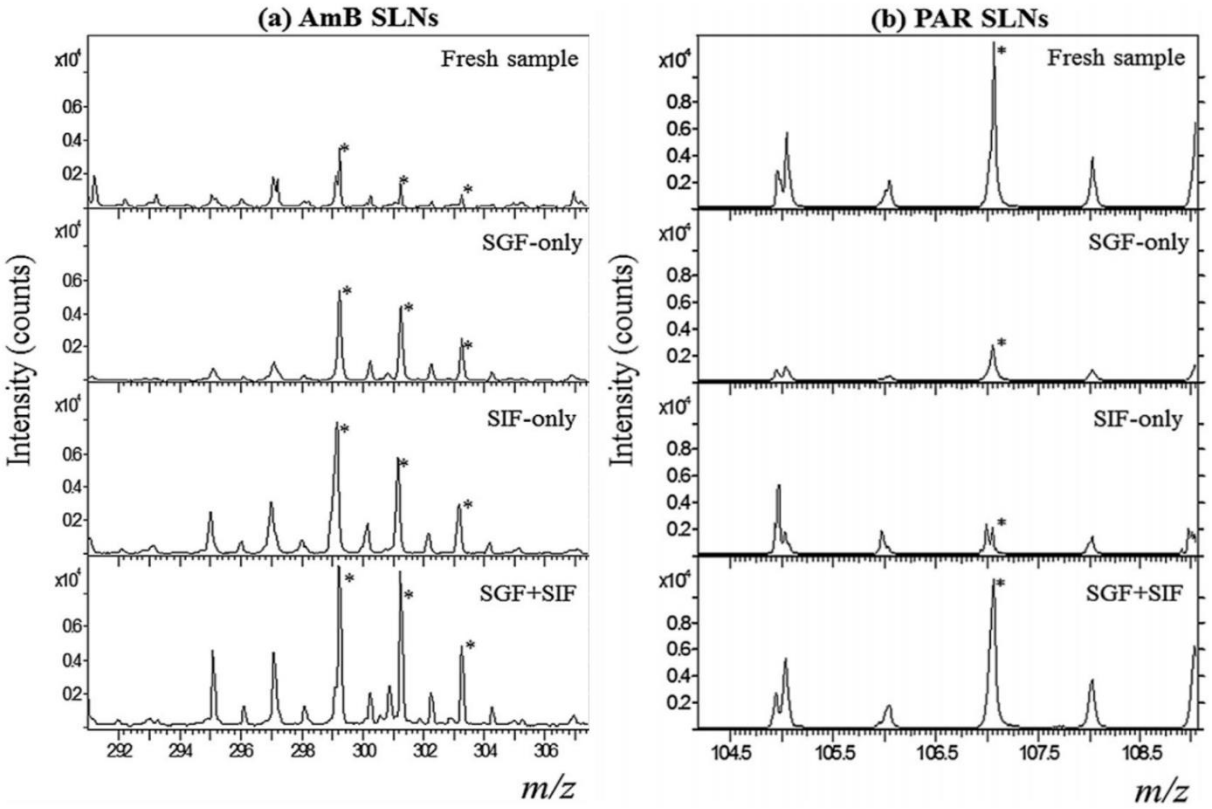


Figure 2.3: Negative ion ToF-SIMS spectra showing the drugs [(a) AmB or (b) PAR] on the surface of the respective fresh SLNs and after their incubation in simulated GI fluids. [* = diagnostic peaks][8]

For the AmB SLNs, it was observed that higher drug counts were detected on the particles after the exposure to the SGF + SIF medium. These higher intensities were correlated to the diffusion of AmB towards the surfaces of the SLNs. For the PAR SLNs, the spectra showed more intense PAR counts on the fresh PAR nanoparticles in comparison to those incubated in the media. As a matter of fact, PAR tends to undergo different chemical modifications in the different media. In particular, it is hydrolysed in acidic solutions (SGF) and furthermore it is very soluble at the pH of SIF. These chemical reactions in the media can bring to a low PAR count on the particles. As with the AmB SLNs, the highest drug intensity was detected on the PAR SLNs after their incubation in SGF + SIF, which means that there is a higher rate of drug diffusion out of the particles in SGF + SIF and , therefore, this is the best dissolution medium for both drugs.

The results showed that ToF-SIMS analyses were able to indicate that drug loading typology for these SLNs possibly followed the core-shell model and that the AmB SLNs may have a more drug-enriched core than the PAR SLNs do. Furthermore, they could give information about the stability of the SLN formulations in the simulated GI media. This paper is an example of the potential applications of the ToF SIMS analysis on SLNs. In fact, it can allow for the investigation of the chemistry of these systems and, therefore, to give more information about their suitability for oral delivery. Significantly,

ToF-SIMS has high potential to investigate the SLNs' three-dimensional structure in order to acquire more detailed information on the drug loading efficiency and their stability. By plotting the distribution of chemical compounds against position with submicrometric resolution, a chemical map of the SLN as a function of depth from the surface can be generated, which so far is missed in literature. In this way, the encapsulation efficiency of the drug loaded into the particles can be directly verified.

### 2.2.2 Single particle imaging issue

As said, other imaging techniques were already used to study SLNs' shape and dimension. However, carrying out ToF-SIMS imaging can be a great tool to combine the spatial information with the molecular, thanks to the high spatial and mass resolution that this technique can offer. The study of single solid lipid nanoparticle presents significant challenges due to the fundamental complexity associated with any drug delivery system. Sample preparation is of critical importance in controlling this complexity, owing to the instable nature of these systems and to the need to characterize them in their pristine state, free of chemical or physical changes. As a matter of fact, this ToF-SIMS imaging analysis requires first a solid sample suitable for ultra-high vacuum which allows to keep separated the particles and an instrument set-up which permit to maintain high spatial and mass resolution in order to identify some diagnostic fragments in the spectra.

As far as sample preparation is concerned, biological samples, as well as structured organic samples, are the most challenging. Due to the ultrahigh-vacuum conditions typically required for a ToF-SIMS experiment, special precautions must be taken to conserve sample integrity. To obtain mass spectral data with sufficient quality, both substrate and sample preparation must be chosen in order to maintain the shape and distribution of sample chemical components[9].

Generally, biological samples like cells need to be fixed either cryogenically or chemically. Thus, commonly used sample preparation methods include chemical fixation, freeze fracturing, frozen hydration and freeze-drying[10,11]. Yet, all these techniques modify the chemical composition of the biological samples. Moreover, certain samples tend to collapse, causing the lack of dimensional localization and curvatures. To solve this issue, a different approach was tested in the 2000s: finding a stabilizing matrix that simplistically preserves native three-dimensional composition while enhancing lateral resolution[9]. In particular, the use of trehalose was successfully demonstrated[12]. In fact, trehalose is a disaccharide of glucose where two cyclic glucopyranose constituents are bound by their reducing, anomeric α-carbons, making it a nonreducing sugar. Under dry conditions, this disaccharide is particularly resistant to crystallization and, if desiccated, it forms a highly viscous

amorphous glass, which stabilizes entrained biomolecules. The extreme viscosity allows to prevent the movement and diffusion of the samples' constituents, effectively "freezing" the various component in the space. From preliminary analyses, it was possible to verify that this sugar has a high sputtering yield under ion bombardment. Therefore, the trehalose matrix can be eroded quite fast and avoids degradation phenomena or carbonification, even without the use of cluster ion beams.

## 2.3 Thesis Work

In this thesis work, ToF-SIMS analyses and imaging of drug loaded SLNs will be presented. The particles' core is constituted of Compritol® 888 ATO, which is a mixture of long chain fatty acid, triglycerides, and other species; Lutrol® F-127 was employed as surfactants. Both these mixtures are covered from proprietary secret; therefore, preliminary analyses of the single SLNs' components had been necessary to achieve information of their own composition. Moreover, the SLNs were loaded with an anti-inflammatory drug, more specifically Palmitoylethanolamide which belongs to the o the class of nuclear factor agonists and it exerts several biological effects related to chronic inflammation and pain; in order to facilitate the acquisition of high spatial resolution images, the average dimension of the synthetized SLNs was purposely around 1 micron.

In order to perform this imaging study, a solid stabilizing matrix was employed for the sample preparation. After literature had been consulted and several attempts were carried out, it was found out a trehalose matrix can give promising results. This research had the aim to not only to present three-dimensional images of SLNs, but also to demonstrate to the scientific community a successful and efficient procedure to enable a rigorous chemical study of these systems in a pristine state. In so doing, provide a pathway to enhance and improve SLNs for the purpose of drug delivery.

## 2.4 Materials and Methods

The SLNs were furnished by Professor Puglia (University of Catania, Department of Pharmaceutical Science), together with the main commercial products used for the synthesis process: Compritol® 888, Lutrol® F-68, and Palmitoylethanolamide (PEA). The particles dimension (around 1 μm) was also provided by means of specific analysis techniques by Prof. Puglia's research team. The particles were provided as an aqueous dispersion and the concentration was unknown.

For the sample preparation, first the aqueous dispersion was properly diluted (1:10 ratio in milliQ water) and dropped directly on Si wafer; successively, the diluted SLNs dispersion was added in a trehalose solution (3% in milliQ water), then deposited on Silicon wafer by drop casting and let it dry

overnight. For reference, each single components of the synthesis mixture, as well as the pure solution of trehalose, were dropped on Si wafer and let them dry.

The ToF-SIMS analyses were carried out by a ToF SIMS IV spectrometer (IONTOF, Germany), equipped with a LMIG Bismuth source, and with a dual source (Fullerene and Cesium) ion gun. $Bi_3^+$ was employed as analysis beam, with average energies of 50 KeV (0.5 pA). The analyses were acquired both for the drug loaded SLNs on Si and for the single components used for the synthesis on Si, as well as for the drug loaded SLNs dispersed in the trehalose matrix and the pure trehalose matrix. For the so-called "bunched mode" (BU) the bismuth beam was operated at 10 kHz (resolution M/ΔM of 7000 measured at m/z 29); the $Bi3^+$ dose delivered to the sample during each analysis cycle was of the order of $10^{10}$ ions $cm^{-2}$.

For all same samples, burst alignment (BA) mode analyses were likewise acquired. In the burst mode, the long pulses (170 ns in this study) are cut into a burst of successive short ion pulses by a sine blanker operating at 40 MHz (i.e., 6 pulses of 2 ns every 25 ns). In the burst alignment mode, the ion beam is not bunched to avoid the energy dispersion that causes the degradation of the spatial resolution. The nominal mass resolution was around e000 in BU mode, and >5000 in the BA mode.

By combining imaging with molecular depth profiling, a complete 3-dimensional rendering of the particles was possible. Bi3 + was typically rastered over a 200 × 200 $\mu m^2$ area, centered inside a 500 × 500 $\mu m^2$ $C_{60}^{++}$ crater. Target currents were measured separately before each measurement in the pulsed mode for $Bi_3^+$ and in the direct current mode for $C_{60}^{++}$. More specifically, the $Bi_3^+$current was 0.2 pA in the BU mode (< 1 ns pulse width) and 0.08 pA in burst alignment (100 ns pulse width); the $C_{60}^{++}$ current was between 0.15 and 1 nA. All images were reconstructed in false colours employing the ION-TOF palette *Thermomap1*.

## 2.5 Results and Discussion

### 2.5.1 ToF-SIMS preliminary analyses

Figure 2.4 shows **a)** the negative spectrum of the PEA loaded SLNs on Si, **b)** the negative spectrum of pure PEA on Si and **c)** the negative spectrum of Compritol® 888 ATO on Si.

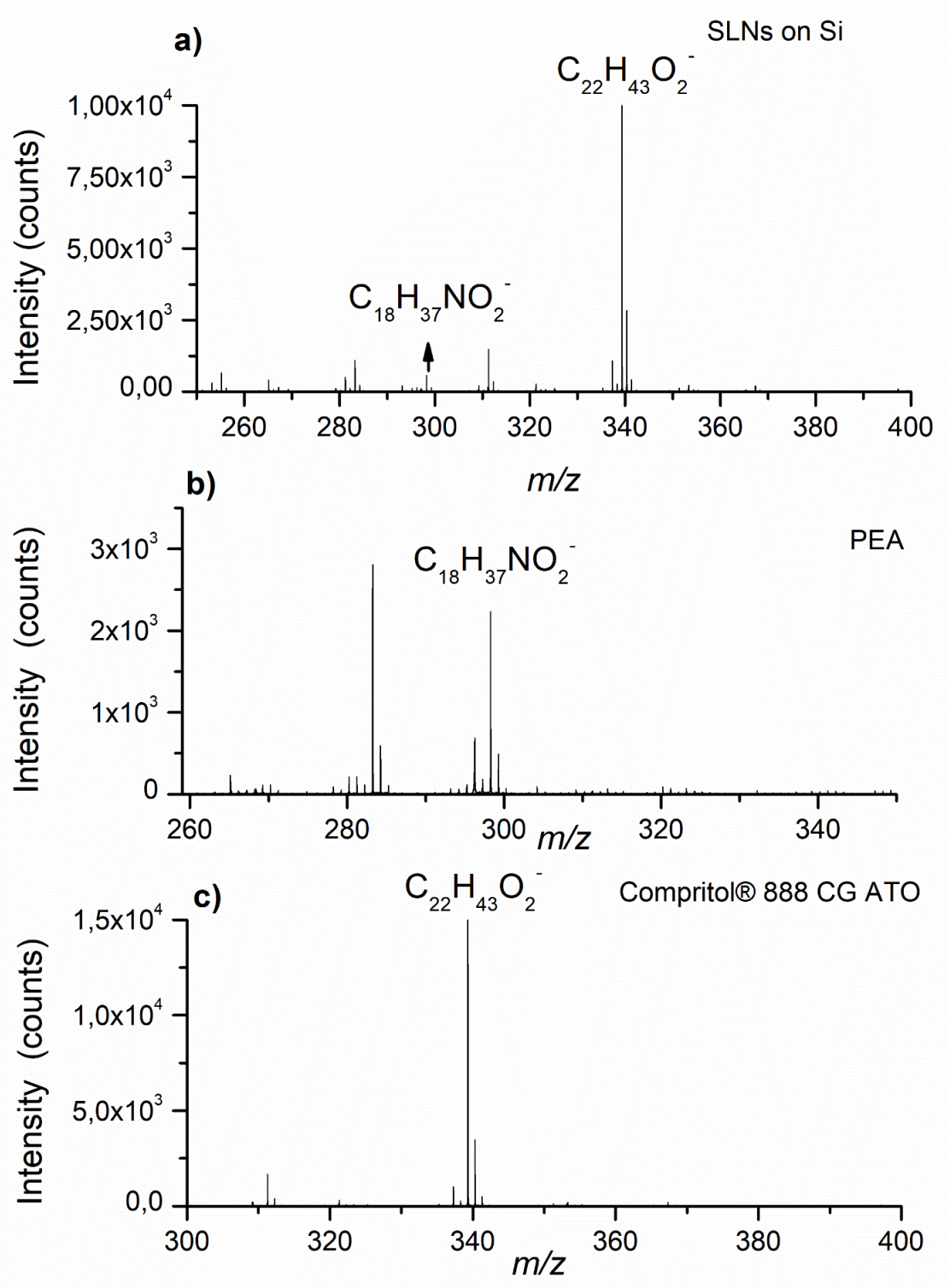


Figure 2.4: negative spectra of **a)** of SLNs on Si; **b)** PEA on Si; **c)** Compritol® 888 ATO on Si

As mentioned, Compritol® 888 ATO is a mixture of long chain fatty acid, triglycerides and other species and it constitutes the solid structure of the particles. It is generally utilized as lipid excipient, in particular in cosmetic industry as viscosity-inducing agent in emulsions or creams. It is made of a blend of different esters of behenic acid with glycerol. Behenic acid (also known as decosanoic acid),

is a carboxylic acid with formula $C_{21}H_{43}COOH$ (molar mass 340.592 $g \cdot mol^{-1}$). The chemical structure is shown in Figure 2.5.

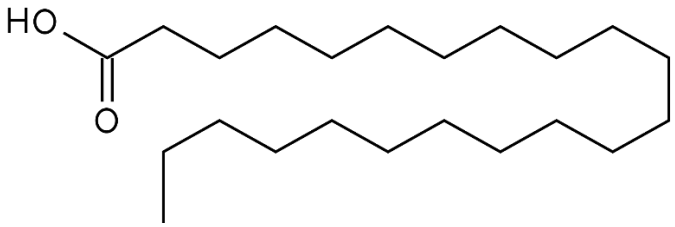


Figure2.5 : Behenic Acid structure

The anti-inflammatory drug (PEA) is a fatty acid amide: the chemical formula is $C_{18}H_{37}NO_2$ and the molar mass 299.499 $g \cdot mol^{-1}$. The chemical structure is shown in Figure 2.6.

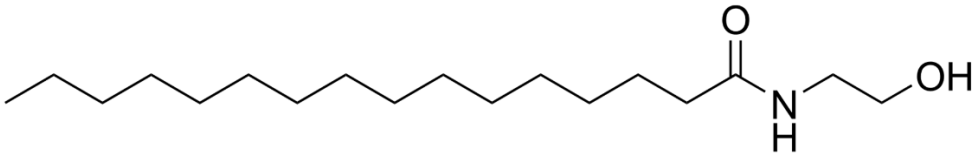


Figure2.6: Palmitoylethanolamide structure

It is possible to discriminate in Figure 2.4 **c)** the molecular peak of behenic acid ($[M-H]^-$: $C_{22}H_{43}O_2^-$ *m/z* 339.3), and in Figure 2.4 **b)** the molecular peak ($[M-H]^-$: $C_{18}H_{37}NO_2^-$) of PEA at *m/z* 299.3. Figure 2.4 **a)** shows that the ToF-SIMS analyses allowed to reveal both molecular fragments in the sample. Table 2.1 and 2.2 show the cluster isotopic distribution detected in the negative spectrum, respectively of behenic acid molecular peak $C_{22}H_{43}O_2^-$, and PEA molecular peak $C_{18}H_{37}NO_2^-$, with the relative standard deviations.

Table 2.1: cluster isotope distribution of $C_{22}H_{43}O_2^-$

| **Peak** | **Theoretical *m/z*** | **Detected *m/z*** | **Standard deviation (%)** |
|---|---|---|---|
| $C_{22}H_{43}O_2^-$ | 339.3263 | 339.3090 | -52.6 |
| $^{13}CC_{21}H_{43}O_2^-$ | 340.3297 | 340.3083 | -64.1 |
| $^{13}C_2C_{20}H_{43}O_2^-$ | 341.3330 | 341.3111 | -63.7 |
| $C_{22}H_{43}{}^{18}OO^-$ | 341.3306 | 341.3198 | -61.7 |

Table 2.2: cluster isotope distribution of $C_{18}H_{37}NO_2^-$

| Peak | Theoretical *m/z* | Detected *m/z* | Standard deviation (%) |
|---|---|---|---|
| $C_{18}H_{37}NO_2^-$ | 299.2830 | 299.2732 | -32.7 |
| $^{13}CC_{17}H_{37}NO_2^-$ | 300.2863 | 300.2676 | -62.2 |
| $^{13}CC_{16}H_{37}NO_2^-$ | 301.2897 | 301.2698 | -66.04 |

Figure 2.7 shows the positive spectra of **a)** SLN sample on Si **b)** PEA on Si and **c)** Compritol® 888 ATO on Si.

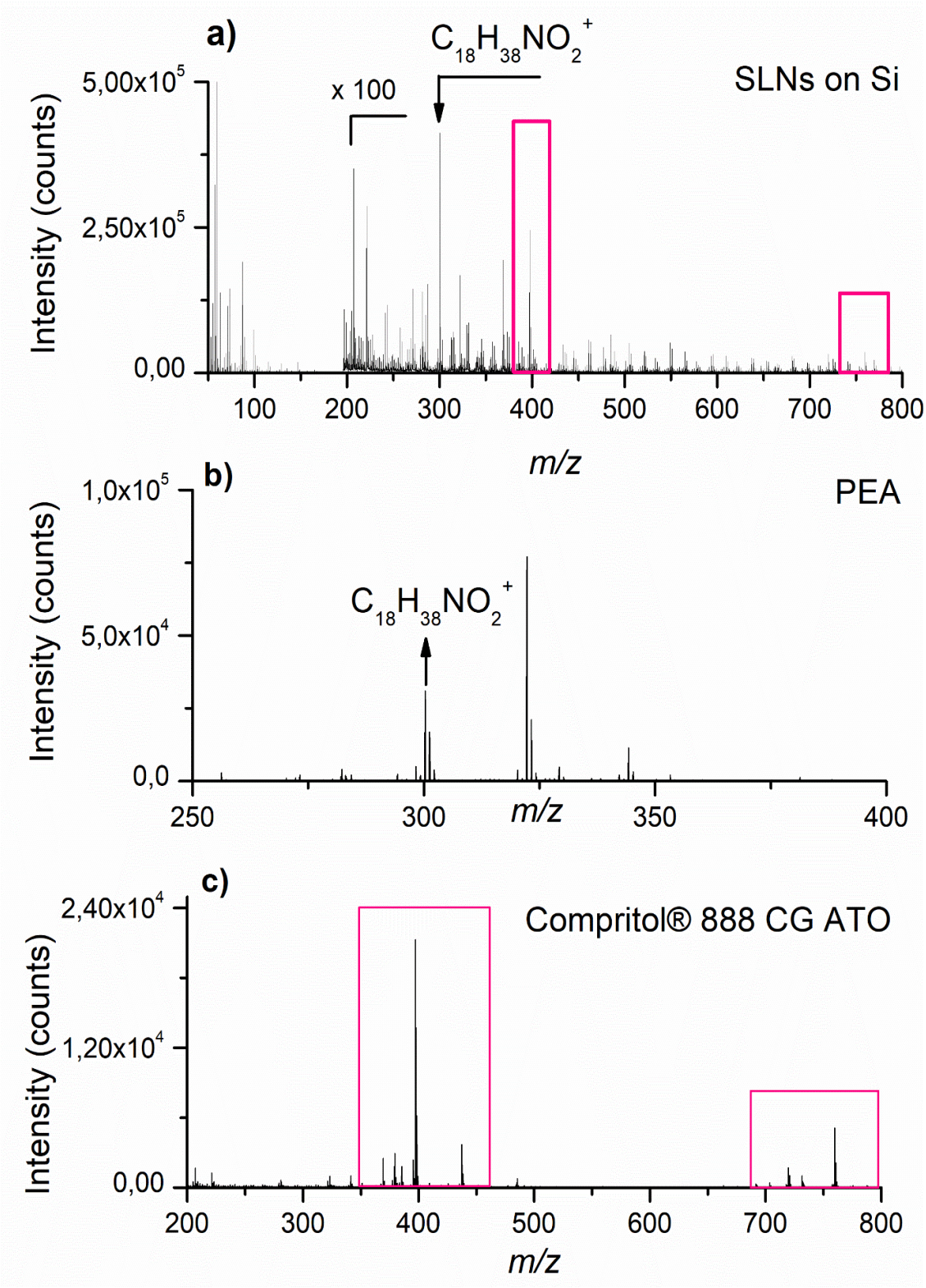


Figure 2.7: positive spectra of **a)** SLNs on Si **b)** PEA on Si and **c)** Compritol® 888 ATO on Si

In the positive spectrum of PEA (figure 2.7 **b)** it is possible to see the molecular peak $[M+H]^+$ ($C_{18}H_{38}NO_2^+$) of the drug at *m/z* 300.3. Additionally, a strong peak is observed at m/z 322, which is

the adduct of PEA plus sodium $[M+Na]^+$. The sodium likely comes from the solution provided by Prof. Puglia. On the other hand, the molecular peak of behenic acid is not present in the positive spectrum of Compritol® 888 ATO. Indeed, since it is a carboxylic acid, its emission as positive ion is not favourable. Nevertheless, some characteristic peaks in the regions of 400 and 750 *m/z* are observed. These typical fragments together with PEA molecular peak were found in the positive spectrum of the sample (Figure 2.7 **a)**).

These preliminary spectra are indeed extremely rich of peaks. However, it was not possible to provide a rigorous assignment for most of these signals. Indeed, Compritol® 888 ATO is a very complex mixture of several substances and the detailed composition is subject to trade secret. Yet, this product constitutes the structure of the particles and therefore it is deduced that most of the spectral peaks come from the Compritol® 888 ATO composition. Moreover, the PEA diagnostic peak is perfectly visible in the particles' spectra. Thus, it is reasonable to expect the drug is also on the surface of the particles.

### 2.5.2 High mass resolution Imaging

Even though the BU mode does not allow for high spatial resolution, these analyses are fundamental to study the signals of the samples' components in high mass resolution in order to permit an easier peak attribution and identification in the high lateral resolution analyses. These preliminary secondary ions images showed the presence of several regions with different chemical composition. One of the regions was characterized by molecular fragments of Lutrol® F-127. As specified, Lutrol® F-127 is a mixture of polymers, including polyethylene oxide and polypropylene oxide, which as surfactants allow the suspension of the particles in a water solution. The chemical structures of the main components are shown in Figure 2.8.

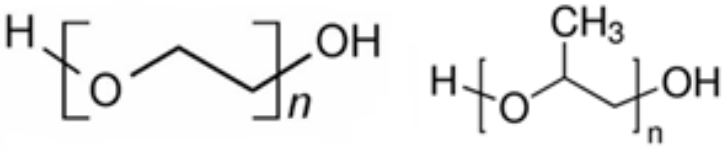


Figure 2.8: polyethylene oxide structure (left); polypropylene oxide structure (right)

In Figure 2.9 **b)** some diagnostic regions of Lutrol® F-127 positive spectrum (coloured boxes) are pointed out; the same sequences of peaks were found in the positive spectrum of the sample (Figure 2.9 **a)**).

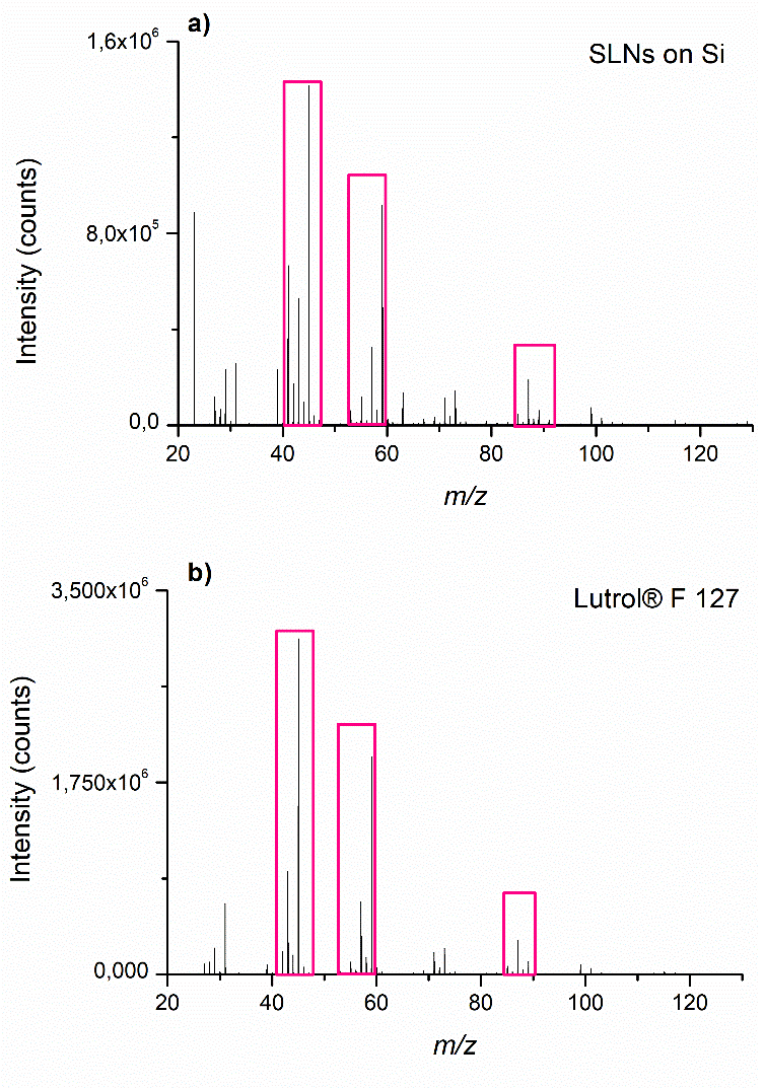


Figure 2.9: positive spectra of a) SLNs on Si (top) and b) Lutrol® F-127 on Si

Figure 2.10 shows the secondary ions images in false colours of some signals of PEA-SLNs on Si acquired in BU mode (positive polarity). In particular, the spatial distribution of **a)** signal at *m/z* 87.06, **b)** signal of the substrate $Si^+$ at *m/z* 27.9, **c)** PEA molecular signal $C_{18}H_{38}NO_2^+$ at *m/z* 300.3 and **d)** the overlay of *m/z* 87.06 (blue), $C_{18}H_{38}NO_2^+$ (red) and $Si^+$ (green).

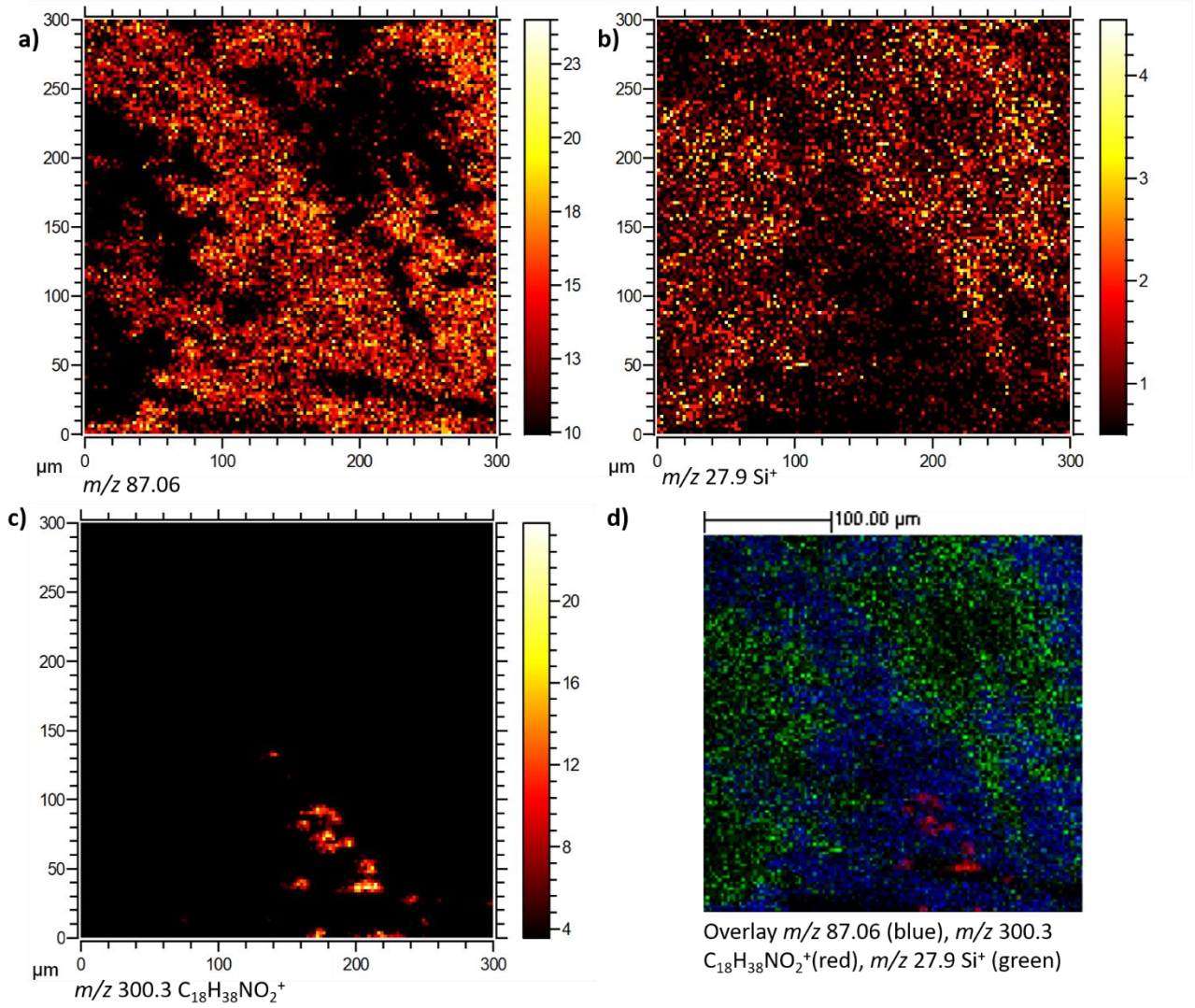


Figure 2.10 : HCBU images of SLNs on Si (positive polarity) of **a)** *m/z* 87.06, **b)** Silicon substrate signal ($Si^+$), **c)** PEA molecular signal, d) overlay of *m/z* 87.06 (blue), $C_{18}H_{38}NO_2^+$ (red), $Si^+$ (green)

It is possible to see that the PEA molecular signal $C_{18}H_{38}NO_2^+$ at *m/z* 300.3 is all concentrated in a certain region of the chemical map, which reveals the presence of some aggregated particles. In fact, in this chemical map, the particles' dimension ranges from 50 to 200 μm. The signal at *m/z* 87.06, characteristic of Lutrol® F-127 reveals that the surfactant mixture spread through the substrate surface after the solution deposition. In the solution, as well known, the surfactant's role is the stabilization of the particles. This can occur by means of repulsive surface charges or for a steric effect. It is conceivable that the aggregation phenomenon is increased by the spread of the surfactant mixture, which is not able to surround the particles and therefore stabilize them.

Figure 2.11 shows BU secondary ions images in negative polarity of **a)** PEA molecular peak, $C_{18}H_{37}NO_2^-$, at *m/z* 299.3; **b)** *m/z* 121.03 signal, **c)** Compritol® 888 ATO molecular peak $C_{22}H_{43}O_2^-$ at *m/z* 399.3; **d)** a characteristic signal of Lutrol® F-127 at *m/z* 85.3 signal; **e)** the overlay of $C_{18}H_{37}NO_2^-$(green), *m/z* 121.03 (red), $C_{22}H_{43}O_2^-$ (blue), *m/z* 85.3 (yellow).

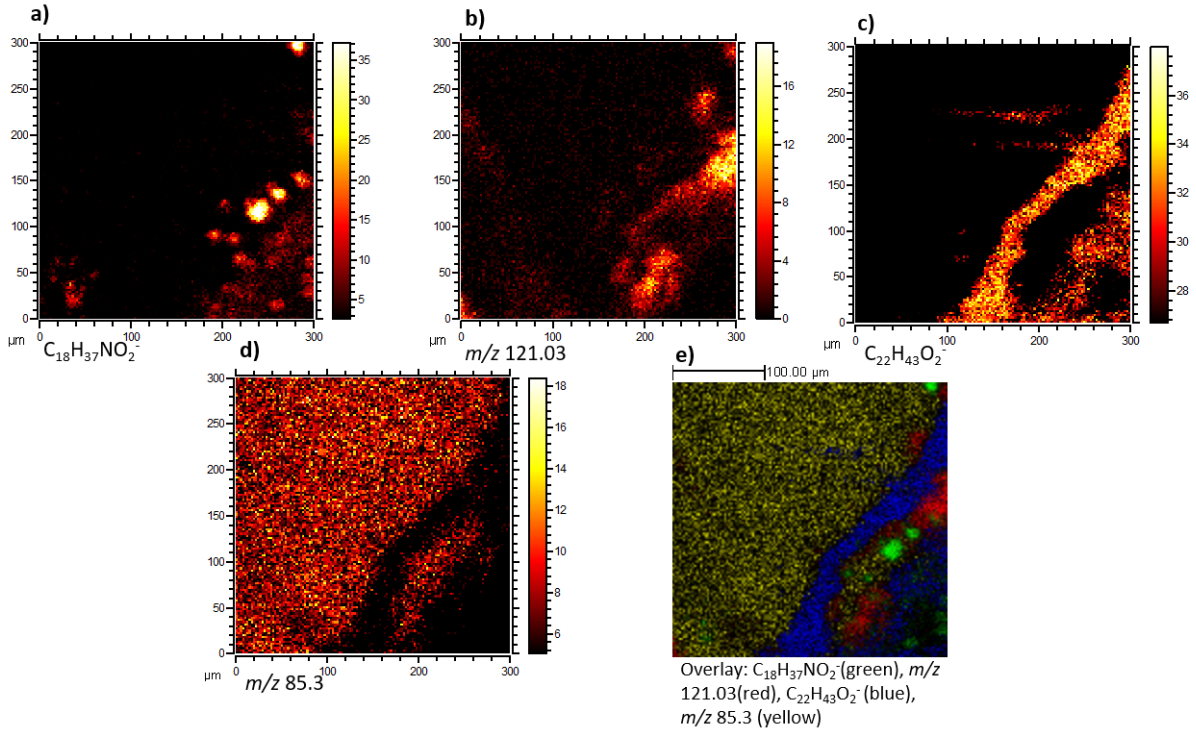


Figure 2.11: negative HCBU chemical map in false coloured of **a)** PEA molecular peak $C_{18}H_{37}NO_2^-$ at *m/z* 299.3; **b)** *m/z* 121.03 signal, **c)** Compritol® 888 ATO molecular peak $C_{22}H_{43}O_2^-$ at *m/z* 399.3; **d)** *m/z* 85.3 signal; **e)** the overlay of $C_{18}H_{37}NO_2^-$(green), *m/z* 121.03 (red), $C_{22}H_{43}O_2^-$ (blue), *m/z* 85.3 (yellow)

The signal at *m/z* 121.03 belongs likely to another component of Compritol® 888 ATO as we can observe in figure 2.12, which shows the comparison between the negative spectra of SLNs on Si (top) and Compritol® 888 ATO on Si. Indeed, it is possible to observe the same peak at *m/z* 121.03 in both spectra. These negative secondary images reveal again the presence of aggregated particles and the diffusion on the substrate's surface of the Lutrol. In addition, it is possible to the separation between the lipidic structure of the particles and the drug.

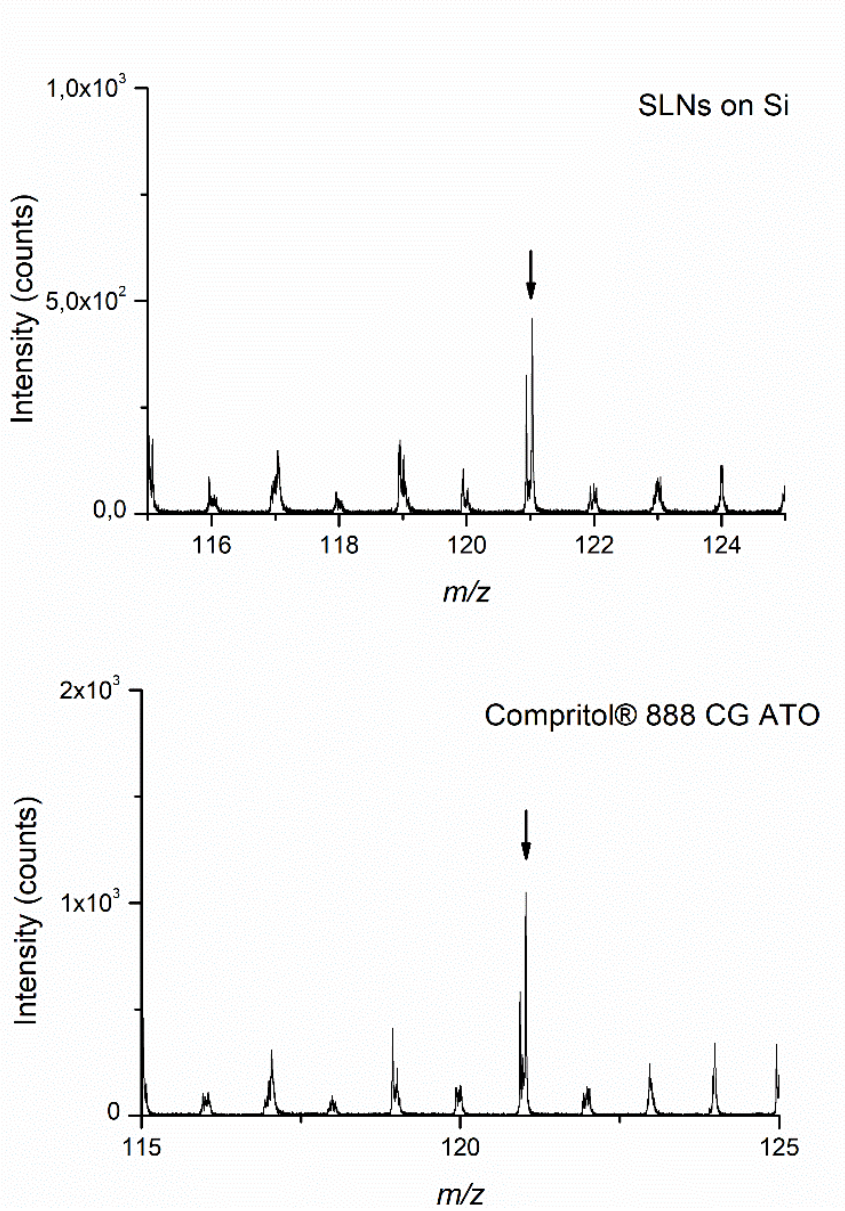


Figure 2.12: negative spectra of SLNs on Si (top) and Compritol® 888 ATO on Si (bottom)

In both positive and negative chemical maps, it is evident that this sample preparation methodology does not allow the investigation of the particles' structure. In fact, dropping the SLN emulsion directly on the substrate entails an agglomeration of the particles. This agglomeration phenomenon is probably caused by the decay of the electrostatic interactions (coulomb forces), which maintain the particles in solution. As a matter of fact, by measuring the size of the particles (figure 2.13), it is possible to estimate the diameter dimension around 25 µm, which is a considerably larger compared to the expected value.

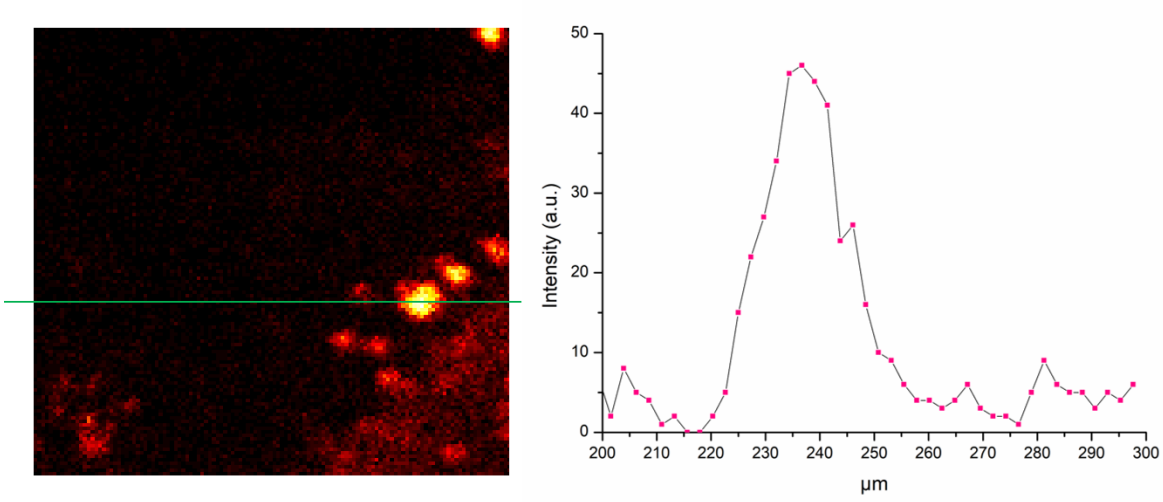


Figure 2.13: line scan of signal intensity to highlight the size of a single particle.

### 2.5.3 ToF-SIMS imaging by using a solid trehalose matrix

As stated before, literature reports the use of matrixes only for biological samples which are particularly challenging from a sample preparation point of view. However, as well as biosamples, the solid lipid nanoparticles represent a difficult sample to analyse with a quite complex three-dimensional structure. For this reason, utilizing a trehalose matrix for these particles was considered favourable and remarkable.

BU trehalose spectra were acquired in both polarities, in order to highlight some characteristic fragments which are not overlapped with other component signals. Figure 2.14 shows the positive spectra of drug loaded SLNs dispersed on the trehalose matrix and dropped on Si (top) and trehalose on Si (bottom). It is possible to observe a characteristic region on trehalose positive spectrum from *m/z* 99 to 101 (displayed in coloured box), which is also present in the sample positive spectra (displayed in coloured box) and it do not overlap with other components' characteristic fragments. The matrix characteristic fragments in the SLNs spectra are explained by the presence of trehalose also in the surface of the particles since it covers and surrounds the entire system.

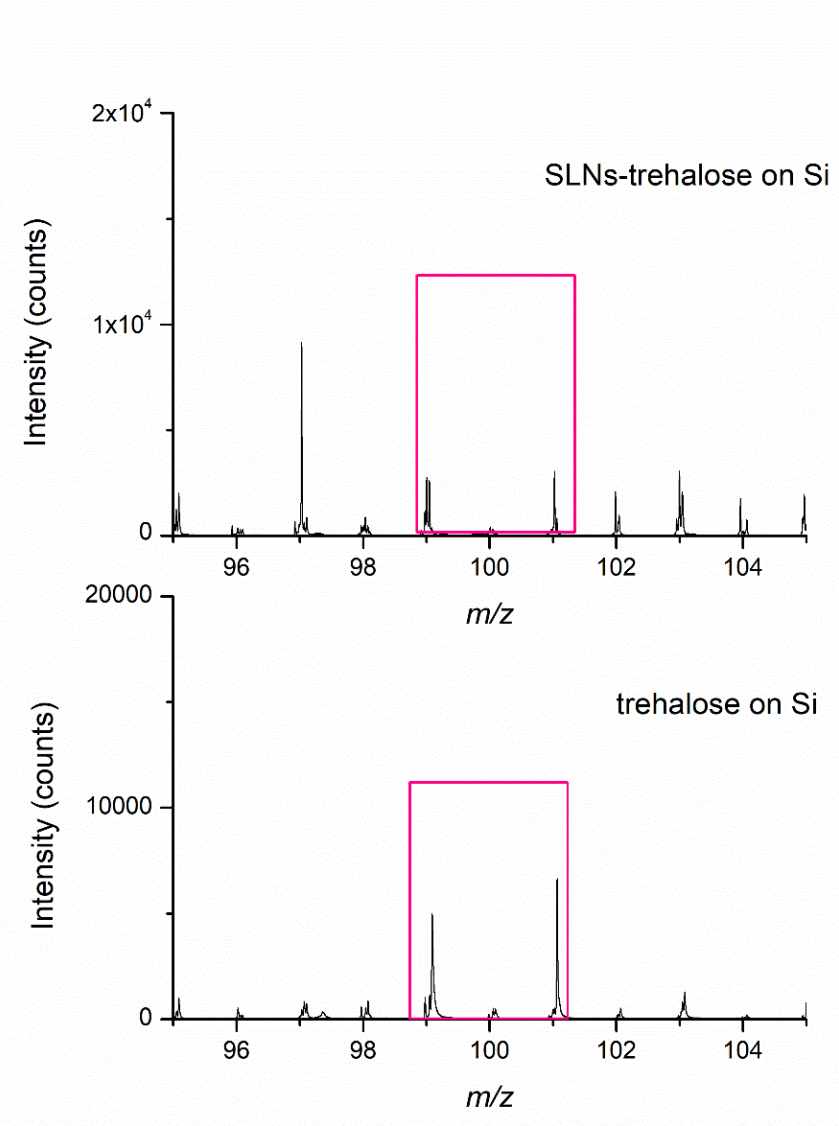


Figure 2.14: positive spectra of SLNs dispersed on a trehalose matrix on Si (top) and trehalose on Si (bottom)

In order to confirm that this sample preparation methodology allows to avoid the particles agglomeration and to investigate on the particles dimension in the sugar matrix, BU secondary ions images were acquired. Figure 2.15 shows the BU chemical maps (positive polarity) of **a)** PEA molecular peak $C_{18}H_{38}NO_2^+$ at *m/z* 300.3, **b)** a characteristic peak of trehalose at *m/z* 101.07, **c)** overlay of $C_{18}H_{38}NO_2^+$(red) and *m/z* 101.07(green).

It is evident from these images that the agglomeration of the particles was avoided, allowing to observe the single particles inside the trehalose matrix. The overlay of the chemical maps reveals how the trehalose matrix can surround the particles. It is presumable that after the deposition of the solution the sugar crystalize around the particles preventing the agglomeration. As a matter of fact, the measure of the particles' dimension showed a diameter around 2 µm (Figure 2.16).

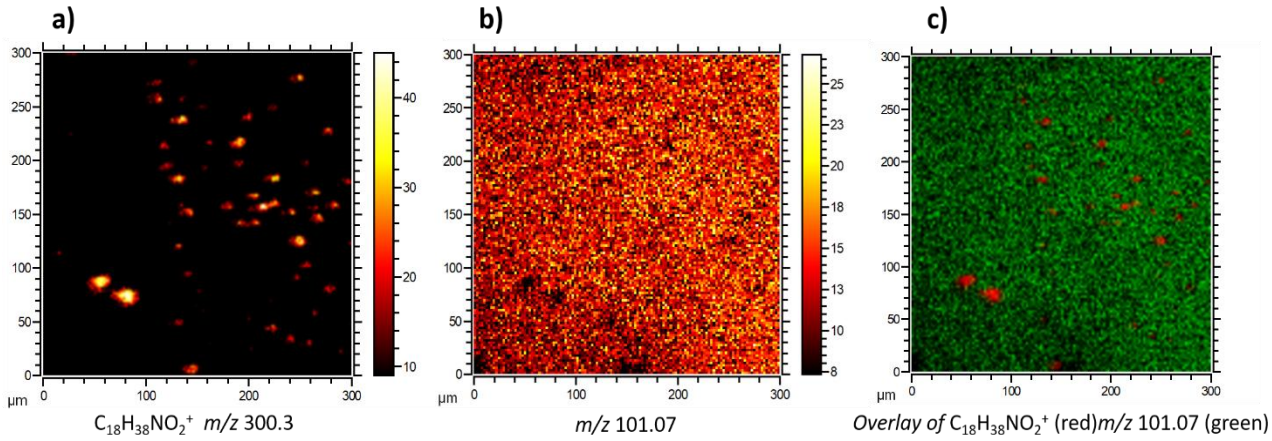


Figure 2.15: positive chemical maps of **a)** $C_{18}H_{38}NO_2^+$ at *m/z* 300.3, **b)** *m/z* 101.07, **c)** overlay of $C_{18}H_{38}NO_2^+$(red) and *m/z* 101.07(green)

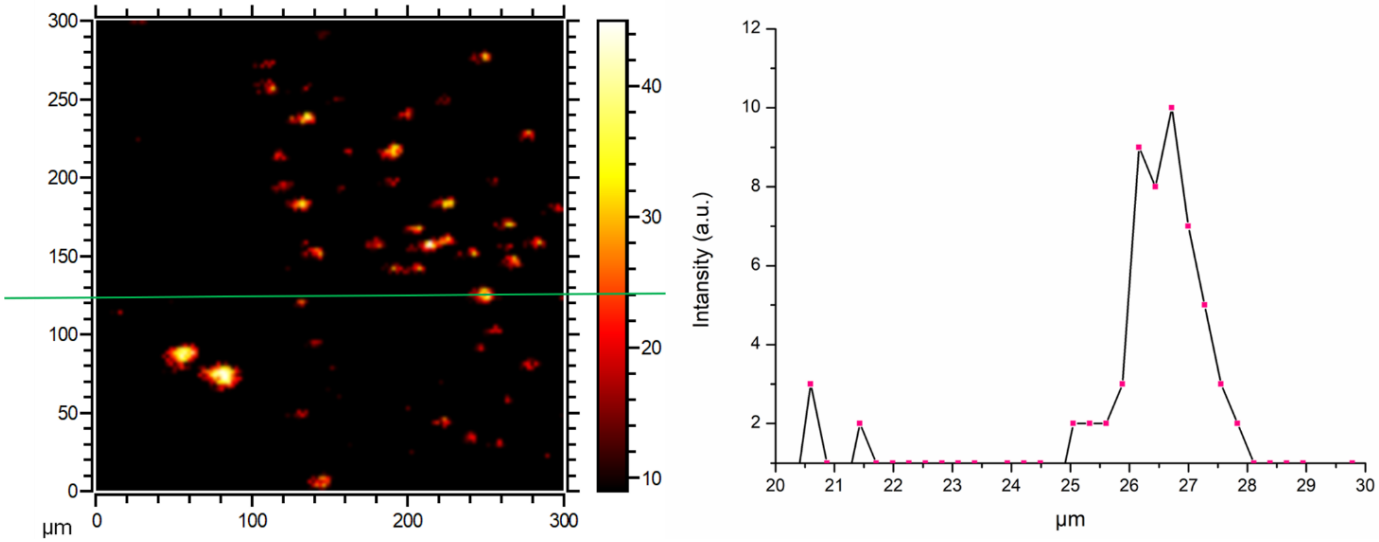


Figure 2.16: measure of the particles dimension

## 2.5.4 High spatial resolution imaging

For obtaining high spatial resolution images, BA mode analyses were carried out. Figure 2.17 displays high lateral resolution chemical maps of **a)** the sum of two characteristic signals of Compritol® 888 ATO at *m/z* 339.3 and 721.2, **b)** trehalose characteristic peak at *m/z* 101.07 **c)** PEA molecular peak at $C_{18}H_{38}NO_2^+$ *m/z* 300.3 and **d)** the overlay of $C_{18}H_{38}NO_2^+$ *m/z* 300.3 (red), *m/z* 101.07 (green), *m/z* 339.3 (blue).

The BA mode permitted to drop to smaller framing (50 × 50 µm$^2$) achieving a more define sight of the particles. The high lateral resolution distinguished even the smallest particles in the trehalose

matrix and enabled correct identification of the signals by comparing them with the BU high mass resolution spectra.

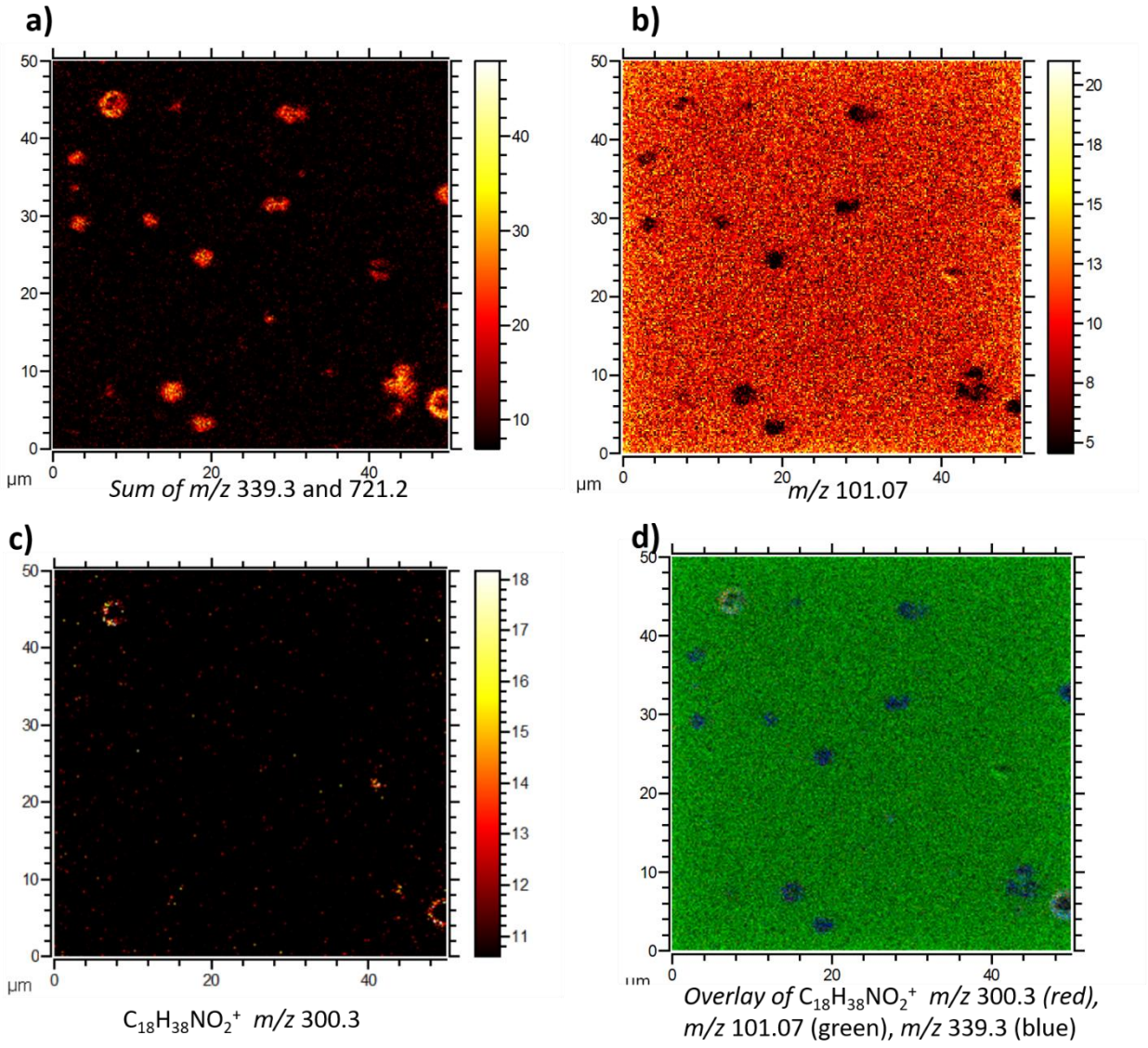


Figure 2.17: high lateral resolution chemical maps of **a)** sum of two characteristic peaks of Compritol® 888 ATO *m/z* 339.3 and 721.2, **b)** trehalose characteristic peak *m/z* 101.07 **c)** PEA molecular peak $C_{18}H_{38}NO_2^+$ *m/z* 300.3 **d)** overlay of $C_{18}H_{38}NO_2^+$ *m/z* 300.3 (red), *m/z* 101.07 (green), *m/z* 339.3 (blue)

Figure 2.18 shows 3D high lateral resolution images of **a)** the sum of *m/z* 339.3 and 721.2, characteristic signals of Compritol® 888 ATO, **b)** PEA molecular peak at $C_{18}H_{38}NO_2^+$ *m/z* 300.3, **c)** the sum of trehalose characteristic signal at *m/z* 101.07 and Lutrol® F-127 characteristic signal at 87.06, **d)** the overlay of sum of *m/z* 339.3 and 721.2 (blue), $C_{18}H_{38}NO_2^+$ *m/z* 300.3 (red) and sum of *m/z* 101.07 and 87.06 (green).

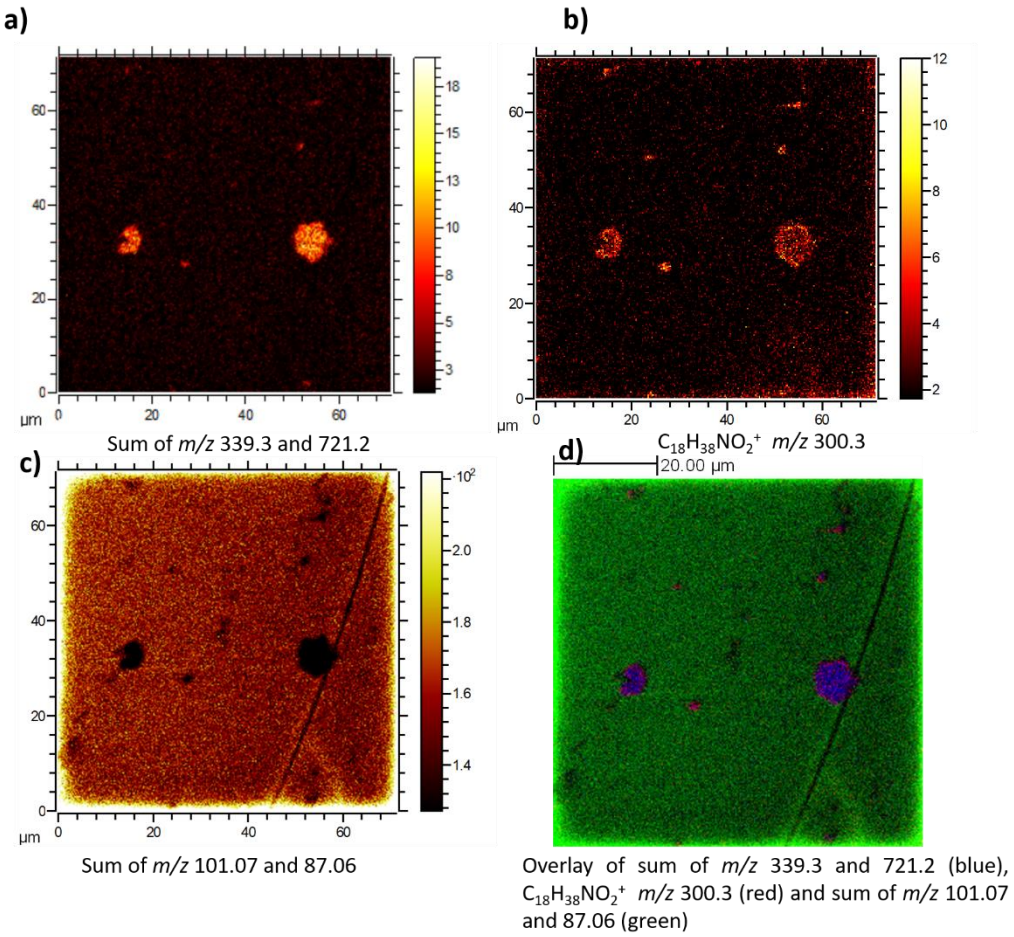


Figure 2.18: 3D BA images of **a)** Sum of *m/z* 339.3 and 721.2, **b)** $C_{18}H_{38}NO_2^+$ *m/z* 300.3, **c)** Sum of *m/z* 101.07 and 87.06, **d)** Overlay of sum of *m/z* 339.3 and 721.2 (blue), $C_{18}H_{38}NO_2^+$ *m/z* 300.3 (red) and sum of *m/z* 101.07 and 87.06 (green)

In these images, some agglomerated particles are present along with isolated single particles. Nevertheless, by plotting a 3D rendering on one of the signals of Compritol® 888 ATO (figure 2.19), the size of the particles was estimated along z axes. The value is around 2 µm, confirming the expected dimensions of the particles.

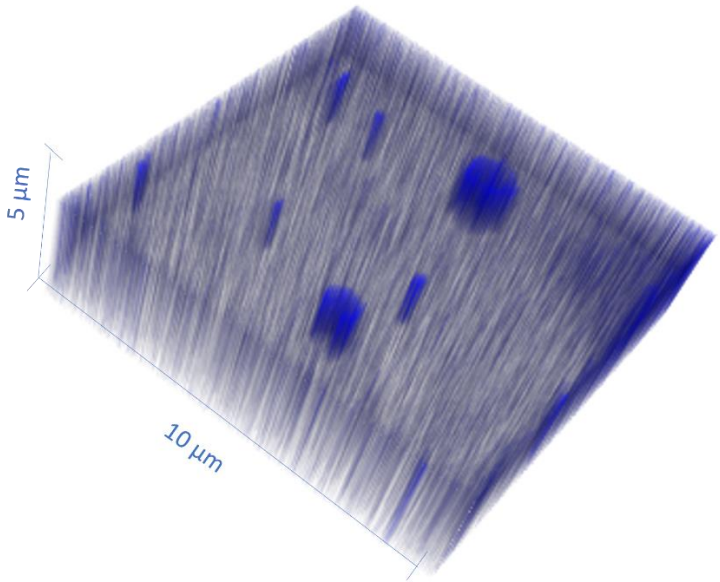


Figure 2.19: 3D rendering of *m/z* 339.3 (Compritol® 888 ATO)

## 2.6 Conclusions

The chemical three-dimensional structure of solid lipid nanoparticles assumes a critical role for the drug releasing process during the drug delivery, reflecting its effects on the patient's drug assimilation. This thesis shows that ToF-SIMS imaging is a valid tool for providing structure information about these systems. Notwithstanding, SLNs imaging with ToF-SIMS had not been realized before and despite the lack of supporting literature, it was possible to provide an efficient procedure for SLNs imaging. In fact, particles' agglomeration phenomenon did not permit analysis by dropping the particles directly on Si. However, by exploring several procedures, it was found out that solid trehalose matrix permitted both the dispersion and stabilization of the single particles and was suitable as an ultra-high vacuum solid sample. Thanks to the high sputtering yield, this matrix can be easily eroded and avoids the damage processes induced by primary ions, even without the use of giant cluster ion beams.

Another issue that was overcome was the identification of molecular signals. In fact, the chemical composition of the SLNs components is protected by an industrial patent. Therefore, it was necessary to carry out several high mass resolution analyses in order to achieve a correct peak attribution. This is essential to obtain BA images where mass resolution is very scarce.

Having resolved the main issues that prevented previous analysis, here isolated SLN particles were observed and their dimensions, even in 3D, were measured using ToF-SIMS imaging. Further, it was possible to identify the molecular peak of the anti-inflammatory loaded inside lipidic core drug. Thus,

these promising results demonstrated the development a TOF-SIMS imaging procedure for the discrimination between 1$^{st}$ and more structured 2$^{nd}$ and 3$^{rd}$ generations SLNs.

*References*


1. Üner M, Yener G. Importance of solid lipid nanoparticles (SLN) in various administration routes and future perspective. *International Journal of Nanomedicine*. 2007;2(3):289-300.

2. Bae KH, Lee JY, Lee SH, Park TG, Nam YS. Optically traceable solid lipid nanoparticles loaded with sirna and paclitaxel for synergistic chemotherapy with in situ imaging. *Advanced Healthcare Materials*. 2013;2(4):576-584. doi:10.1002/adhm.201200338

3. Dubes A, Parrot-Lopez H, Abdelwahed W, et al. Scanning electron microscopy and atomic force microscopy imaging of solid lipid nanoparticles derived from amphiphilic cyclodextrins. *European Journal of Pharmaceutics and Biopharmaceutics*. 2003;55(3):279-282. doi:10.1016/S0939-6411(03)00020-1

4. Andreozzi E, Seo JW, Ferrara K, Louie A. Novel method to label solid lipid nanoparticles with 64Cu for positron emission tomography imaging. *Bioconjugate Chemistry*. 2011;22(4):808-818. doi:10.1021/bc100478k

5. Amekyeh H, Billa N, Roberts C. Correlating gastric emptying of amphotericin B and paracetamol solid lipid nanoparticles with changes in particle surface chemistry. *International Journal of Pharmaceutics*. 2017;517(1-2):42-49. doi:10.1016/j.ijpharm.2016.12.001

6. SCHWARZ C. Solid lipid nanoparticles (SLN) for controlled drug delivery II. drug incorporation and physicochemical characterization. *Journal of Microencapsulation*. 16(2):205-213. doi:DOI: 10.1080/026520499289185

7. Rainer H. MuÈller, Karsten MaÈder SG. Solid lipid nanoparticles (SLN) for controlled drug delivery: a review of the state of the art. *European Journal of Pharmaceutics and Biopharmaceutics*. 50:161-177.

8. Amekyeh H, Billa N, Roberts C. Correlating gastric emptying of amphotericin B and paracetamol solid lipid nanoparticles with changes in particle surface chemistry. *International Journal of Pharmaceutics*. 2017;517(1-2):42-49. doi:10.1016/j.ijpharm.2016.12.001

9. Fletcher JS, Rabbani S, Henderson A, Lockyer NP, Vickerman JC. Three-dimensional mass spectral imaging of HeLa-M cells - Sample preparation, data interpretation and visualisation. *Rapid Communications in Mass Spectrometry*. 2011;25(7):925-932. doi:10.1002/rcm.4944

10. Brison J, Robinson MA, Benoit DSW, Muramoto S, Stayton PS, Castner DG. TOF-SIMS 3D imaging of native and non-native species within hela cells. *Analytical Chemistry*. 2013;85(22):10869-10877. doi:10.1021/ac402288d

11. Piehowski PD, Kurczy ME, Willingham D, et al. Freeze-etching and vapor matrix deposition for ToF-SIMS imaging of single cells. *Langmuir*. 2008;24(15):7906-7911. doi:10.1021/la800292e

12. Parry S, Winograd N. High-resolution TOF-SIMS imaging of eukaryotic cells preserved in a trehalose matrix. *Analytical Chemistry*. 2005;77(24):7950-7957. doi:10.1021/ac051263k

# 3 ToF-SIMS Detection, Identification, and Imaging of Dyes on Textiles from 19th Century and PCA Data Treatment

As stated in the introduction, ToF-SIMS is a powerful tool for the study of surfaces in materials science and has become particularly relevant for many different fields of research including cultural heritage. The first reviews of its use for the study of ancient glasses or metal artefacts already existed in the literature since 2000s. In general, these studies were limited to inorganic materials. Nevertheless, especially after the introduction of cluster beams, ToF-SIMS application spread out also in the study of organic materials from cultural heritage artefacts. This technique allows not only the identification, but also the distribution, by means of imaging, of organic components present in artworks. Thanks to its excellent lateral resolution and its minimal sample preparation, ToF-SIMS currently has become one of the primary reference techniques for chemical imaging by mass spectrometry for cultural heritage analysis. Moreover, the investigation of the materials' structures often requires the support of computer modelling and other advanced experimental methodologies. This is particularly true in the case of complex samples, such as artworks, where not all the components are entirely known and understood.

During the second year of the PhD course, I had the possibility to be hosted and work at the *Laboratoire d'Archéologie moléculaire et Structurale* (LAMS) in Paris under the supervision of Doctor Alain Brunelle, who is the Directeur de Recherche (DR1) *Centre national de la recherche scientifique* (CNRS). LAMS is a research unit associated to Sorbonne University (Campus Pierre et Marie Curie) and the CNRS since 2012, which deals with the characterization of cultural heritage objects of different origin and constitution, such as paintings, ceramics, textiles, and frescos. There I applied the ToF-SIMS technique to the identification and imaging of dyes on ancient textiles from 19th century. In particular, the analysed textiles come from a 19th century dye catalogue, which is the third tome of a French dye collection called *"Revue Générale des Matières Colorants et des Industries qui s'y rattachent"*.

The study of textile dyes is fundamental to obtain important information about the materials and the techniques involved in old dyeing processes. In particular, the characterization of the textiles from XIX century yields an understanding of how the chemistry evolved during the industrial revolution and which kinds of processes were developed. The classical characterization procedure requires a hydrolysis step, various extraction techniques, separation by a chromatographic technique, and finally the identification of the individual compounds present[1]. Nowadays, it is known that ToF-SIMS is a

promising alternative method, because it avoids the phase of extraction which can result in the possible destruction of the molecular structure of the sample.[2]

In this thesis, the results obtained for a textile taken from a 19th century French catalogue are reported. This catalogue contains 480 samples and each of them is coloured with a different dye, i.e. 480 different dyes. For this reason, an accurate selection of the samples on the catalogue was needed. A set of ten samples were selected to be analysed, two representatives of the colours red, purple/pink, orange/brown, blue and black. Because of the difficulties verifying or even obtaining the lineage of the samples, thorough results could only be provided for one of the selected. Nevertheless, the detection and identification, as well as PCA data treatment was provided for on dye used for colouring a textile named *Bleu méthylène-Imprimé avec la gomme végétale*, produced by *(B.A.S.F.)* contained in the catalogue.

The analyses of this sample have been very challenging for their interpretation as many chemical components were unknown. As said, these kinds of analyses require specific methods of post-analysis treatments, in order to provide tools for the data interpretation. Currently, the most popular approaches for handling and interpretation of ToF-SIMS data are based on multivariate analysis methods. Among these, principal component analysis (PCA) and other related techniques became a sort of standard approach in the ToF-SIMS community. In fact, PCA can extract features from a complex set of data, allowing the recognition of chemically different areas in the same sample. In this thesis work, PCA data treatment methodology was performed in a textile sample for the recognition of unidentified different chemical components.

## 3.1 Thesis work and ToF-SIMS dyes on textiles analysis issues

The aim of this project was to provide the detection, identification, and the spatial distribution of ancient dyes used for colouring several different textiles, according to the methodologies used in the 19th century. Although this purpose can seem banal, it was necessary to overcome several issues related to the antiquity of these samples. From the end of 18thcentury and during the first and second industrial revolution in the 19th century, many scientific discoveries were achieved[3]. Among these, many new molecules were synthetized, including dyes[4],and the first textile colouring techniques at an industrial level were developed[5]. Especially in France and Germany, many important industrial companies started to build their own plants and produce their own dyes. Rules and regulations were not present, thus no check or control on the possible impact of the molecules on the human health was undertaken. Likewise, no respect for the patents or the paternity of the discoveries was imposed. The industries were “let loose” to produce as many structural variations of the molecules as they

wanted, and to appropriate of the paternity of new dyes just changing their names. This out of control-behaviour of the industries has given many consequences on the catalogues from 19th century, which display long lists of dyes, creatively named, without any chemical information for scientists and historicists.

The previous studies on ToF-SIMS textiles analysis show that ToF-SIMS is an excellent technique for ancient textiles[6]. Compared to other techniques, smaller sample sizes are utilized and the solvent extraction of the dyes from the fibres is avoided. So far, the reports have been limited to the analysis of natural dyes such as curcumin, quercetin or indigo, however. For textiles originating from the 19th century, a further complication is added: the molecules used for dying these textiles have a synthetic nature. Although their core structure was often taken from natural organic groups (such as for instance Fluorone or Benzidine), these synthetic dyes are the results of several chemical processes, and their final structures are unknown. As a matter of fact, the identification of the composition for most of these dyes is very difficult and, unfortunately most of time impossible, because of several problems:

- The lack of information and literature about the samples. During the periods discussed earlier, industries used to name the new synthetic molecules with creative names and were not obliged to reveal the chemical structure or to patent their syntheses process. This entailed chaos in the chemical nomenclature of new molecules. In fact, different industries produced the same molecules, and each attributed a different name to them. Therefore, the only information for certain was the coloration. In some cases, however, the name of the dye was reminiscent of a well-known chemical structure and can provide a clue as to its nature.
- The incompatibility to the reference samples. For all the investigated samples, the results were compared with references. Nevertheless, most of the spectra were not comparable to the reference ones. These differences might be correlated to many causes. In the case of cultural heritage objects' characterization, the long passage of time must be considered since degradation phenomena can occur[7]. This group of processes ranges from the photooxidation induced by the exposition to the light, to the mechanical damage caused to the human handling. The *ageing* the textiles underwent can be also visible through the discoloration of the dyes (loss of brilliance or lowering of tonality), the creases along the textiles, and also some stains (either dark/brown or white). All of these processes have likely provoked chemical modifications of the dye molecules and therefore they cannot show the same spectra of the pristine molecules. Consequently, despite the understandable nomenclature, it was impossible to provide a robust identification for most of the samples. Additionally, the references were in the form of a salt, generally chlorides, while the interaction between the dyes and the textiles implicates either secondary bonds (Van der Waals, London, Coulomb

forces) or chemical covalent bonds. These kinds of chemical interactions can modify the electronic system of the molecules, distorting the orbitals, and thus, influence the chemical behaviour under ion bombardment of the dyes on textiles. However, the aim of this project was the identification of the dye molecules, and these chemical modification reactions and ageing phenomena will not be delved into.

- The complex matrix of the samples. Moreover, even though ToF-SIMS is a powerful instrument to analyse hybrid solid sample, these textiles represent a very complex matrix since they were woven with thin and hairy fibres, which can cause charging phenomena. Indeed, many textile typologies easily undergo charging phenomena, because of the presence of a high thickness of hair, which can increase the surface charge.

Despite all the issues which affected the analysis of these samples, this thesis work presents the ToF-SIMS analyses for *Bleu méthylène-Imprimé avec la gomme végétale*, produced by *(B.A.S.F.)* from the 19$^{th}$ century catalogue. Thanks to the PCA treatment of the acquired data the ancient dyeing technique used for colouring this textile was identified together with other components in the textile.

## 3.2 Materials and Methods

The ancient catalogue, including the samples, belongs to a private collection. It contains 480 pieces of textiles of different composition, such as wool, silk, linen, and cotton (of course just natural textiles, since at that time the synthetic fibres were not developed yet). Among these samples, some textiles show a unique and homogeneous coloration, others show several decorations, either geometrical or with flowers and plants drawing, of different colours.


Figure 3.1: sample picture of Bleu méthylène-Imprimé avec la gomme végétale, produced by (B.A.S.F.)

The results are reported for the sample *Bleu méthylène-Imprimé avec la gomme végétale* : page *N°33, échantillon N° 82*. The sample (figure 3.1) shows blue flower decorations (supposed to be realized with *Bleu méthylène*) on a white background which is probably the textile treated for the colouring process.

As far as the textile sample preparation is concerned, an appropriate protocol was employed to make the samples compatible with high voltage and ultra-high vacuum and to avoid surface charging. A minimal number of filaments were extracted from the samples on the lateral side using tweezers. Then, the filaments were glue on a conductive substrate, by means of a conductive double-sided tape. Successively, they were wet with some drops of distillate water and left inside a press for about one hour. This process would decrease the thickness of the hair and mitigate the charging phenomena, which could had compromised the analysis. Lastly, they were dehydrated in a desiccator overnight. Figure 3.2 show the comparison between the fibres before and after the procedure.

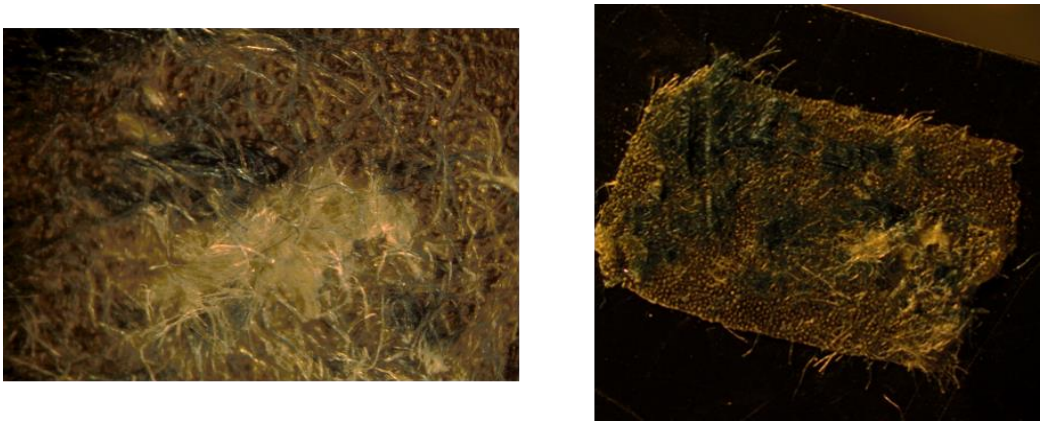

Figure 3.2: pictures of (left) Filament of Bleu méthylène-Imprimé avec la gomme végétale before pressing, (right) after pressing

To compare the sample spectra to a reference, Methylene Blue was purchased from Sigma Aldrich (CAS Number 28983-56-4, $C_{16}H_{18}N_3S^+Cl^-$ 319.09 amu, $C_{16}H_{18}N_3S^+$ [$M^+$] 284.12 amu). For predisposing the reference to the ToF-SIMS analysis, an ethanol : MilliQ Water (3:1) solution was prepared. Some drops of the solution were placed on a silicon wafer. Then, the solvent was evaporated overnight.

The ToF-SIMS analyses were carried out by a TOFSIMS IV spectrometer with delayed extraction (IONTOF, Germany), equipped with a LMIG Bismuth source and an Argon cluster beam source (GCIB). The HCBU mode was used for the analyses of both the sample and the reference. For these analyses, a 25 keV $Bi_3^+$ ion beam was selected with an incidence angle of 45°. This ion source operating mode ensures a high mass resolution ($M/\Delta M=6\times10^3$). The primary ion dose density was

$4.37\times10^{11}$ ions per $cm^2$, below the so-called 'static SIMS limit', in order to preserve the molecular information. The $Bi_3^+$(100µs) current was measured 0.48 pA on the Faraday cup. A low energy electron flood gun was activated to neutralize any residual charge on the surface of the samples. Secondary ion images were also acquired in HCBU mode over a sample surface of 200 µm × 200 µm. The mass resolution was 7000 M/ΔM measured at mass 29. In order to manage the amount of data and make it possible the interpretation of the results, a Principal Component Analysis (PCA) was carried out.

## *3.3* Results and Discussions

### 3.3.1 Preliminary analyses

First ToF-SIMS analyses of the reference Methylene Blue were carried out. The positive spectrum (Figure 3.3) reveals the molecular peak at 284.1257 (zoomed in the insert) with the associated isotope cluster distribution, which is reported in Table 3.1.

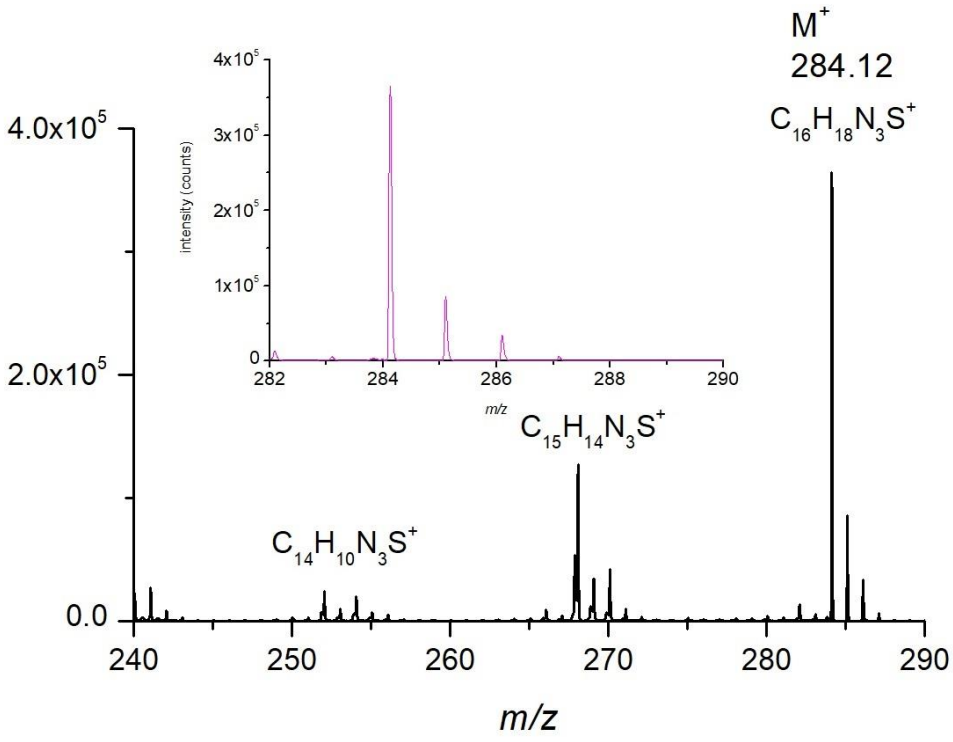


Figure 3.3: reference positive ion mass spectrum

Table 3.1: cluster isotopic calculation of $C_{16}H_{18}N_3S^+$

| Peaks | Theoretical *m/z* | Measured *m/z* | Dev. (ppm) | Relative Abundance |
|---|---|---|---|---|
| $C_{16}H_{18}N_3S^+$ | 284.1221 | 284.1206 | -5.28 | 78.88 |

| | | | | |
|---|---|---|---|---|
| $C_{15}{}^{13}C_1H_{18}N_3S^+$ | 285.1255 | 285.1013 | -84.87 | 13.65 |
| $C_{16}H_{18}N_3{}^{34}S^+$ | 286.1179 | 286.0994 | -64.7 | 3.56 |
| $C_{14}{}^{13}C_2H_{18}N_3S^+$ | 286.1289 | 286.0994 | -103.1 | 1.11 |
| $C_{16}H_{18}{}^{15}NN_2{}^{34}S^+$ | 285.1192 | 285.0975 | -76.1 | 0.87 |
| $C_{16}H_{18}N_3{}^{33}S^+$ | 285.1215 | 285.0947 | -94.00 | 0.63 |

As well as the molecular peak, a series of patterns of the fragments related to the loss of 14 and 16 amu were identified. They probably derive from fragmentation processes which provoke the loss of one $CH_2$ group and $H_2$ (284-14amu = 270, -2 amu, *m/z* 268), followed by another loss of $CH_2$ and $H_2$ (-14 amu, *m/z* 254, -2 amu, *m/z* 252). The $C_{15}H_{14}N_3S^+$ peak at m/z 268.0848 and $C_{14}H_{10}N_3S^+$ peak at m/z 252.0489 were also found in the reference positive spectrum, presumably originated from the same fragmentation process.

Then, sample spectra and reference spectra were compared in figure 3.4. It is evident from figure 3.4 that the dye on the textile underwent a different fragmentation process. As a matter of fact, the sample positive spectrum shows peaks related to the loss of methylene groups ($-CH_2$) but not methylene plus $H_2$. Within the literature, this behaviour has also been confirmed[8], and has been described as a photodegradation process. The peaks within that study closely correspond to those reported for the dye on textile sample. Considering the age of this sample it is quite possible that photodegradation occurred and strong peaks were observed for the $CH_2$ degradation pathway. In contrast, in the reference spectrum, the molecular peak is the most intense. Therefore, it is reasonable affirm that the other peaks in the reference originated only by fragmentation and no degradation occurred.

One of the interesting peaks observed in the spectra acquired from the sample is at *m/z* 270. In the literature this has been identified as Azure B $C_{15}H_{16}ClN_3S$. The chemical structure of Azure B is reported in figure 3.5. Azure B is an active metabolite of methylene blue and nowadays it is used as histological dye, a fluorochrome, and a drug metabolite. Moreover, it can be used as dye itself. Previous study of the photodegradation process in Methylene Blue also identified this peak as Azure B. The positive spectrum of the *Bleu méthylène-Imprimé avec la gomme végétale* on textile (figure 3.4, bottom) shows the molecular peak $[M]^+$ of the Azure B with the related cluster isotope distribution, reported in the table 3.2. The strong intensity of this peak confirms the presence of this molecule on the textile.

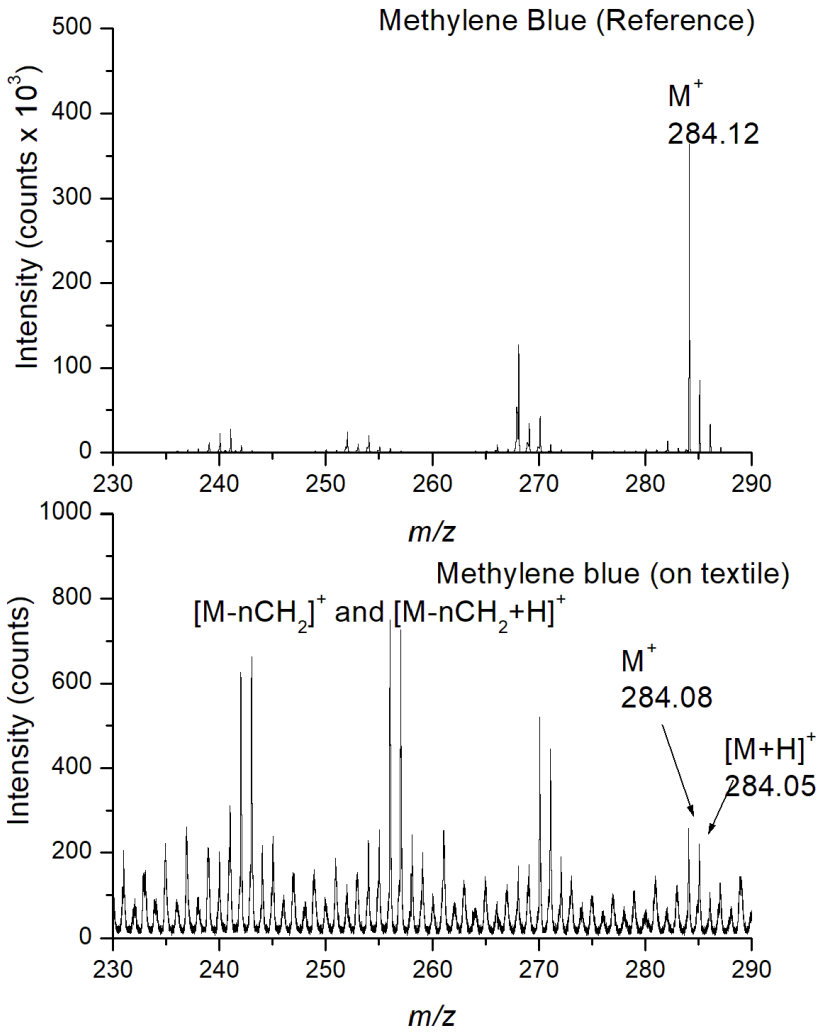


Figure 3.4: comparison between the reference spectrum (top, previously shown in the figure 3.15) and the textile spectrum (bottom)

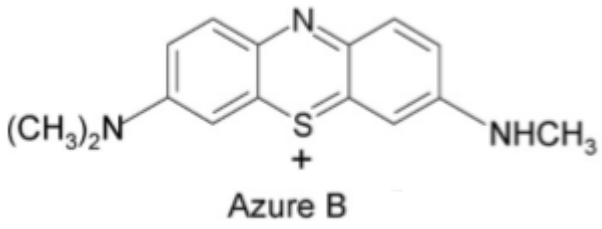


Figure 3.5: Structure of Azure B molecule

Table 3.2: cluster isotopic calculation of $C_{15}H_{16}N_3S^+$

| **Peaks** | **Theoretical *m/z*** | **Detected *m/z*** | **Dev. (ppm)** |
|---|---|---|---|
| $C_{15}H_{16}N_3S^+$ | 270.1059 | 270.0486 | -212.13 |

| | | | |
|---|---|---|---|
| $C_{14}{}^{13}CH_{16}N_3S^+$ | 271.1093 | 271.0550 | -200.29 |
| $C_{15}H_{16}N_3{}^{34}S^+$ | 272.1017 | 272.0560 | -167.95 |

The presence of Azure B can have two possible origins. The first, as supported in the literature, is that methylene blue degradation gives rise to the Azure B molecule. Thus, considering the age of the sample, significant degradation may have occurred, leading to the stronger intensity of Azure B vs. Methylene Blue molecular peak. The other possibility is the use of Azure B within the original dye itself. Historically, this molecule was used as a blue dye. Considering the lack of control in the textile dyeing industrial processes in the past, it may be possible that the Methylene Blue colour was mixed with other blue dyes such as Azure B. This could also justify such intense Azure B molecular peak in the spectrum of the sample. Another possibly is a combination of the two cases. Further investigations of historical documentations are needed to determine the origin of this dyeing procedure.

ToF-SIMS analyses rise important questions about this textile, whether the dye was pure initially and simply photodegraded, or it was mixed purposely with other dyes. ToF-SIMS therefore can represent a tool to answer to questions on ancient textiles' analyses. For the purpose of further investigations, the secondary ion images were acquired and will be discussed in the next section.

### 3.3.2 Secondary ion imaging and PCA data treatment

As stated in the introduction PCA is a powerful tool for the processing of large and/or complex data sets and is recently becoming popular within the ToF-SIMS community. Nowadays it is also included in the vendors software dedicated to ToF-SIMS instruments. In this study, the preliminary analyses have shown the presence of chemically different areas in the sample besides the areas coloured with Methylene Blue. In the light of these results, a further investigation about the surrounding matrix was carried out. To highlight the presence of other components, a multivariate analysis (PCA) was fulfilled by using SurfaceLab 7 PCA by IONTOF. From the study of the original total area spectrum, every single peak was manually integrated to be evaluated by PCA. Several principal components were obtained and, among these, PC1, PC2 and PC3 were evaluated to study the different chemical components of the sample.

Figure 3.6 shows PC1 image (left) and total ion count (TIC) image (right). PC1 explains the maximum variability of the data, that in the case of ToF-SIMS imaging is given by the discrimination between the pixels which contains any peaks' intensity and pixels with zero counts for the entire mass spectra. Thus, PC1 is always comparable to TIC in ToF-SIMS imaging and Figure 3.6 confirms PCA is

operating correctly. In Figure 3.7 PC1 loadings are not able to discriminate any difference between the peaks, since as said PC1 identifies just the peaks with intensity more than zero. In contrast, if a difference was observed, PCs would plot negative features on the y-axes of the loading graph. Indeed, in general, loadings define the relationship between the new PCs and the original spectral coordinates (peaks). Because no discrimination was observed in the loading graph, the chromatic variation in the PC1 image is probably associable to the topography trend.

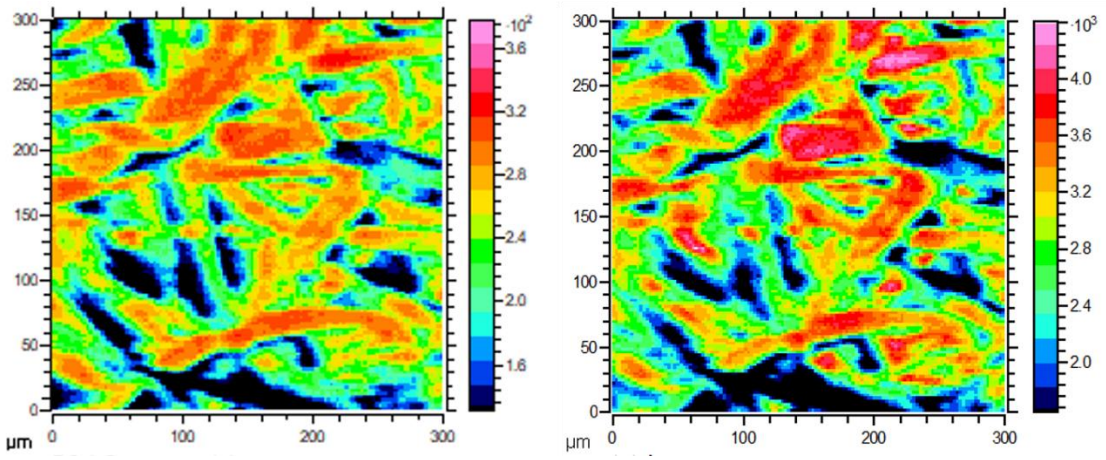


Figure 3.6: Image of Principal Component 1 (PC1, left) and of total ion count (right)

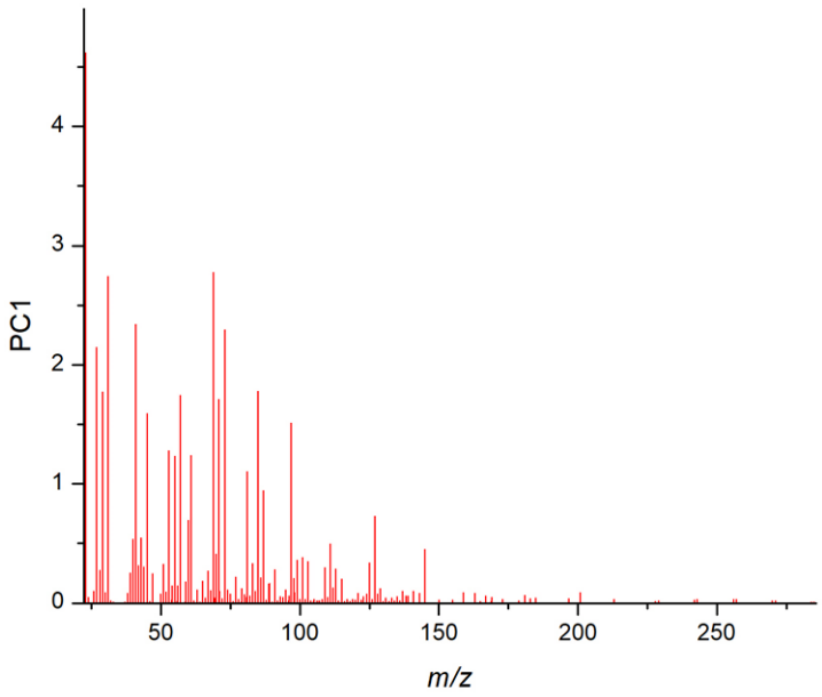


Figure 3.7: PC1 loading

Figure 3.8 shows PC2 representation, where it is evident a non-homogeneous distribution of the variables. In comparison to PC1, which looks at the greatest variability in the spectra i.e. counts vs. no-counts, PC2 searches for groups of peaks which are clustered in certain pixels of the image. As it is clear in figure 3.8, coloured pixels represent the area of the sample characterized by these groups of peaks. In contrast the black coloured pixels represent areas of the sample where these peaks have no counts.

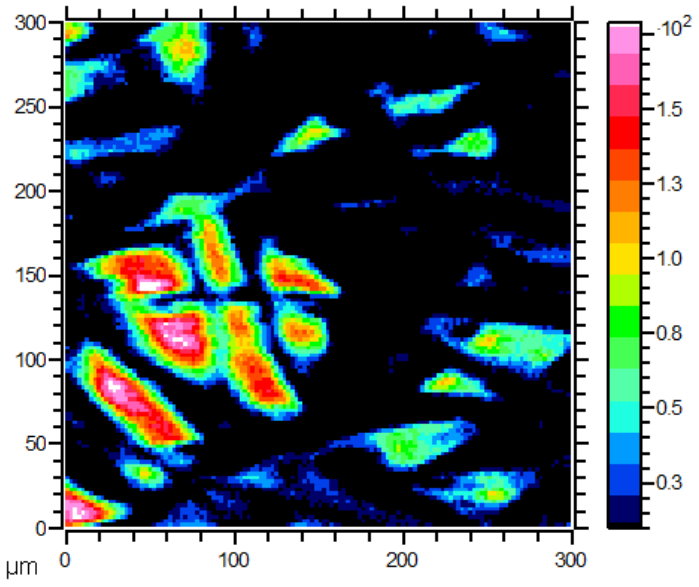


Figure 3.8: PC2 representation

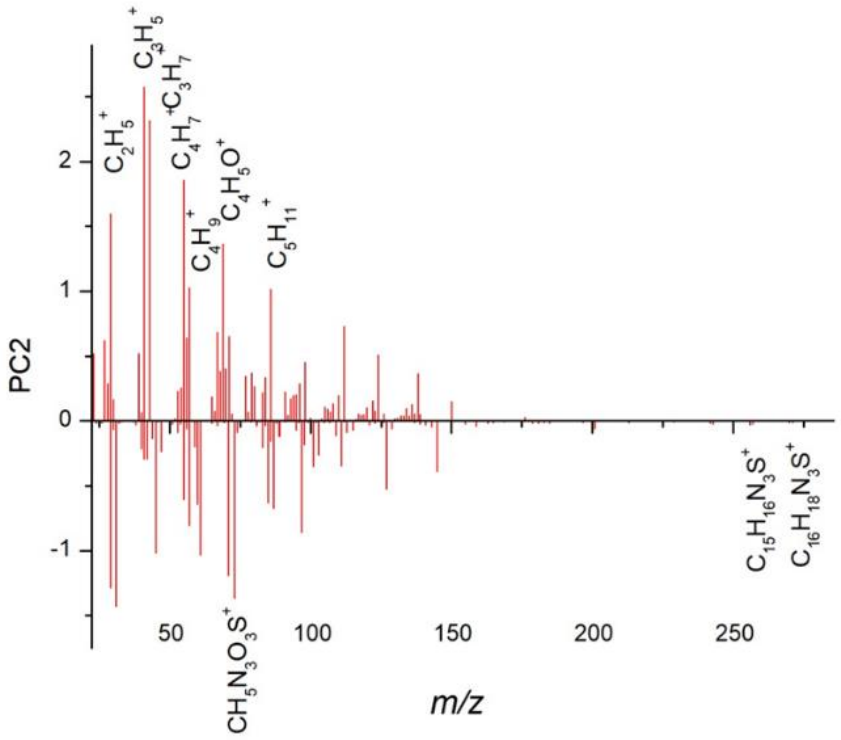


Figure 3.9: PC2 loadings

By studying the loadings (figure 3.9), it is evident that PC2 can discriminate between two different types of variables. In particular, the positive variables in the loadings are those visible in the PC2 image. In this case, the negative loadings correspond to the dark areas. In the positive side of PC2 loadings, several *m/z* values assignable with reasonable certainty to hydrocarbon fragments ($C_nH_m$, aliphatic-like) were found. Among the negative variables, the dye characteristic peaks ($C_{16}H_{18}N_3S^+$ and $C_{15}H_{16}N_3S^+$) were found. This indicates in the PC2 image certain regions do not contain the dye. Considering Figure 3.2 which shows the original sample, it is clear that the blue dye is not present over the entire textile and certain areas are white. PC2 highlighted this feature.

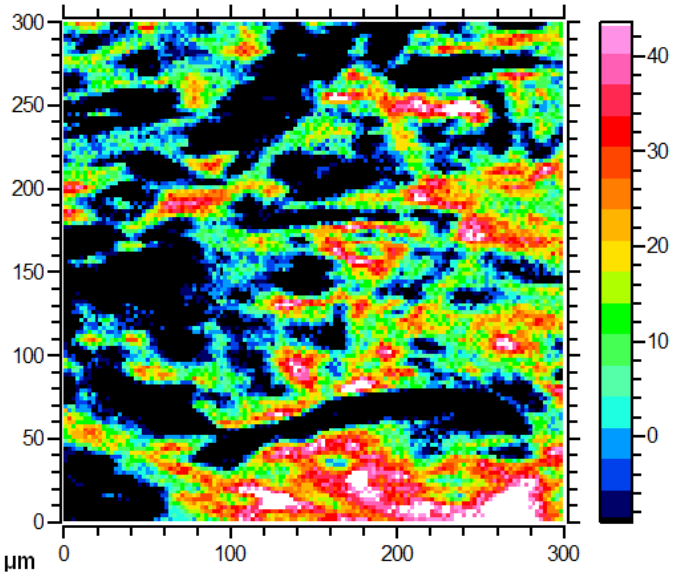


Figure 3.10: PC3 representation

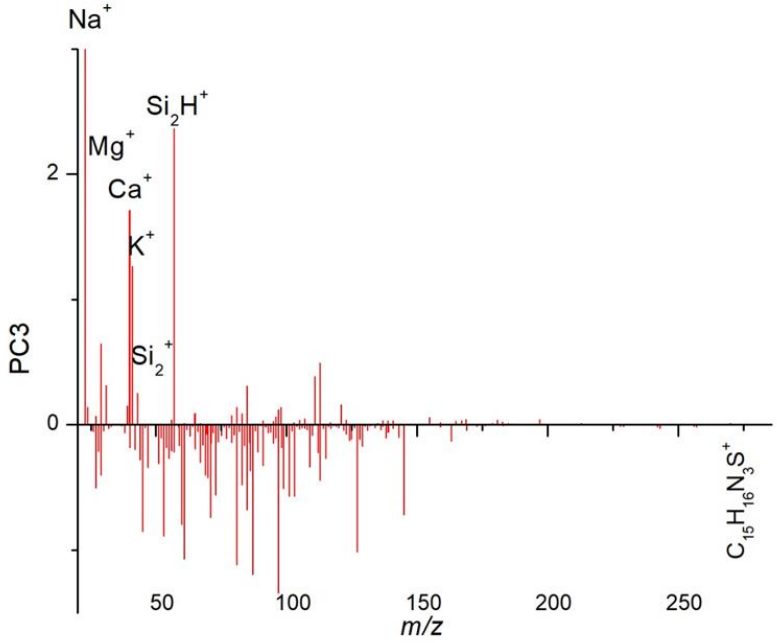


Figure 3.11: PC3 loading

As well as PC2, PC3 image in figure 3.10 shows a different clustering of certain peaks. The PC3 loadings (Figure 3.11) reveal a discrimination between positive and negative variables. In this case, the positive variables are represented by inorganic cluster and metal ions. On the other hand, the negative variables include organic fragments including the dye characteristic ones. Thus, PC3 is discriminating the regions of organic species from the regions characterized by inorganic ion peaks. Both PC2 and PC3 were able to highlight regions with different chemical composition which do not include the dye. PC2 revealed hydrocarbon fragments in the positive side of the loadings and PC3 showed inorganic peaks for the positive side of the loadings. Therefore, PC2 and PC3 made it evident that certain regions of textile were not coloured by the dye. To confirm PCA findings, the peaks identified in Figure 3.9 and 3.11 were summed and plotted. In particular, Figure 3.12 shows the sum of the signals $C_2H_5^+$, $C_4H_8^+$, $C_5H_8^+$, $C_5H_{11}^+$, $C_6H_{14}^+$, $C_7H_{12}^+$, $C_8H_{10}^+$ from PC2 positive loadings. This chemical map presents the same spatial distribution of PC2 image (Figure 3.8). The *m/z* values of these peaks are shown in table 3.3 with the relative deviation values. Figure 3.13 displays the chemical maps of the sum of $Al^+$, $Ti^+$, $Ca^+$, $CaH^+$, $Mg^+$, $CaH^+$, $Si_2^+$, $Si_2H^+$ signals from PC3 positive loadings, which looks very similar to PC3 image (figure 3.10). The *m/z* values of these peaks are shown in table 3.4 with the relative deviation values.

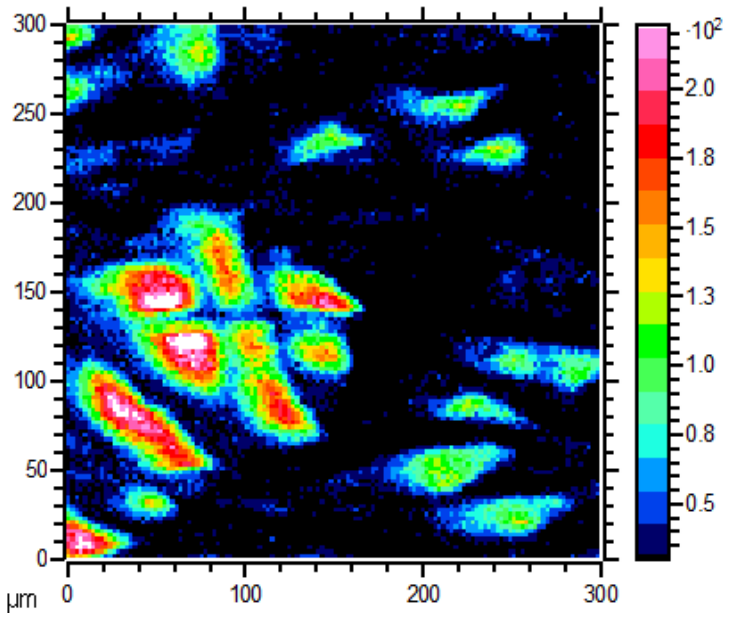


Figure 3.12: Image of the sum of $C_5H_{11}^+$, $C_6H_{14}^+$, $C_7H_{12}^+$, $C_2H_5^+$, $C_4H_8^+$, $C_5H_8^+$, $C_8H_{10}^+$ ions

Table 3.3: PC2 peak assignment

| **Signals** | **Theoretical *m/z*** | **Measured *m/z*** | **Deviation (ppm)** |
|---|---|---|---|
| $C_2H_5^+$ | 29.0386 | 29.0428 | 144.64 |

| | | | |
|---|---|---|---|
| $C_4H_8^+$ | 56.0621 | 56.0591 | -53.51 |
| $C_5H_8^+$ | 68.0621 | 68.0574 | -69.05 |
| $C_5H_{11}^+$ | 71.0855 | 71.0932 | 108.32 |
| $C_6H_{14}^+$ | 86.1090 | 86.0962 | -148.65 |
| $C_7H_{12}^+$ | 96.0934 | 96.1015 | 84.3 |
| $C_8H_{10}^+$ | 106.0777 | 106.0653 | 106.9 |

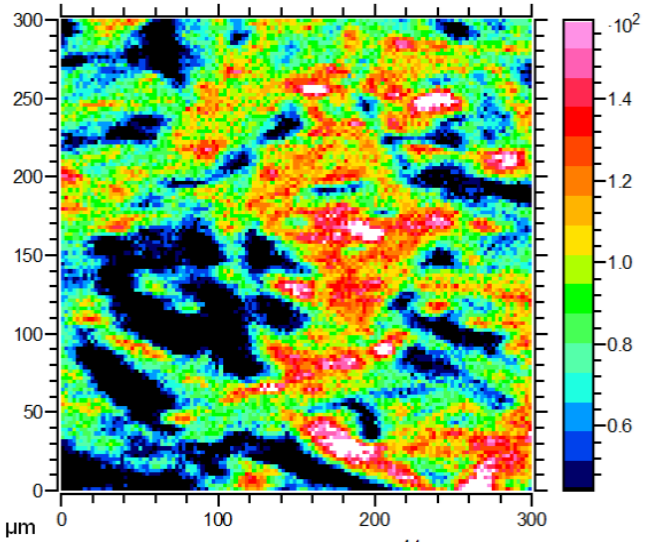


Figure 3.13: image of the sum of image of the sum of $Al^+$, $Ti^+$, $Ca^+$, $CaH^+$, $Mg^+$, $CaH^+$, $Si_2^+$, $Si_2H^+$ signals

Table 3.4: PC3 peak assignment

| **Signals** | **Theoretical *m/z*** | **Measured *m/z*** | **Deviation (ppm)** |
|---|---|---|---|
| $Mg^+$ | 23.9845 | 23.9429 | -173.4 |
| $Al^+$ | 26.9810 | 26.9759 | -189.0 |
| $Ca^+$ | 39.9620 | 39.9586 | -85.1 |
| $CaH^+$ | 40.9699 | 40.9655 | -107.4 |
| $Si_2^+$ | 55.9533 | 55.9459 | -132.25 |
| $Si_2H^+$ | 56.9611 | 56.9588 | -41.4 |

The results from these two figures confirmed the PCA findings which are summarized in Figure 3.14

- (red) the sum of $C_{16}H_{18}N_3S^+$ and $C_{15}H_{16}N_3S^+$ signals, characteristic of the dye.
- (green) the sum of $C_5H_{11}^+$, $C_6H_{14}^+$, $C_7H_{12}^+$, $C_2H_5^+$, $C_4H_8^+$, $C_5H_8^+$, $C_8H_{10}^+$ signals
- (blue) the sum of $Al^+$, $Ti^+$, $Ca^+$, $CaH^+$, $Mg^+$, $CaH^+$, $Si_2^+$, $SiH^+$ signals

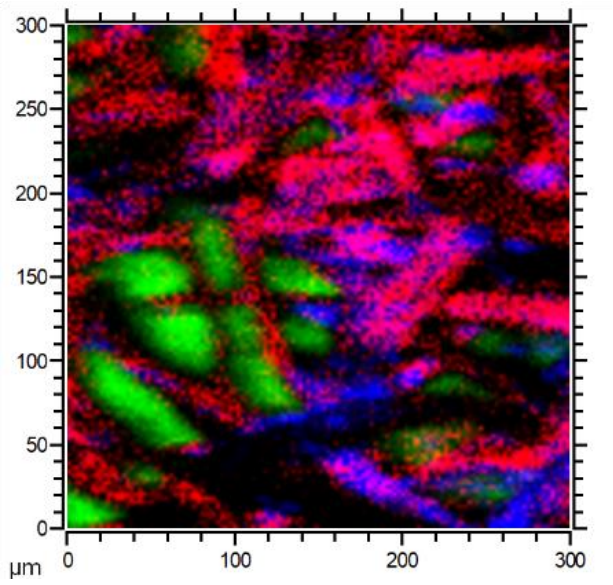


Figure 3.14: 3-color overlay showing the distribution of the sum of $C_{16}H_{18}N_3S^+$ and $C_{15}H_{16}N_3S^+$ ions, characteristic of the dye (red), the distribution of sum of $C_5H_{11}^+$, $C_6H_{14}^+$, $C_7H_{12}^+$, $C_2H_5^+$, $C_4H_8^+$, $C_5H_8^+$, $C_8H_{10}^+$ ions (green), and distribution of the sum of $Al^+$, $Ti^+$, $Ca^+$, $Mg^+$, $CaH^+$, $Si_2^+$, $SiH^+$ ions (blue)

In order to ensure the assignment of the principal components and confirm the chemical distribution of the species in the sample, three ROIs were extracted from the original spectrum (Figure 3.14): from the red areas ROI 1, from the green areas ROI 2 and from the blue areas ROI 3, showed in Figure 3.15.

ROI 1 shows the peaks of the Methylene Blue dye. ROI 2 reveals some aliphatic fragments, found also in PC2 positive loadings. These aliphatic fragments probably come from the textile which was treated with a natural gum in order to prevent the colouration process in certain areas of the textile. Among the colouring technique employed in the 19$^{th}$ century industries, a technique called Batik makes use of natural gums. Indeed, it is well known from the literature that the Batik colouring technique[9,10] was already employed since ancient times in the Indian and Japanese civilizations for dying a tissue only in some specific areas. This technique spread throughout Europe in the beginning of the 19$^{th}$ century and it was performed by covering certain regions of the textiles, which were not supposed to be coloured, with waxes or vegetal paste made of gums or hydroxyicolloidal phytopolymers. The Batik procedure is generally carried out on soft textiles with thin fibres woven in a regular and flat weft, which allows a precise drawing realization. The most commonly chosen textiles are silk, cotton, and linen. The materials used to cover the textiles are named "waterproofing" and they can be either paraffin-based or polysaccharide-based[11]. In this particular case, it was used a pure vegetal gum. Historically, the use of the gums spread in Europe only from the beginning of 19$^{th}$ century thanks to the Montgolfier brothers which discovered how to waterproof textiles with gums. Finally, ROI 3 reveals inorganic fragments which are likely related to the conductive tape used to glue the textile.

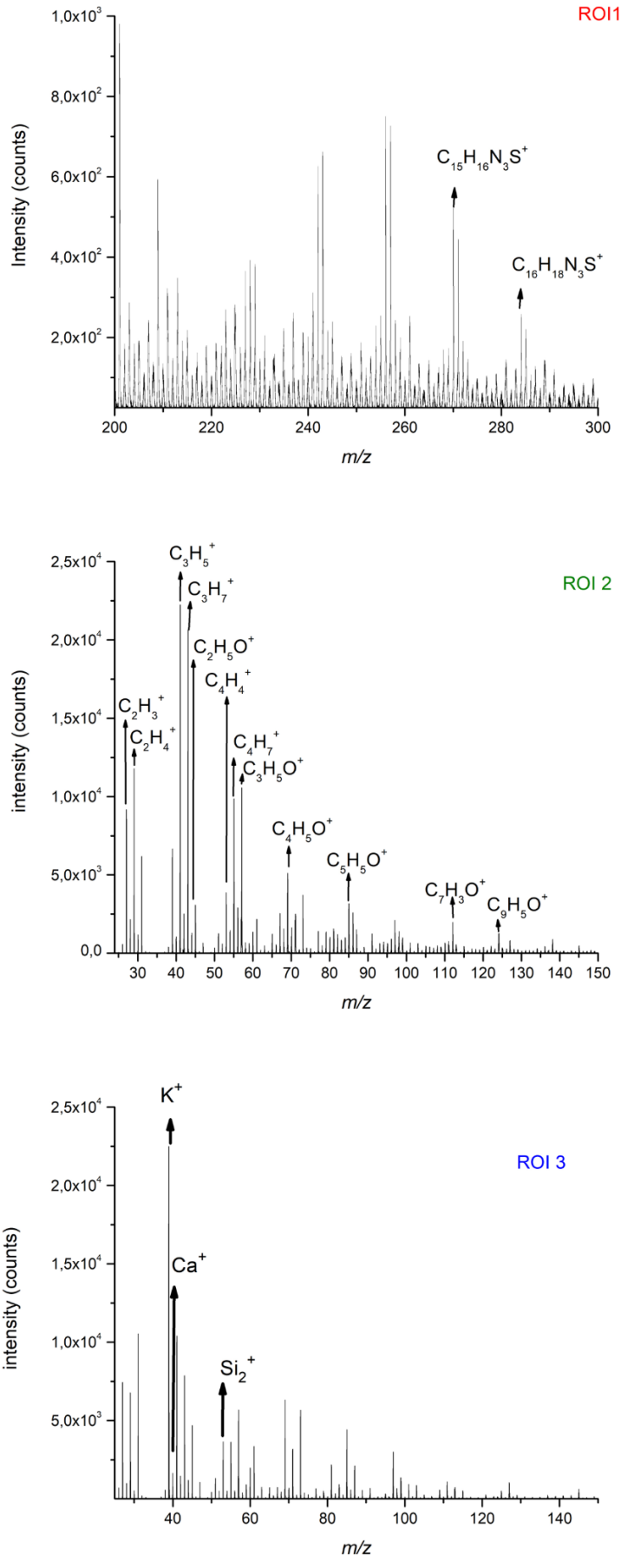


Figure 3.15: ROIs extracted from the original positive spectrum

Overall, the PCA analysis revealed a hidden characteristic of the dye textile sample. In fact, it could bring to the light the presence of areas with a different superficial chemical composition, associated with the use of different materials. Only the PCA was able to discriminate these localized regions where the dye was not present and, in this way, it was also possible to identify an 19$^{th}$ century colouring technique which was used to obtain decoration on the ancient textiles. This result demonstrates the usefulness of ToF-SIMS application to Cultural Heritage study, in particular for ancient textiles. Moreover, with the support of PCA data analysis, it can represent a powerful tool to discovered ancient procedure in the colouring techniques of textiles.

## 3.4 Conclusions

This chapter showed that ToF-SIMS can be a powerful technique for cultural heritage ancient objects. Not only did it allow us to identify molecules, but it allowed the preservation of the samples by avoiding the use of chemical products and scratching or cutting them. Only a tiny filament taken from the corner of the textile was necessary for the analysis.

In particular, for a 19$^{th}$ century textile coloured with *Bleu méthylène-Imprimé avec la gomme végétale*, the ancient dye was identified as Methylene Blue. Additionally, a post-analysis data treatment was carried out by means of Principal Component Analysis method. This analysis allowed to identify the other unknown components found in the sample and to discover the ancient colouring technique employed for this textile.

The results presented in this thesis demonstrate that ToF-SIMS can be a valid means of investigating for ancient textile, and it can represent a great source of information for ancient art objects. As future prospective, other further investigations should be conducted since it was not possible to provide a robust identification for most of the textile samples contained in the catalogue. Further research must be carried out in order to identify ancient synthetic molecules and then succeed in their recognition. However, ToF-SIMS 3D imaging could represent a valid strategy for the investigation of dyes' distribution along the depth. Discovering the spatial position of the dye molecules is important to determine which areas of the textile are more damaged, and how deep inside the dye molecules have penetrated the textile fibres. This could provide more information about the chemical nature of the bond between the dye and the textile. Moreover, the results presented in this thesis demonstrate that ToF-SIMS can be a valid means of investigating ageing phenomena, for instance comparing sample spectra to virgin textiles. Obtaining information about ageing processes would be very useful for restorers and the art conservators. Finally, it would be important to spend further time searching in literature sources (history books, revolution industrial period essays, and textile papers) for clues as to the molecular structures of ancient synthetic dyes.

*References*


1. Pirok BWJ, den Uijl MJ, Moro G, et al. Characterization of Dye Extracts from Historical Cultural-Heritage Objects Using State-of-the-Art Comprehensive Two-Dimensional Liquid Chromatography and Mass Spectrometry with Active Modulation and Optimized Shifting Gradients. *Analytical Chemistry*. Published online 2019. doi:10.1021/acs.analchem.8b05469
2. Ferreira ESB, Heeren RMA, van den Berg KJ, Maines C, Sutherland K, Higgitt C. Mass Spectrometry of Art and Cultural Heritage. *International Journal of Mass Spectrometry*. 2009;284(1-3):1. doi:10.1016/j.ijms.2009.04.006
3. Adèle Coulin Weibel. *Two Thousand Years of Textiles: The Figured Textiles of Europe and Near East.* Hacker art books; 2017.
4. Johann Peter Murmann. Knowledge and Competitive Advantage in the Synthetic Dye Industry, 1850—1914: The Coevolution of Firms, Technology, and National Institutions in Great Britain, Germany, and the United States. *Enterprise & Society*. 2000;1(4):699-704.
5. H. P. Bauman JMF. *Textile Dyeing*. E.I. du Pont de Nemours & Company
6. Lee J, Kim MH, Lee KB, van Elslande E, Walter P, Lee Y. Analysis of natural dyes in archeological textiles using TOF-SIMS and other analytical techniques. *Surface and Interface Analysis*. 2014;46(S1):312-316. doi:10.1002/sia.5594
7. Howell D, Mitchell R, Carr CM. Surface chemical investigation into the cleaning procedures of historic tapestry materials. Part 2. *Journal of Materials Science*. 2007;42(14):5452-5457. doi:10.1007/s10853-006-0779-z
8. Rauf MA, Meetani MA, Khaleel A, Ahmed A. Photocatalytic degradation of Methylene Blue using a mixed catalyst and product analysis by LC/MS. *Chemical Engineering Journal*. 2010;157(2-3):373-378. doi:10.1016/j.cej.2009.11.017
9. Belfer N. *Batik and Tie Dye Techniques*. third. Dover Publications
10. *Tie and Dye Bleach and Dye Batik Screen Printing and Painting.* Unesco Harare; 2005.
11. Azadeh Nilghaz, Dedy H. B. Wicaksono, Dwi Gustiono, Fadzilah Adibah Abdul Majid, Eko Supriyanto and MRAK. Flexible microfluidic cloth-based analytical devices using a low-cost wax patterning technique. *Lab Chip*. 2012;12(1):209-218. DOI: 10.1039/C1LC20764D

# 4. ToF-SIMS imaging of PET-PC blends

The research on polymeric blends has been extensively developed in the past decades. Indeed, polymer blends have always been considered to be interesting combinations to obtain new high-performance polymeric materials without synthesizing completely new polymers[1]. This is especially true when the properties of two or more polymers are synergistically combined.

Mixing two or more polymers is a useful methodology for the development of new materials in which the physical-chemical properties of the starting polymers are combined to achieve new blends[2]. This strategy is often more convenient and faster that studying new monomers with new synthesis techniques, which are the fundamental to the production of new polymers. Another advantage of the polymer blends is the possibility to control the final properties of the obtained material by varying the composition of the mixing. Currently, polymer-blend-based materials are very widespread and occupy a waste area of the market of many fields such as the automotive and building industry, electric and electronic or packing.

However, blending is not always simple. Sometimes polymers are not entirely miscible, and they tend to form two or more separate phases[3]. In order to obtain a unique phase, it is necessary that the mixing free energy $\Delta G_{mix}$ (equation 4.1) has a negative value[4].

$$\Delta G_{mix} = \Delta H_{mix} - T\Delta S_{mix}$$

Equation 4.1

When two polymers with a high mass weight are mixed, it is generally possible to neglect the $\Delta S_{mix}$ contribution since they have very few degrees of freedom. Therefore, the $\Delta G_{mix}$ is influenced principally by the $\Delta H_{mix}$ contribution. According to the thermodynamic law shown in Equation , it is necessary that the process is exothermic ($\Delta H_{mix} < 0$), or rather, specific interactions between the components have to occur. In most cases, the interactions belong to the Van der Waals type and the complete mixing of different polymers is rare.

Three types of polymer blends can be distinguished:

- Blends showing complete miscibility, characterized by a homogeneous structure (at least on nanometric scale); this kind of blend has one transition temperature ($T_g$) between those of the starting polymers.
- Blends showing partial miscibility; in these cases, a little amount of one component is dissolved in the other, revealing a morphology with small domains and interfacial regions

where the polymers are chemically bonded; each of the components is homogeneous and has its own $T_g$. The new $T_g$ value is shifted towards one of the other.

- Blends showing total immiscibility (most frequent), characterized from a structure with domains and prominent interfaces. The adhesion between the domains is poor and each component retains its own $T_g$.

The most interesting typology are the polymer blends belonging to the 3rd type, since they are generally characterized by a total immiscibility and, therefore, show a complex morphology with different domains of both homopolymers. The complexity of the morphology of these blends depends on the polymers' features and on the method of preparation. The result is less predictable especially when the polymer mixture is confined into thin films.

Since in thin films the ratio between surface and volume is high, surface effects can occur. Consequently, the separation phase of thin films can be considerably different from the morphology of thick films (which show a more-like bulk behaviour) despite using the same concentrations and conditions for the preparation. In some cases, it is possible to notice the inhibition of the separation, probably due to entropy factors.

Generally, polymer blends are synthetized by melt mixing procedure, which consists in mixing together the polymers in melting physic state, in an appropriate mixer. However, more interesting results can be achieved by using the spin-coating technique for the deposition of thin films. As a matter of fact, in the spin-coating technique, the solution is poured on a rotating plate which produces a quick decrease of the mobility of the molecules. This "freezes" the solution with a separation of the phases corresponding to a non-equilibrium state.

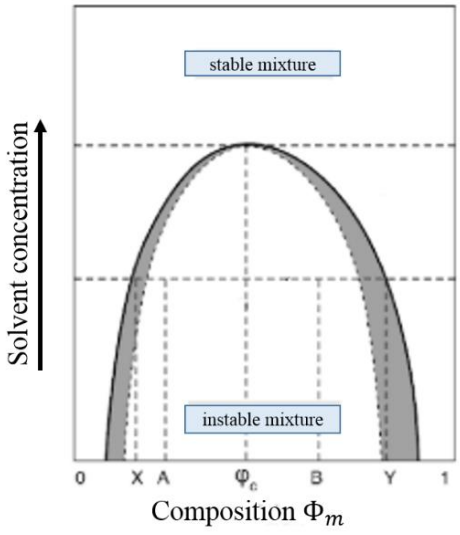


Figure 4.1: graph showing the miscibility curve of a binary polymer mixture (composition of the mixture $\Phi_m$ ) in the function of solvent concentration.

Theoretical studies show that the final phase of a binary polymeric system is influenced also by the solvent evaporation rate. Figure 4.1 shows, the mixture of two homopolymers A and B is stable in the case of high solvent concentration or low concentration of one of the two homopolymers. For low solvent concentration or high concentration of the two homopolymers, the mixture is instable, and the polymers are completely separated. Therefore, it is possible to affirm that inside the "bell of immiscibility" the mixture will be always instable, while outside the mixture will be stable.

If the solvent concentration decreases quickly, for a certain composition of the solution $\Phi_c$ (*critical composition*), the mixture becomes unstable from the equilibrium and collapses in the grey *metastable zone*. In that zone, the mixture is in a *non-equilibrium* thermodynamic condition and the blend morphology is characterized by alternated homopolymer domains of small dimensions. Many types of morphology can be obtained through this procedure for immiscible polymers. Overall, one of the challenges in studying immiscible polymer blends is the use of appropriate characterization techniques. For these reasons, providing a strategy for their characterization can give a great contribution for the enhancement of the materials design of new polymer blends.

## 4.1. PET-PC Blend

Polycarbonate (PC) and poly (ethylene terephthalate) (PET) have been identified in the past as technical polymers due to their high level of properties. However, their commercial importance has brought their application in the field of commodity polymers and, for this reason, these polymers are widely spread in the industry of the plastic matter. This widespread use also comes with several consequences, first of all the increasing volume of polymer wastes (especially PET) due to their use in the packaging industry.

As stated before, polymeric blends have been extensively investigated in the twenty past years. In fact, blending can give origin to new high-performance polymeric materials especially when the properties of two or more polymers are synergistically combined. It is also one of the most important routes of polymer recycling because it makes the sorting step much simpler during a recycling process.

In particular, PET-PC blends' development and study have caused much interest, thanks to their interesting combination of properties. PET added to PC makes the latter more resistant to organic solvents, provides an opportunity to control the flow viscosity of the molten blend, and reduces the material's cost. PC is helpful in increasing PET's impact strength and improves dimensional stability under operating conditions[5]. Moreover, the blending of these polymers can also be used as recycle procedure. In fact, in the case of PET, recycling is a complex process because of the chemical and mechanical degradation the polymer undergoes. Consequently, re-processing affects mechanical

properties of the recycled products. These properties can clearly be improved by the addition of polycarbonate[6]. As a matter of fact, PET-PC blends have gained scientific and industrial interest since they represent a large potential market in post-consumer sector[7,8]. Because of their significant commercial potential, PET/PC blends have been investigated rather intensively. However, the mixing of these polymers is complex and in most of the cases it gives origin to immiscible blend. As a matter of fact, several blending procedures have been experimented in order to test their miscibility[9,10].

A certain grade of miscibility was reported only after transesterification, as per melt-mixing at high temperature (300 °C) or for long processing time[5]. Melt mixing technique involves a thermal treatment of the polymer blend above the melting point of both of the two polymers, leading to the formation of random copolymers through exchange (transesterification) reaction[11]. The final composition can be affected by side degradation reaction (mainly $CO_2$ and aliphatic carbonate losses)[12], that can be minimized by adding a catalyst (usually titanium butoxide), that allow to obtain a reasonable exchange reaction rate at relatively low temperature (about 240-270 °C)[13]. However, the solubility of PET in solid state PC is rather low, and on cooling phase separation of PET takes place. Indeed, the estimated decreasing $T_g$ of PC with increasing PBT content indicates instability of the blends.[14,15]

When the two polymers are deposited on a substrate from a unique solution via spin-coating, PET/PC blends result in a totally immiscible mixture[16,17]. Many types of morphology can be obtained through this procedure for immiscible polymers. The type of morphology depends on the nature of the polymers (interfacial tension, viscosities, and the ratio of these viscosities), their volume fractions and the processing conditions. The structure of the final blend can be categorized into four basic morphology types (Figure 4.2):

a) Matrix-dispersed particle structures
b) Matrix–fibre structures
c) Lamellar structures
d) Co-continuous structures

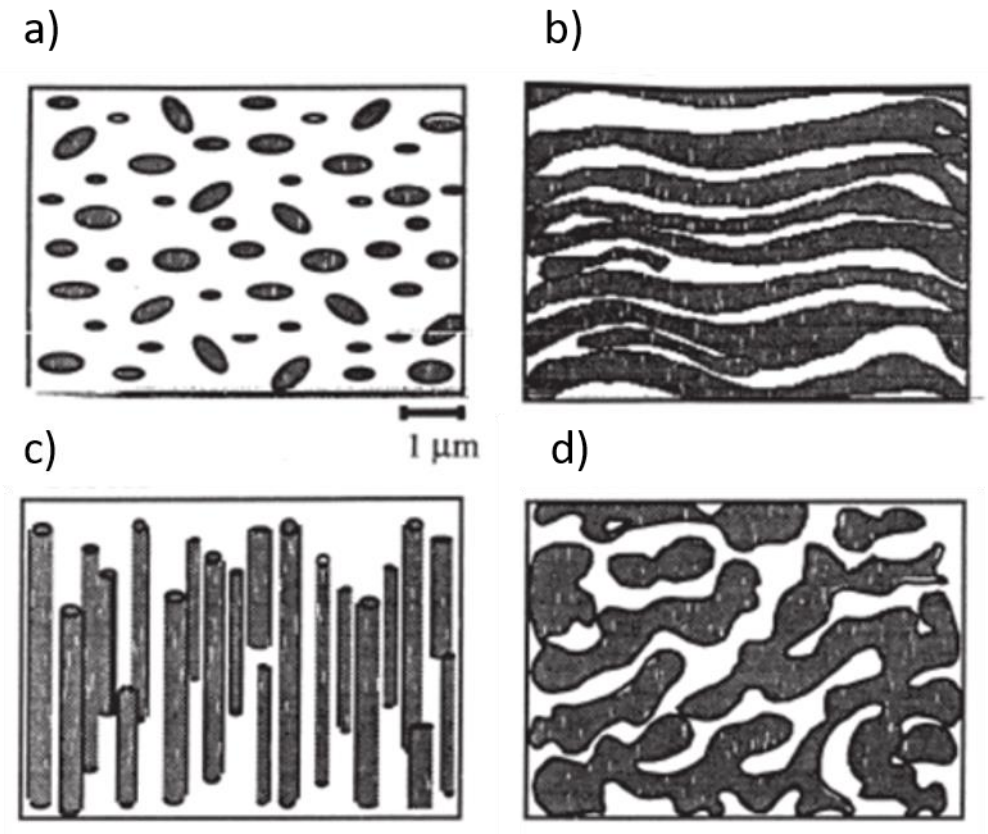


Figure 4.2: four basic morphology types **a)** Matrix-dispersed particle structures, **b)** Matrix–fibre structures, **c)** Lamellar structures, **d)** Co-continuous structures

Depending on the evaporation rate of solvent and the volume ratio of the polymers in the solution, it is possible to obtain many different types of highly structured thin films[18]. For all the possible morphologies, however, the polymers are not chemically mixed. Rather, the polymers are constrained in a "out-of-equilibrium" state, which makes them very unstable. This instability can yield structure modifications, especially following thermal or photo degradation events. The extent of structure modifications highly depends on the different interfacial mobilities of the two polymers, which is influenced by the temperature[19].

Long-term properties of polymer blends under environmental stresses are strongly influenced by the chemical-physical properties of the individual component polymers. The final state of the blends at the end of their lifetime is difficult to predict from the basis of the individual polymers, however. Consequently, the degradation behaviour of blends is not understood without experiments[20]. As a matter of fact, the type of the morphology and its phase dimensions determine the final properties of a polymer blend. For this reason, the investigation of the mechanisms involved in thermal and photo-degradation of immiscible polymer blends assumes a fundamental role in the forecast of the chemical-physical properties of the final materials[21]. Therefore, an accurate investigation of the polymer blends can provide a better understanding of the long-term behaviour of virgin blends.

Monitoring a thermal ageing process can be very challenging, however. The standard experimental set-up for thermal ageing involves annealing in specific environmental chambers in a nitrogen atmosphere for a given amount of time. After the annealing procedure is completed, an imaging technique is required for the investigation of the post-thermal ageing morphology. Several techniques have been explored for this aim, such as electronic microscopies, atomic force microscopy or scanning tunnelling microscopy [22,23,24]. In particular, the latter have been extensively used for the investigation of the surface properties. Yet, in previous times, these techniques above have provided results only after the annealing has been completed.

In order to deepen the understanding of the mechanisms of thermal ageing phenomena on polymer blends, performing an analysis of the surface's chemistry and morphology during the annealing process could provide much needed information about the specific times and/or temperatures for changes to be seen in the blend. Since prediction of blend behaviour is not possible from the individual polymers' behaviour, the prior methodology could require many successive attempts of annealing then characterization to discover at what temperature and time the blend change is occurring. Misunderstandings could occur if care is not taken, and significant time may be required to ensure accurate determination of the behaviour. In addition, the behaviour of the blend during a transition is lost since the characterization takes place before and after the anneal is complete. Thus, an in situ characterization providing chemical and morphological information during an anneal, would represent a significant advance in how new blends could be understood.

In this thesis work, ToF-SIMS imaging performed during a thermal treatment experiment is presented for a PET-PC blend. This work demonstrates that ToF-SIMS can provide information on the microstructure modification of the blend, in particular on the surface, over the course of the annealing experiment. While this was performed for a PET-PC blend, this technique can be extended to other polymer blends, and is evidence for the usefulness of ToF-SIMS for the development and understanding of polymer science.

## 4.2. Thesis work

As stated previously, blends of PET and PC represent a perfect example of the complex interplay between two immiscible polymers. In fact, even in the presence of transesterification reactions, this blend shows several kinds of phase separation. In particular, the spin coating deposition technique can yield many unpredictable behaviours and a wide range of different morphologies for the polymers.

ToF-SIMS is a powerful imaging technique, and it has been extensively exploited for the investigation of polymer structures[25]. In fact, in comparison with other imaging techniques, it is able to provide

molecular information and chemical bonding of materials under the micrometre scale. Thanks to this sensitivity, ToF-SIMS has been utilized for the study of the polymers' surface[26,27], which is fundamental to the understanding of their interaction with the exterior.

In this thesis, it is shown that different morphological typology can be achieved depositing thin films of PET/PC blends via spin-coating. Since this deposition technique is unpredictable, spin-coating is a model for demonstrating the superiority of ToF-SIMS to rapidly ascertain ageing phenomena without an *a priori* understanding of a blend's behaviour. By using the high spatial resolution of ToF-SIMS, these different morphologies can be distinguished. As well, the capability of ToF-SIMS to reveal even small differences in the surface structure was exploited to monitor the changes due to thermal treatment. In particular, temperature-programmed ToF-SIMS experiments were carried out by acquiring ToF-SIMS images along a certain temperature ramp. It was therefore possible to "see" in real time how the "out-of-equilibrium" polymers behaved and to gain some information about their physical-chemical properties.

## 4.3. Materials and Methods

### 4.4.1 Preparation of the films

Polyethylene terephthalate (PET) and poly-bisphenol-A-carbonate (PC) were purchased from Sigma Aldrich (molecular structures in Figure 4.3). A 2% w/w solution was prepared in chloroform/1,1,1,3,3,3-hexafluoro-2-propanol (90/10 vol%) (Sigma Aldrich), using a 75% PET- 25% PC composition. The solution was poured on a rotating plate of a spin-coater using a silicon wafer as substrate. In order to explore different blend morphologies, two different coating programs were set, differing each other for the maximum rotation speed (1000 rpm or 2000 rpm) that was reached in both cases with the same acceleration (40 rounds $s^{-2}$). Once the maximum rotation speed value was reached, it was maintained for 800 sec in order to allow for complete solvent removal.

The film thickness measurements were carried out by means of a stylus profilometer KLA-Tencor P7 equipped with a capacitive sensor which allows surface roughness measurements to be carried out for many kinds of materials with high resolution. The thickness was measured as height difference between the average height of film surface and the substrate exposed at the bottom of a straight incision created on the polymeric films by gently scratching the film by means of a razor blade.

The profilometer parameters were set as follows: scan speed 20 μm/s, sampling rate 50 Hz, point interval 0.4 μm, applied force 0.50 mg and vertical resolution 8 nm. The average film thicknesses were evaluated to be about 800 nm.

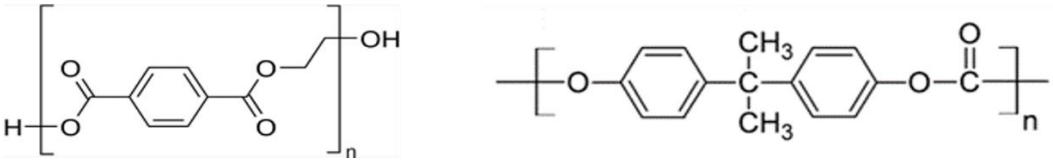

Figure 4.3: chemical structure of polycarbonate (right) and polyethylene terephthalate (left)

### 4.4.2 Temperature programmed ToF-SIMS imaging

For the temperature programmed experiments, the temperature control was achieved by using an IPS Eurotherm unit, which is able to monitor and tune the temperature of the sample, that is mounted on the commercial heat/cool sample holder produced by ION-TOF. In these experiments, samples underwent a temperature ramp from -10°C to 330°C, inside the ToF-SIMS main chamber. The cold temperatures were reached by cooling the sample through a $LN_2$ cold finger in thermal contact with the sample holder. The controlled increase of temperature is obtained by resistive heating of the holder by means of the feedback circuit of IPS unit which constantly monitors the surface temperature with a thermocouple and provides the right heating current in order to obtain the desired temperature ramp.

ToF-SIMS images were acquired by means of a TOFSIMS IV spectrometer (IONTOF) in bunched modality by using a pulsed $Bi_3^+$ ion beam (25 keV, 0.5 pA) with a raster of 500×500 $\mu m^2$ area and 256 × 256 pixels. Surface charge compensation was accomplished by pulsed low energy electron flood, in order to avoid charging effects.

Every temperature increases of 15 °C a secondary ion image was acquired on the same sample area. In order to minimise ion-beam-induced sample damage, the primary ion fluence was kept below $2\times10^{11}$ ions $cm^{-2}$ for each single experimental point, so that the ion fluence experienced by the sample along the entire temperature-programmed experiment remained < $5\times10^{12}$ ions $cm^{-2}$. This allowed the observation of the same sample area during the whole temperature treatment. The images were reconstructed by following two diagnostic fragments of the polymers, $C_{14}H_{11}O_2^-$ (*m/z* 211.07) for PC and $C_7H_5O_2^-$ (*m/z* 121.02) for PET, and successively shown in false colours with the ION-TOF palette respectively *Thermomap1*.

## 4.4. Results and Discussion

### 4.4.1 Preliminary analyses

Figure 4.4 shows the typical postive spectrum, acquired at ambient temperature, of a PET(75%)-PC(25%) blend, deposited via spin coating, according to the procedure described in the section "materials and method". It is possible to observe characteristic peaks of both polymers, although the most intense signals pertain to PET. In particular, $C_6H_4^+$ (*m/z* 76.03), $C_7H_4O^+$ (*m/z* 104.02) $C_8H_5O_3^+$ (*m/z* 149.02) are specific fragments of PET (blue) while $C_9H_{11}O^+$ (*m/z* 135.08) is a specific fragment of PC (red).

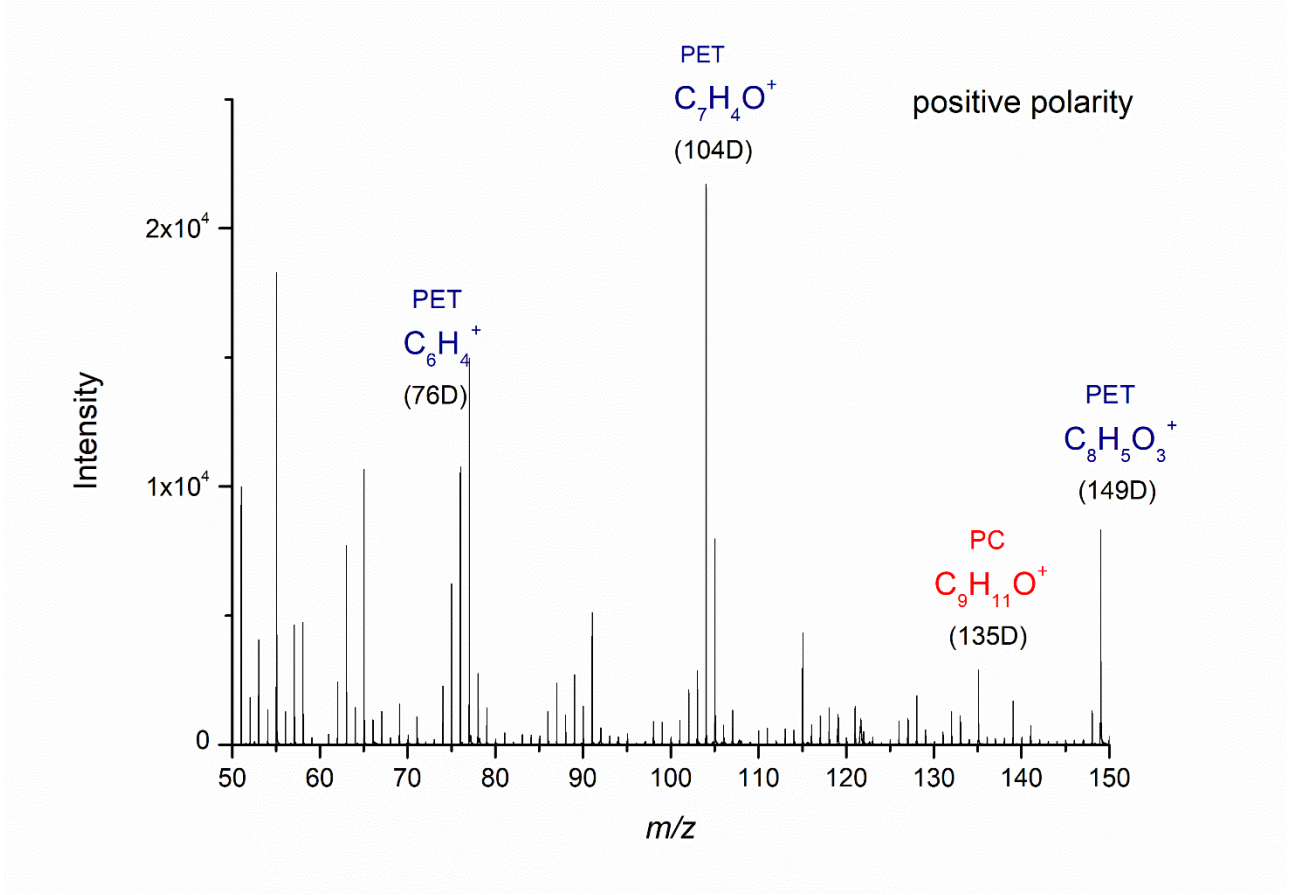


Figure 1.4: positive spectra of PET-PC blend

Table 4.1 and 4.2 display the theoretical *m/z* values of the fragments, the *m/z* detected values and the standard deviations, which allowed to verify the accuracy of the identification.

Table 4.1: main PET characteristic signals (positive polarity)

| PET Fragment | Theoretical Mass (*m/z*) | Detected Mass (*m/z*) | Standard deviation (%) |
|---|---|---|---|
| $C_6H_4^+$ | 76.0308 | 76.0285 | -30.1 |
| $C_7H_4O^+$ | 104.0257 | 104.0238 | -17.9 |
| $C_8H_5O_3^+$ | 149.0233 | 149.0280 | 31.1 |

Table 4.2: main PC characteristic signals (positive polarity)

| PC Fragment | Theoretical Mass (*m/z*) | Detected Mass (*m/z*) | Standard deviation (%) |
|---|---|---|---|
| $C_9H_{11}O^+$ | 135.0804 | 135.0817 | 9.6 |

Figure 4.5 shows an example of the negative spectrum of a the same blend with the assignment of some characteristic peaks of both polymers. We indicated in blue the characteristic fragments of PET $C_6H_4^-$ (*m/z* 76.03), $C_7H_5O_2^-$ (*m/z* 121.02), $[M\text{-}H]^-$ (*m/z* 191.05). The characteristic peaks of PC $C_6H_5^-$ (*m/z* 77.03), $C_6H_4O^-$ (*m/z* 93.03), $C_8H_5O^-$ (*m/z* 117.03), $C_9H_9O^-$ (*m/z* 133.06), $C_{14}H_{11}O_2^-$ (*m/z* 211.07), $C_{15}H_{11}O_4^-$ (*m/z* 255.06) are shown in red. Table 4.3 and 4.4 report the standard deviation of the detected *m/z* values as compared to the theoretical ones.

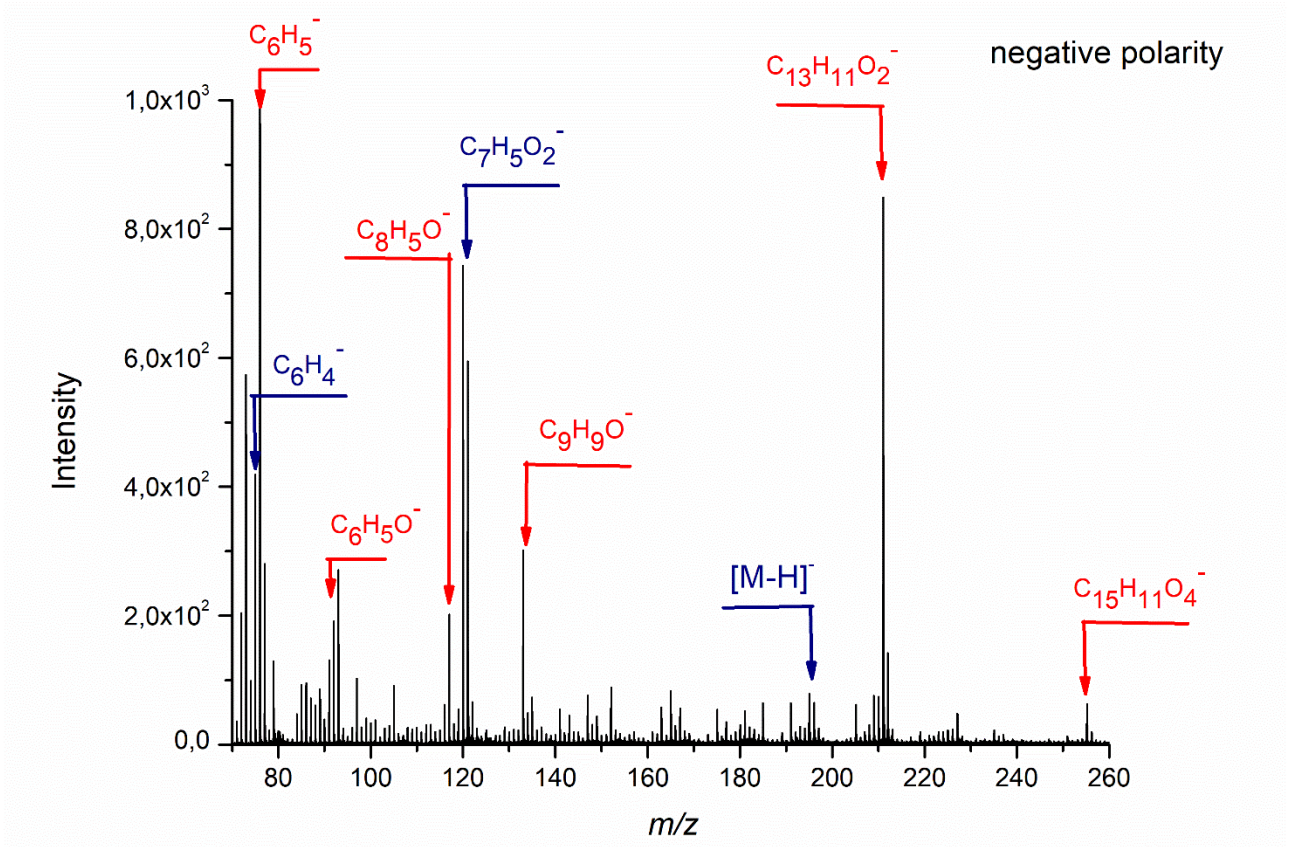


Figure 4.5: negative spectrum of PET-PC blend

Table 4.3: PET characteristic fragments (negative polarity)

| PET Fragment | Theoretical Mass (*m/z*) | Detected Mass (*m/z*) | Standard deviation (%) |
|---|---|---|---|
| $C_6H_4^-$ | 76.0318 | 76.0291 | -35.7 |
| $C_7H_5O_2^-$ | 121.0295 | 121.0336 | 33.8 |
| $[M\text{-}H]^-$ | 191.0502 | 191.0484 | -9.9 |

Table 4.4: PC characteristic fragments (negative polarity)

| PC Fragment | Theoretical Mass (*m/z*) | Detected Mass (*m/z*) | Standard deviation (%) |
|---|---|---|---|
| $C_6H_5^-$ | 77.0397 | 77.0438 | 54.1 |
| $C_6H_4O^-$ | 93.0346 | 93.0300 | -49.6 |
| $C_8H_5O^-$ | 117.0346 | 117.0209 | -117.0 |
| $C_9H_9O^-$ | 133.0659 | 133.0517 | -106.8 |
| $C_{14}H_{11}O_2^-$ | 211.0765 | 211.0502 | -124.3 |
| $C_{15}H_{11}O_4^-$ | 255.0663 | 255.0963 | 117.6 |

### 4.4.2 PET-PC blend imaging

The characterization of morphology for melt mixed PET-PC blends has already been reported in the literature. For blends obtained by this methodology, the morphology varies from a quasi-homogeneous to separation of domains, according to the melt mixing procedure employed and the presence of catalysts[8]. When domains are observed, the system is constituted of a PET matrix and a PC dispersed phase with interfacial regions consisting of bridge-like structures, linking the matrix and the dispersed domains. These bridges are correlated to the presence of a PET-PC block copolymer obtained through chemical reactions occurring during blending in the molten state[24].

In the case of spin cast blends, the studies are not numerous. Notwithstanding, it is well known that phase separation occurs for this immiscible polymer blend, but no robust investigations on spin- cast PET-PC morphology are reported. As stated previously, the structure of an immiscible polymer blend can be categorized into four basic types of morphology: matrix-dispersed particle structures, matrix–fibre structures, lamellar structures, and co-continuous structures. Of all the possible morphologies, the co-continuous morphology is the least predictable. As a result, its identification can be particularly challenging and requires several analyses through different techniques.

To investigate possible morphologies that can be obtained through the spin-coating, two classes of samples made of PET/PC were prepared by varying the spin coating parameters. Figure 4.6 shows secondary ions images (negative polarity) of 75% PET- 25% PC thin film, obtained at a spinning rate of 2000 rpm. In Figure 4.6 we report: **a)** the sum of PET characteristic peaks ($C_6H_4^-$ at m/z 76.03 and $C_7H_5O_2^-$ at m/z 121.03) and **b)** the sum of PC characteristic peaks ($C_{14}H_{11}O_2^-$ at m/z 211.07 and $C_9H_9O^-$ at m/z 133.07). In this case the morphology appears as a matrix-dispersed particle type, characterized by two polymeric domains with circular “patchworked” structures of PC embedded in a PET matrix.

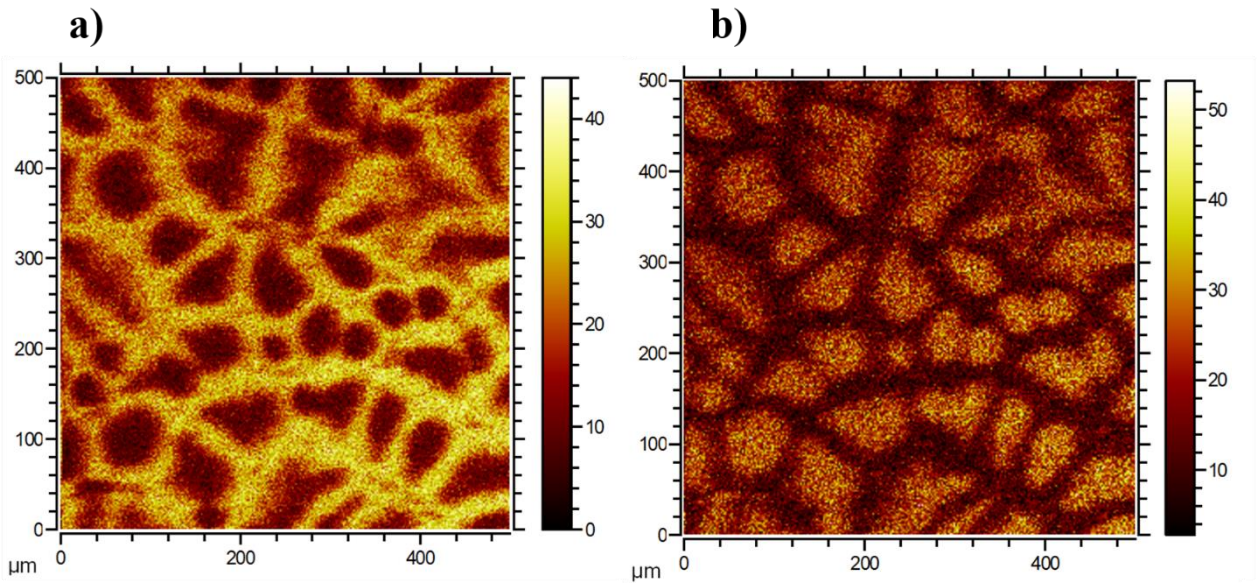


Figure 4.6: negative chemical maps of **a)** the sum of PET characteristic peaks, **b)** the sum of PC characteristic peaks

Figure 4.7 displays the secondary ion images for a sample deposited by spin coating at lower spinning rate, namely 1000 rpm, from the same PET-PC solution. In this case, the negative polarity showed stronger intensity and this, together with the fact that PC signals are more abundant in negative polarity, is the reason why, for the sake of easier comparison, negative ion polarity images are reported for all the samples. In Figure 4.7 the intensity distribution of **a)** the characteristic fragment of PET $C_7H_5O_2^-$ at *m/z* 121.03 and **b)** the PC characteristic fragment $C_{14}H_{11}O_2^-$ at m/z 211.07 are reported. A phase separation is again evident. However, with a lower spinning rate for film deposition, a matrix–fibre structure was obtained in contrast with the matrix dispersed type of the 2000 rpm case.

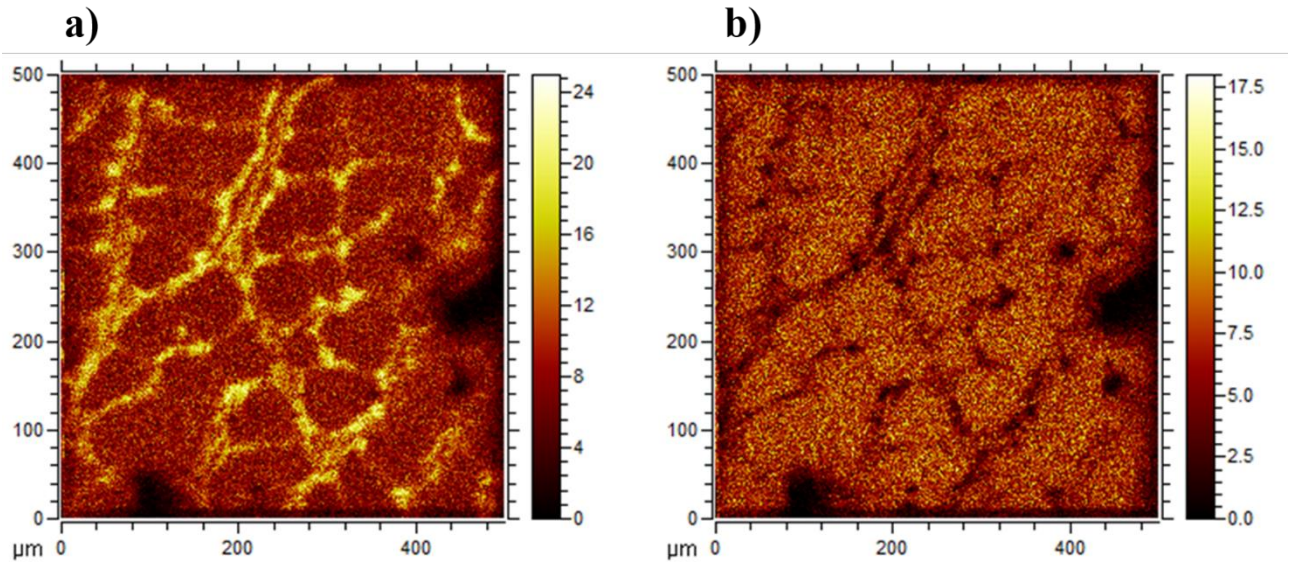


Figure 4.7: negative chemical maps of **a)** PET characteristic peak, **b)** PC characteristic peaks.

Summarizing, Figures 4.6 and 4.7 represent the typical morphologies obtained for the 75% PET- 25% PC solution at spinning rate of 2000 and 1000 round/min, respectively. At decreased spinning rate, we observe a change from dispersed PC domains in a PET matrix to a fibre morphology of PET in PC. As mentioned in the introduction, however, the relationship between the spin-coating parameters and resulting morphology is not of trivial explanation. As the aim of this work was the demonstration of ToF-SIMS as a characterization tool to aid in polymer development, rather than the polymer development itself, the observation of the two morphologies and the demonstration that it is possible to distinguish them through the secondary ions images was satisfactory *per se*. Further studies to observe the effect of other deposition conditions on the deposited morphology would be appropriate, if the aim was to understand how the morphology affects the properties of the blend. However, such study is outside the scope of the present work so that, for now, a proof that the ToF-SIMS measurement can distinguish the different regions with high resolution must be considered satisfactory.

### 4.4.3 Temperature-programmed ToF-SIMS experiments

Following the initial "morphological" investigation, the subsequent goal was to investigate the capability of ToF-SIMS to show in real-time ("live") the changes that an immiscible polymer blend undergoes during a thermal treatment procedure and possibly to determine temperature's effect on its stability, either chemical or morphological. In contrast to other reported methods, where characterization is made after a previously performed annealing, here the attempt is to monitor blend morphology and chemistry *during* the annealing experiment, and to observe the temperature at which changes do occur. It cannot be underestimated the advantage of this approach which would allow – if successful – the study of temperature behaviour of the blend within a single annealing experiment. In a broad sense, the term "degradation of polymers" includes all changes in chemical structure and physical properties of polymers due to external chemical or physical stresses leading to materials with characteristics different from those of the starting material[28]. Thermal ageing is one of the most frequent and important stresses that affect polymer properties and can cause irreversible damage. As stated previously, PET-PC mixtures are totally immiscible and unstable especially when deposited *via* spin-coating. In fact, this technique brings the system to an *out-of-equilibrium* condition, where the polymers' chains are "frozen" in a non-minimum-energy status which is challenging to investigate. So far, a real-time *in situ* imaging investigation of the thermal behaviour of spin cast PET-PC blend has never been reported.

When energy is provided to the polymer chains, for instance by increasing temperature, they will have the possibility to migrate to find new positions or configurations which allows the system to stabilise at lower surface free energy. The exact energy required for a change to occur is not known a priori, especially with a new polymer blend. In the case of PET/PC, its temperature behaviour has been extensively studied in melt-mixing studies. However, as pointed out above, the spin-coating process can lead to difficult-to-foresee metastable situations that can, in some way, mimic the situation of a "new" blend. Characterizing the "new" blend with ToF-SIMS imaging while annealing it *in-situ*, can be a quick and effective way for characterising the thermal evolution of the system.

Based on the study reported in § 4.4.2, a sample prepared at 1000 round/min was chosen for the temperature-programmed SIMS imaging study. The fibres-matrix morphology was selected since literature already reports annealing studies carried out on polymer blends with this morphology. In particular, it was found out that the fibres tend to break up during annealing. This was proved by extraction experiments before and after the annealing[29].

Figure 4.8 shows the secondary images in negative polarity, in particular the intensity maps of two characteristic polymers' signals: $C_7H_5O_2^-$ at *m/z* 121.02 for PET and $C_{14}H_{11}O_2^-$ at *m/z* 211.07 for PC. Images were acquired along a temperature ramp from -10°C up to 320°C with 15°C intervals.

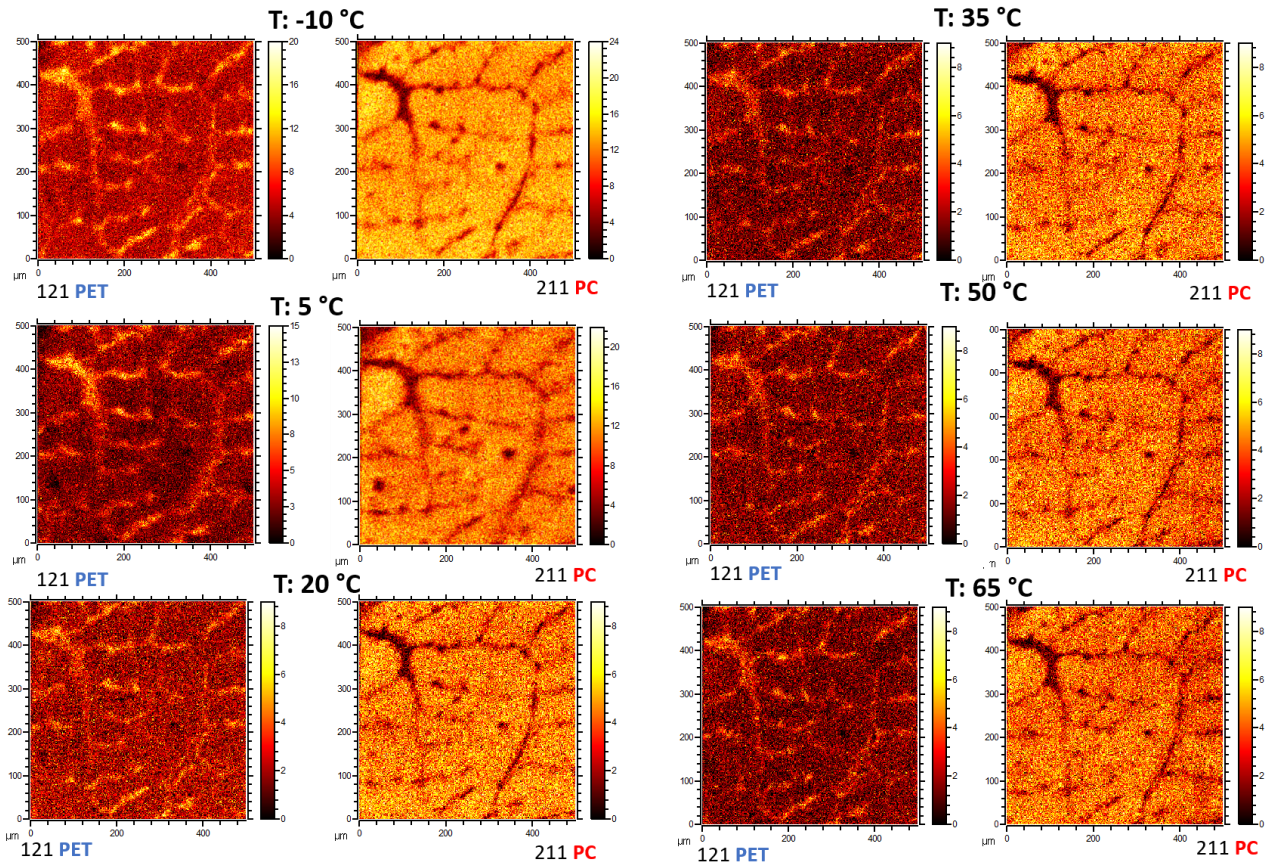

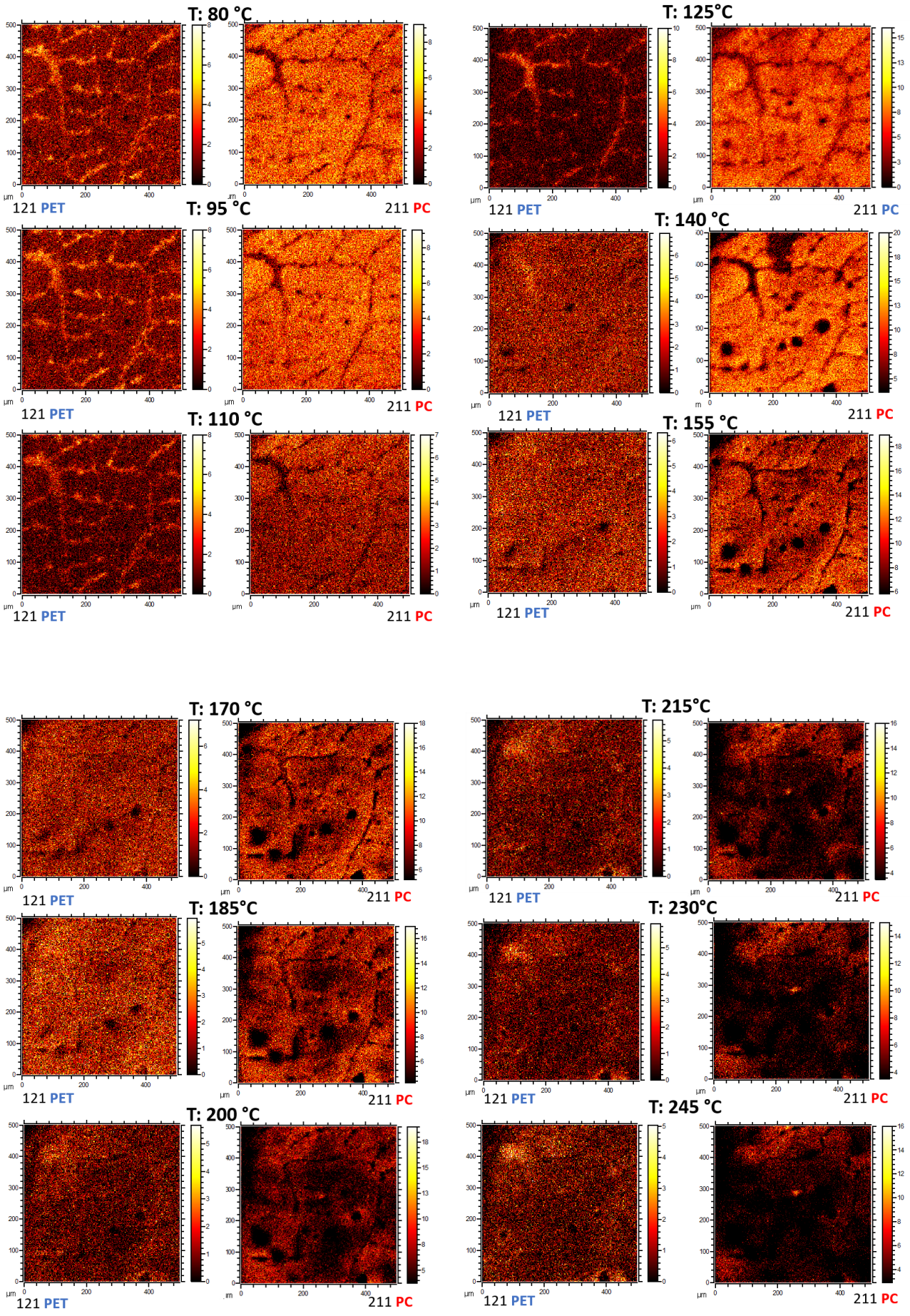
T: 80 °C
121 PET
211 PC
T: 125°C
121 PET
211 PC
T: 95 °C
121 PET
211 PC
T: 140 °C
121 PET
211 PC
T: 110 °C
121 PET
211 PC
T: 155 °C
121 PET
211 PC
T: 170 °C
121 PET
211 PC
T: 215°C
121 PET
211 PC
T: 185°C
121 PET
211 PC
T: 230°C
121 PET
211 PC
T: 200 °C
121 PET
211 PC
T: 245 °C
121 PET
211 PC

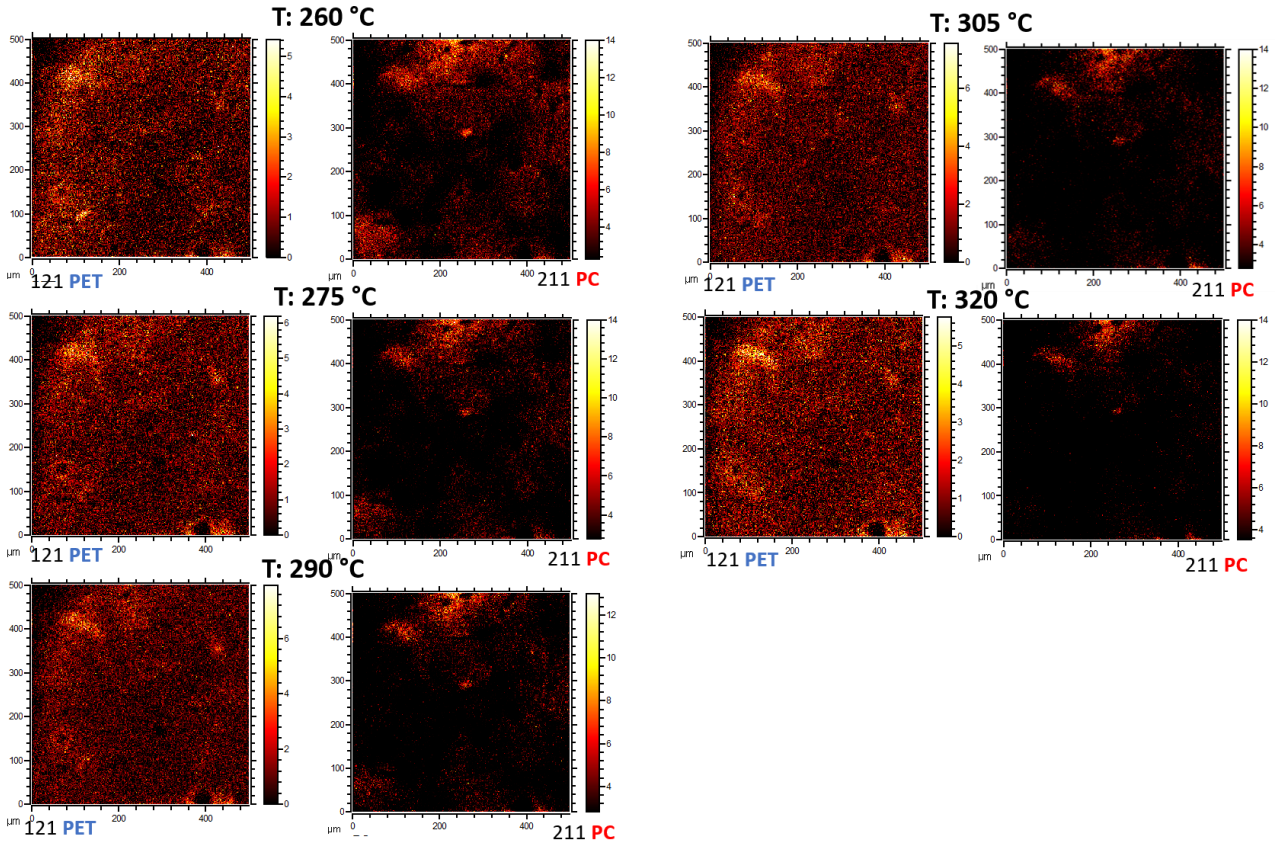


Figure 4.8: chemical maps of PET and PC at various Temperatures

These images show that at lower temperatures it is possible to distinguish the matrix-fibres morphology. With increasing temperature, important changes occur approximately between 100°C and 150°C, when it becomes increasingly difficult to distinguish the PET fibres, while the PC counterpart retains, in some extent, the original morphology up to about 185°C, when it starts to become blurred and then to disappear at higher temperatures.

Some additional indication useful for the interpretation of the temperature evolution of the blend film can be obtained by plotting, as function of temperature, the intensity of the same characteristic peaks considered in Figure 4.8.

The intensities of the two characteristic signals for PET and PC as function of temperature are reported in Figure 4.9, along with the chemical maps corresponding to some key points of the plot. The initial decay of both intensities, reasonably, is due to the desorption of volatile species at the surface (most probably water condensed during the initial sample freezing) that can affect the ionization probability of both polymers. Starting from 20°C, we observe a general trend of slow decrease of the intensities, that could be due, at least partly, to thermal degradation of the polymers. Also, a contribution due to the accumulation of beam-induced damage cannot be ruled out. Superimposed to this intensity drift, we note some sudden and relatively sharp variations, more evident on PC signal, in the temperature interval at approx. 90° and 150°C.

In fact, we observe that a decrease of about 50% of PC intensity occurs around 100°C, followed by its strong increase up to a maximum at about 145°C. Above this temperature, a continuous decay is observed. This signal variation has been carefully verified and we can exclude that it is due to instability of the analytical beam. Rather, one should hypothesize that the observed variations are associated with some characteristic property of the binary system under investigation.

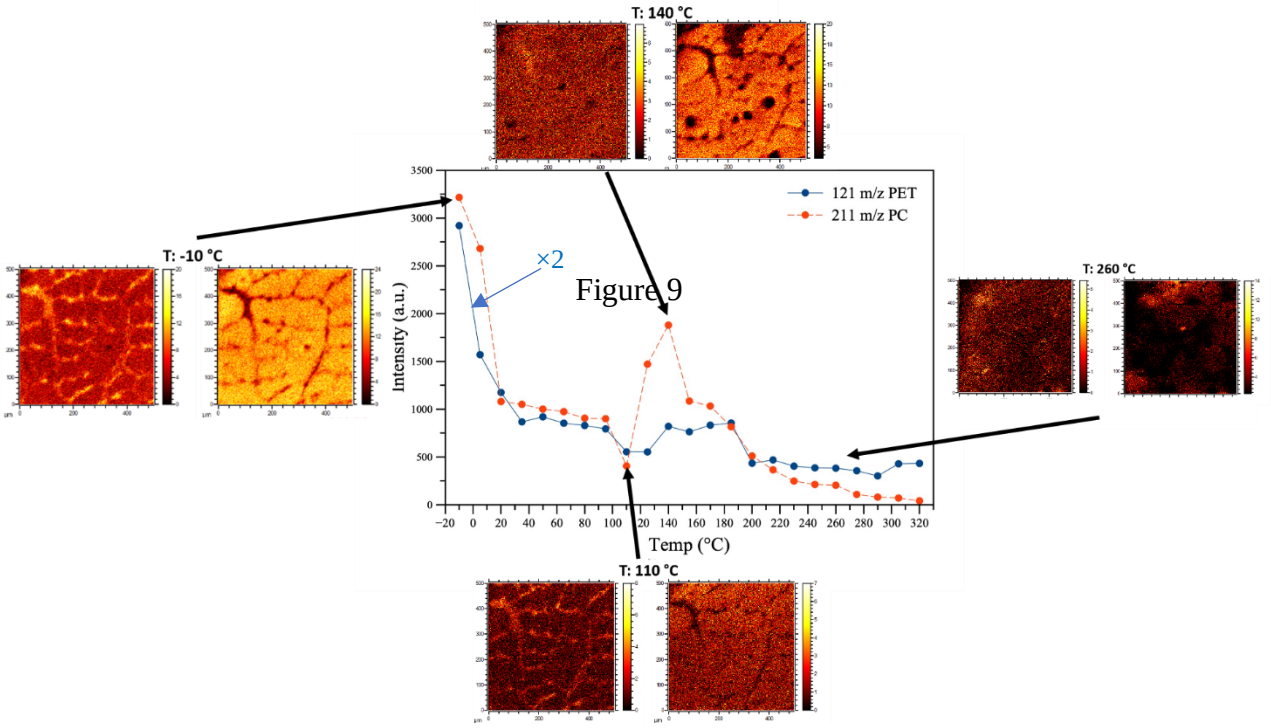


Figure 4.9: the intensities of the two characteristic signals for PET and PC as function of temperature

Actually, it is well known that $T_g$ of PET is around 85°C and $T_g$ of PC is around 145°C, and the sharp intensity variations in the plot of figure 9 do occur remarkably close to these temperatures. This observation is consistent with the presence, at lower temperatures, of separate domains of pure polymers, as indicated also by ToF-SIMS data which, within the limits given by the non-optimal lateral resolution connected with the high mass resolution imaging modality – bunched mode – used, show no intermixing of the two components. Indeed, as stated in the introduction, in the case of completely immiscible blends, each component polymers should retain its individual $T_g$ value. DSC experiments, reported in literature for melt-mixed PET-PC blends, show that when transesterification does not take place, because of absence of catalysts or insufficient processing time, no copolymer blocks are formed and in such a situation the blend exhibits two glass transitions, indicating the presence of two amorphous phases. Moreover, no shifts of the $T_g$ values occur[18], and the two polymers maintain their own individual $T_g$. In the present case, since we observe that there are two transition points at temperatures which are close to the glass transition temperatures of the two individual polymers, we can conclude that, at least in the experimental condition used, no major reaction/mixing phenomena do occur in the system. This is confirmed by the fact that no signals specific of transesterification reaction fragments[25] do appear in the spectra.

It must be pointed out that a precise interpretation of the evolution of the intensities or the two characteristic peaks reported in Figures 4.8-4.9, however, is difficult because a change in the structure of each polymer around the glass transition can already produce variations in SIMS intensities.

Moreover, we must consider that, when polymers are in the physical state of elastic solid, well below the glass transition temperature ($T_g$), no chain movements can occur, but above the glass transition the polymer chains acquire more degrees of freedom, allowing movements which can deform the morphology of the solid structure and also allow the migration and or segregation of chain segments. Such enhanced chain mobility above the glass transition temperature can favour the preferential surface segregation of certain chain segments, and this, in turn, can cause a variation of the observed SIMS intensities because of both the increased surface concentration of certain chain segments and the possible matrix effect associated with these compositional changes at the surface.

In spite of the difficulties in the detailed interpretation of the data presented in figures 4.8 and 4.9, we can surely state that the *in-situ* temperature-programmed ToF-SIMS imaging measurements allowed us to get an overall picture of the behaviour of the blend under examination, providing evidence of its behaviour, at least up to 150°C, as immiscible two-components system which is retaining the glass transition temperatures of each component. At higher temperatures, the imaging data show a progressive disruption of the original morphology, which is consistent with the fact that PC is expected to melt in the temperature range 185-230 °C[31] and PET undergoes melting in the range 230-

260°C[31]. Although the detailed melting behaviour is known to depend on the thermal history of the sample (and on its crystallinity)[30,31] we observe that the total disappearance of the initial morphology in the chemical maps of figure 8 occurs in the same temperature interval, confirming again the potentiality of temperature-programmed ToF-SIMS imaging for in-situ study of the thermal evolution of complex polymer systems. This also in view of the fact that, for each temperature point, a large amount of data can be extracted from the high-resolution mass spectra reconstructed from the acquired raw data.

## 4.5. Conclusion

In this chapter we presented the imaging study of PET/PC blends spin cast with different deposition parameters. A preliminary ToF-SIMS imaging characterization allowed us to recognise different microstructures formed in the different deposition conditions. Although not unexpected, this result was used for choosing a particular starting morphology for a temperature-programmed ToF-SIMS imaging experiment, which represents the innovative part of the study. Indeed, at our knowledge, no previous experiment of this type has been reported previously. The images obtained at different temperatures, together with the behaviour of overall intensities of some characteristic fragments, allowed us to individuate the changes in morphology and surface composition connected with the glass transition temperatures of the two component polymers of this well-known model system. Moreover, it was possible to follow the surface morphology and composition of the system up to more than 300°C when the system is expected to be in a melt state. The information extracted from the experiment shows that, in the temperature range explored and in the timescale of the experiment, no detectable transesterification reaction occurs.

It is probably worth to remark that the results described in this chapter, beyond the specific information grasped about the particular model system under study, constitute a novel proof-of-concept of the applicability of temperature-programmed ToF-SIMS imaging for the study or the thermal evolution of structured organic systems. Moreover, some limitations in the interpretation of the acquired data, arisen in the present study, could be overcome through the application of specific data treatment methodologies such as those applied to the systems in the next two chapters of this thesis work.

*References*


1. M Frigione. Compatibilization *criteria and procedures for binary blends: a review*. Journal of Polymer Engenie 1997;17(6). doi:https://doi.org/10.1515/POLYENG.1997.17.6.429
2. Rauwendaal C. *Mixing in Polymer Processing*. Marcel Dekker; 1991.
3. Ju.S.Bessonov Thermodynamics of mixing of polymers. *European Polymer Journal*. 1975;11(4):321-326. doi:https://doi.org/10.1016/0014-3057(75)90043-9
4. Robert L. Scott and Michael Magat. The Thermodynamics of High-Polymer Solutions: I. The Free Energy of Mixing of Solvents and Polymers of Heterogeneous Distribution. *J Chem Phys*. 13:172. doi:https://doi.org/10.1063/1.1724018
5. Pesetskii SS, Jurkowski B, Koval VN. Polycarbonate/polyalkylene terephthalate blends: Interphase interactions and impact strength. *Journal of Applied Polymer Science*. 2002;84(6):1277-1285. doi:10.1002/app.10472
6. Fraïsse F, Verney V, Commereuc S, Obadal M. Recycling of poly(ethylene terephthalate)/polycarbonate blends. *Polymer Degradation and Stability*. 2005;90(2 SPEC. ISS.):250-255. doi:10.1016/j.polymdegradstab.2005.02.019
7. Beigbeder J, Perrin D, Mascaro JF, Lopez-Cuesta JM. Study of the physico-chemical properties of recycled polymers from waste electrical and electronic equipment (WEEE) sorted by high resolution near infrared devices. *Resources, Conservation and Recycling*. 2013;78:105-114. doi:10.1016/j.resconrec.2013.07.006
8. Yang Z, Peng H, Wang W, et al. The effect of different compatibilizers on the properties of a post-industrial PC/PET blend. *Journal of Polymer Science, Part B: Polymer Physics*. 2016;41(1):1575-1593. doi:10.1002/polb.20095
9. Carrot C, Mbarek S, Jaziri M, Chalamet Y, Raveyre C, Prochazka F. Immiscible blends of PC and PET, current knowledge and new results: Rheological properties. *Macromolecular Materials and Engineering*. 2007;292(6):693-706. doi:10.1002/mame.200700006
10. Ignatov VN, Carraro C, Tartari V, et al. PET/PC blends and copolymers by one-step extrusion: 1. Chemical structure and physical properties of 50/50 blends. *Polymer*. 1997;38(1):195-200. doi:10.1016/S0032-3861(96)00558-7
11. Montaudo G, Puglisi C, Samperi F. Mechanism of exchange in PBT/PC and PET/PC blends. Composition of the copolymer formed in the melt mixing process. *Macromolecules*. 1998;31(3):650-661. doi:10.1021/ma9712054
12. F. Pilati E. Marianucci C. Berti. Study of the reactions occurring during melt mixing of poly(ethylene terephthalate) and polycarbonate. *Journal of Applied Polymer Science*. 1985;30(3):1267-1275. doi:doi.org/10.1002/app.1985.070300330

13. Vladimir N.lgnatov, Claudio Carraro, VittorioTartari, Roberto Pippa, Francesco Pilati, Corrado Berti, MaurizioToselli M. Reactive blending of commercial PET and PC with freshly added catalysts. *Polymer*. 1996;37(26):5883-5887. doi:doi.org/10.1016/S0032-3861(96)00610-6

14. D. C. Wahrmund D. R. Paul J. W. Barlow. Polyester–polycarbonate blends. I. Poly(butylene terephthalate). *Applied Polymer Science*. 1978;22(8):2155-2164. doi:doi.org/10.1002/app.1978.070220808

15. WOO NYON KIM and CHARLES M. BURNS. Phase Behavior of Blends of Polycarbonate with Partially Miscible Polymers. *Journal of Applied Polymer Science*. 1990;41:1575-1593.

16. C. J. Lawrence. The mechanics of spin coating of polymer films. *The Physics of Fluids*. 31(10):2786. doi:doi.org/10.1063/1.866986

17. K. Norrman, A. Ghanbari-Siahkalia and NBL. studies of spin-coated polymer films. *Annu Rep Prog Chem, Sect C: Phys Chem*. 2005;101(6):174-201. doi:doi.org/10.1039/B408857N

18. Kong Y, Hay JN. Miscibility and crystallisation behaviour of poly(ethylene terephthalate)/polycarbonate blends. *Polymer*. 2002;43(6):1805-1811. doi:10.1016/S0032-3861(01)00772-8

19. Willemse RC. Co-continuous morphologies in polymer blends:stability. *Polymer*. 1999;40(8):2175-2178. doi:10.1016/S0032-3861(98)00430-3

20. Hamid DSH. *Handbook of Polymer Degradation*. (Halim Hamid S, Amin MB, Maadhah AG, ed.). LaMantia FP

21. Machiels AGC, Denys KFJ, van Dam J, Posthuma De Boer A. Formation, stability, and properties of in-situ composites based on blends of a thermotropic liquid crystalline polymer and a thermoplastic elastomer. *Polymer Engineering and Science*. 1996;36(19):2451-2466. doi:10.1002/pen.10643

22. Mendes LC, Pereira PS da C. Optical Microscopy as a Tool to Correlate Morphology and Thermal Properties of Extruded PET/PC Reactive Blends. *Materials Sciences and Applications*. 2011;02(08):1033-1040. doi:10.4236/msa.2011.28140

23. Hiltner, R. Adhikari, W. Lebek, R. Godehardt, S. Henning, G. H. Michler EBA. Investigating morphology and deformation behavior of multilayered PC/PET composites. *Polymers for Advanced Technologies*. 2005;16(2-3):95-101. doi:doi.org/10.1002/pat.579

24. Mendes LC, Pereira PSC. Solid state polymerization: Its action on thermal and rheological properties of PET/PC reactive blends. *Polimeros*. 2013;23(3):298-304. doi:10.4322/polimeros.2013.031

25. Auditore A, Samperi F, Puglisi C, Licciardello A. ToF-SIMS investigation of the thermally induced processes at the surface of polyester based polymer blends. *Composites Science and Technology*. 2003;63(8):1213-1219. doi:10.1016/S0266-3538(03)00080-0

26. Awaja F, Pigram PJ. Surface molecular characterisation of different epoxy resin composites subjected to UV accelerated degradation using XPS and ToF-SIMS. *Polymer Degradation and Stability*. 2009;94(4):651-658. doi:10.1016/j.polymdegradstab.2009.01.001

27. Chan CM, Weng LT. Surface characterization of polymer blends by XPS and ToF-SIMS. *Materials*. 2016;9(8). doi:10.3390/ma9080655

28. Francesco Paolo La Mantia Antonino Valenza. Thermo-mechanical degradation of polymer blends. *Macromolecular Materials and Engineering*. 1994;216(1):45-65. doi:doi.org/10.1002/apmc.1994.052160104

29 Willemse R. Co-continuous morphologies in polymer blends:stability. Polymer (1999) 40(8) 2175-2178. Doi:doi.org/10.1016/S0032-3861(98)00430-3

30. S. Sohn, A. Alizadeh, H. Marand. On the multiple melting behavior of bisphenol-A polycarbonate. P*olymer* 2000;41(25):8879-8886. doi.org/10.1016/S0032-3861(00)00110-5

31. R. C. Roberts. The melting behaviour of bulk crystallized polymers. *Journal of Polymer Science Part B: Polymer Letters.* 1970;8:381-384. doi.org/10.1002/pol.1970.110080512

# 5. Probabilistic Neural Network-Based Classifier for ToF-SIMS Polymer Single-Pixel Spectra

ToF-SIMS is one of the most powerful techniques for spatially resolved chemical imaging of surfaces and thin films and is widely applied within the fields of science, technology, and biology. Nevertheless, ToF-SIMS technique still has some apparent limitations and, in some cases, carrying out the analyses becomes impossible for certain organic and hybrid materials because of their low signal intensity. In fact, as state in previous chapters, set of problems relating to the impossibility to achieve a high intensity of the signals still affects this technique, especially for imaging. This issue limits the acquisition of good quality images for a wide range of samples, and in extreme cases, imaging cannot be carried out.

To overcome this issue of low signal-to-noise ratio, one method to increase the signal is collecting many scans of the same sample area. However, does this strategy not only require additional time to acquire extra scans, but also it can cause beam induced damage, especially in the case of organic and polymeric samples. Moreover, a further complication in the large size of the acquired dataset is introduced. These datasets are difficult to handle, and they represent a critical issue especially in the elaboration of the ToF-SIMS images.

As a matter of fact, acquiring more scans generates hyperspectral image data sets, which usually contain 128 × 128, 256 × 256, or even larger number of pixels. For each pixel, a high-resolution mass spectrum is stored which includes several millions of time-of-flight channels. In the case of 3D imaging, which consists of alternating imaging with erosion cycles to create a stack of 2D images, the amount of data is increased by the number of these cycles. Very rapidly the size of the datasets grow beyond which normal data processing can handle. Recently introduced instrumentation can further complicate the problem, because they can combine different types of mass analysis, e.g., ToF and Orbitrap[1]. As a result, normal data processing is not possible because the dataset dimensions. Ultimately, this leaves the user in the same position of being unable to characterize or provide information about a material.

For this reason, it is fundamental to design and develop computing modelling programs able to rework limited signals. Currently, the most popular approaches for handling and interpretation of ToF-SIMS data are based on multivariate analysis methods. Among these, principal component analysis (PCA) and related techniques increasingly became a sort of standard approach in the surface analysis community[2]. Likewise, in the last chapter of this thesis, PCA was used for the study of the secondary

ion images of a 19th century textile coloured with Methylene Blue. PCA shed light on different hidden components of the sample and assisted in the identification of their chemical composition. This approach has shown to be efficacious in the analysis of complex chemical images, where different components and species are present.

Despite the promising results that PCA can perform, in the case of low-counts datasets, PCA can fail due to computational limitations. Therefore, it is sometimes necessary to perform a pre-processing treatment of the dataset[3, 4]. Such pre-treatments (e.g., unit mass binning, peak picking, and integration) often lead to a loss of resolution (either mass or spatial resolution, or both). Moreover, they can be biased by subjective analyst's decisions and by errors of automated peak search/integration routines. In order to avoid these consequences, some methods for multivariate analysis of raw and non-binned data sets have been reported recently. However, none of them are able to overcome aforementioned drawbacks[5]. Consequently, complex datasets still require data pre-treatments, including subsampling, pre-processing wavelet-based, and data compression[6].

In addition to the problem of the large number datasets, as mentioned previously, ToF-SIMS also carries the problem of low signal. In many cases, ToF-SIMS datasets are coming from a single pixel, and while they are almost free of noise, can exhibit very low-intensity (typically up to 99% of zero-signal channels). Therefore, it is necessary to develop methods which exploit such scarcity of signal, but, at the same time, to avoid the continuous increase of information collected by the modern instrumentations.

Neural networks play an active role in pattern recognition, and for this reason their use in science has spread in many fields, including imaging. Many neural network methodologies have been developed, such as multilayer perceptron, time delay neural networks, backpropagation, radial basis function networks and fuzzy neural networks. Among them, Probabilistic Neural Network (PNN) has demonstrated in many cases the ability to learn more quickly than other neural network models and has had success on a variety of applications. Indeed, PNN supplies flexibility and straightforward design, which make the system easy to operate along with the successful classification results.

In this thesis work such an approach is described and has been published in the literature[7], which can extract latent chemical information from ToF-SIMS data, working on uncompressed and unbinned raw data set. In the following, a review of the candidate's work in this article will be provided. In particular, thin films of four different polymers (Polystyrene PS, polymethylmethacrylate (PMMA), polyalphamethylstyrene (PaMS), and polyethylenterephthalate-co-isophthalate (PETi)) were analysed by ToF-SIMS. Successively, a probabilistic neural network (PNN) was designed and trained by the team with the support of the candidate, to provide a correct classification of these four different polymers.

## 5.1. Thesis work

As stated above, for every primary beam pulse in a ToF-SIMS analysis, a huge number of data are recorded. As a matter of fact, for each primary beam pulse, the flight time information is split in 50-ps-long channels and then collected and stored in a specific format raw data file. Then, these raw data files can be exported in a general readable format. Moreover, for each ion count, the ToF-SIMS files contain several information, including scan number, primary ion shot number, x and y pixel coordinates of the primary ion beam raster, and ToF channel. Therefore, even a single pixel spectrum can be considered belonging to "big dataset", since it contains an impressive amount of recorded data. In this thesis work, it is demonstrated that a computational method can offer the possibility to a correct classification of single pixel spectra, containing signals which look more like a barcode rather than an interpretable mass spectrum. In particular, the main objective of this chapter is to describe the possible use of a probabilistic neural network in solving problems arising low-counts ToF-SIMS signal processing and pattern recognition.

A PNN is predominantly understood as a classifier since it can map any input pattern to a number of classifications. This neural network method has been chosen thanks to its several advantages. In fact, it can supply a fast-training process and an inherently parallel structure, which allows the convergence to an optimal classifier as the size of the representative training set increases. Moreover, the training samples can be added or removed without extensive retraining. Accordingly, PNNs learn more rapidly than many neural network models and have had success on a variety of applications. Based on these facts and advantages, PNN can be considered as a supervised neural network, capable of system classification and pattern recognition for ToF-SIMS imaging data.

In order to verify the success of this pattern recognition method, four different polymers' single spectra were recorded and used as training for a probabilistic neural network. Once designed and trained, this neural network was able to provide a correct classification of the spectra acquired through an automated procedure. After the acquisition of the single pixel spectra, the presence of a sequence of counts containing a discriminating feature is determined by studying the distribution of the $\Delta m_i$ values in the Fourier transform domain. For a quantitative description of the similarities and differences between spectra from different pixels, skewness, and kurtosis of the probability density distribution of the Fourier transform moduli were selected. Then, the two component vectors were used as an input for the artificial neural network classifier. The procedure is fast and low-demanding

in terms of CPU performances, and it is also able to evaluate the similarity/dissimilarity in the Fourier transform domain of extremely low intensity single pixel spectra.

Overall, this study proves the power of this new data processing method, where a large dataset with a lack of signal intensity was input into the neural network, and for each analysed polymer, a correct classification of single pixel spectra was provided. This was done without pre-treatment of the data, so that biases were removed, and relatively little effort by the analyst. As a result, this probabilistic neural network approach represents an exciting new possibility for ToF-SIMS to analyse previously unmanageable materials.

## 5.2. The Probabilistic Neural Network (PNN)

A probabilistic neural network (PNN) is a unidirectional neural network and represents a special form of Radial Basis Function (RBF) network. It is a powerful instrument to solve classification and pattern recognition problems since its algorithm minimizes the probability of misclassification[8]. Because of the complexity of the theory behind the PNN, a substantial mathematic discussion would be necessary for a deep comprehension of the neural network construction. Since the purpose of this thesis work is the demonstration of the PNN application for polymer identification and not the PNN construction itself, a methodical and robust mathematic support will not be provided in this thesis. However, some base mathematic information will be provided in the following to guide the understanding of this thesis work.

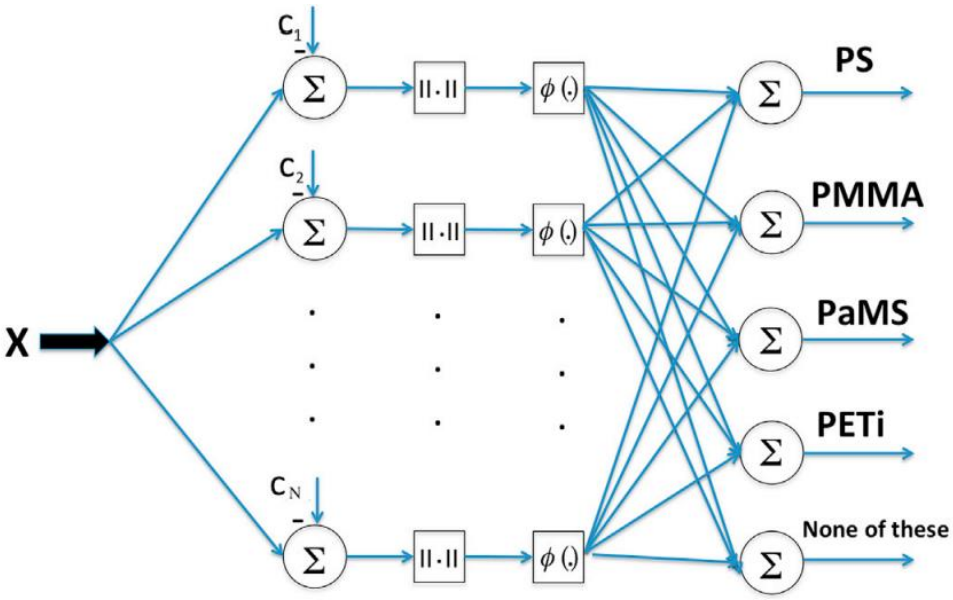


Figure5.1: block diagram of the used neural network.

A PNN consists of several sub-networks, and each sub-network represents a parent probability distribution function (PDF) for each of the investigated classes. The PDF of each class allows to estimate the class probability of a new input data. In PNNs, the operations are organized into a multi-layered feedforward network with a strictly layered structure consisting of a pattern layer, a summation layer, an output layer, and finally an input layer which is always fully connected to the hidden layer because of the computation distance (all coordinates are used to determine the distance). In this case, a specific scheme was employed (showed in figure 5.1) to design the layers:

1. Skewness and kurtosis were used as input for the realization of the input layer.
2. The second layer was composed of 300 neurons activated by Gaussian functions; for the setting of the Gaussians centres (Ci) the train set points were used, which were previously provided by the input layer.
3. The third level performed the average of the second layer outputs for each class.
4. The fourth layer was made of five neurons which were correlated by a linear transfer function; it provided a vote, selecting the largest value.
5. At the end of this procedure the labels were determined for each class[910]

All the no-class-belonging outputs are labelled as “None of these”. As a matter of fact, the PNN training set comprises both spectra subsets belonging to one of the class, and spectra subsets which are different to ones belonging to the polymers we want to classify.
In PNNs, radial basis functions are employed as activation functions. Functions like these can be illustrated by considering a circle. Indeed, a circle is defined as the set of points that have the same fixed distance from a given point. This fixed distance is called the radius of the circle. In the same way, these functions describe a set of output points which have a characteristic distance from the centre. The region hypothetically described by the function assumes an important role in the classification process. In fact, these functions allow the assignment of each neuron to a kind of “catchment region”, which mainly influences the output of the neural network. For this experiment, skewness and kurtosis state the centre of this region. Intuitively, the neuron radial basis function and its parameters determine the “size” of the catchment region of the neuron by specifying how strong the influence of an input vector is depending on its distance from the weight vector described by the radial function.
A Gaussian function was chosen as radial basis function for the neurons, which is explained by equation 5.1:

$$\varphi(r) = e^{-\left(\frac{r}{\sigma}\right)^2}$$

Equation 5.1

This is the so-called simple radial basis function network, in which each training example is covered by its own radial basis function. In other words, the hidden layer contains exactly as many neurons as the training examples. The weights of the connections from the input neurons to the hidden layer neurons are determined by the training examples: each hidden neuron receives a training example and the connection weights given to the hidden neurons are simply initialized with the elements of the input vector of this training example.

Mathematically this can be understood by the following. Let $L_{fixed} = \{l_1,\ldots,l_m\}$ be a fixed learning task with m training patterns $l = (i^{(l)}, o^{(l)})$. Since each pattern is used as the centre of its own radial function, there are m neurons in the hidden layer. Let these neurons be $v_1,\ldots, v_m$, then it is possible to write the equation 5.2:

$$\forall k \in \{1,\ldots, m\}: \quad w_{v_k} = i^{l_k}$$

Equation 5.2

When Gaussian activation function is chosen, like in our case, the radii $\sigma_k$ are often initialized to equal values according to the heuristics in the equation 5.3:

$$\forall k \in \{1,\ldots, m\}: \ \sigma_k = \frac{d_{max}}{\sqrt{2m}}$$

Equation 5.3

where $d_{max}$ is the maximal distance between the input vectors of two training patterns and m is the number of training set spectra. The distance function d is computed with the network input function chosen for the hidden neurons and it expressed by the equation 5.4:

$$d_{max} = \max_{l_j, l_k \in L_{fixed}} d(i^{l_j}, i^{l_k})$$

Equation 5.4

This choice has the advantages that the Gaussian bell curves are not too narrow (there are not isolated peaks in the input space), but also not too wide (there are not peaks overlapping). Since the parameters of the hidden layer (centres and radii) were known, it was possible to calculate the outputs of the hidden neurons for every training example by an iteratively computational process, which allowed to determine the connection weights and the bias values.

Since the network input function is a weighted sum of linear functions (that is its inputs and its activation and output functions), each training example yields for each output neuron one linear function according to equation 5.5:

$$E = \frac{1}{2}\sum_{j=l}^{m}\left(d_j - y_j\right)^2 = \frac{1}{2}\sum_{j=l}^{m} e_j^2$$

$$w_{i,j}^{new} = w_{i,j}^{old} - \eta_1 \frac{\partial E}{\partial w_{i,j}}$$

$$c_i^{new} = c_i^{old} - \eta_2 \frac{\partial E}{\partial c_i}$$

$$\sigma_i^{new} = \sigma_i^{old} - \eta_3 \frac{\partial E}{\partial \sigma_i}$$

Equation 5.5

where $\eta_1$, $\eta_2$ and $\eta_3$ are learning rate coefficients, $\sigma_i$ is the smoothing parameter controlling the spread of the *i*th Gaussian function, $d_j$, e $y_j$ are respectively the desired output and the actual one output obtained from the *j*th spectrum input.

## 5.3. Materials and Methods

Several polymeric thin films were prepared by spin-casting technique. In particular, four polymers were utilized showed in figure 5.2: polystyrene PS, polymethylmethacrylate (PMMA), polyalphamethylstyrene (PaMS), and polyethylenterephthalate-co-isophthalate (PETi) purchased from Source Polymer Inc. (Canada).

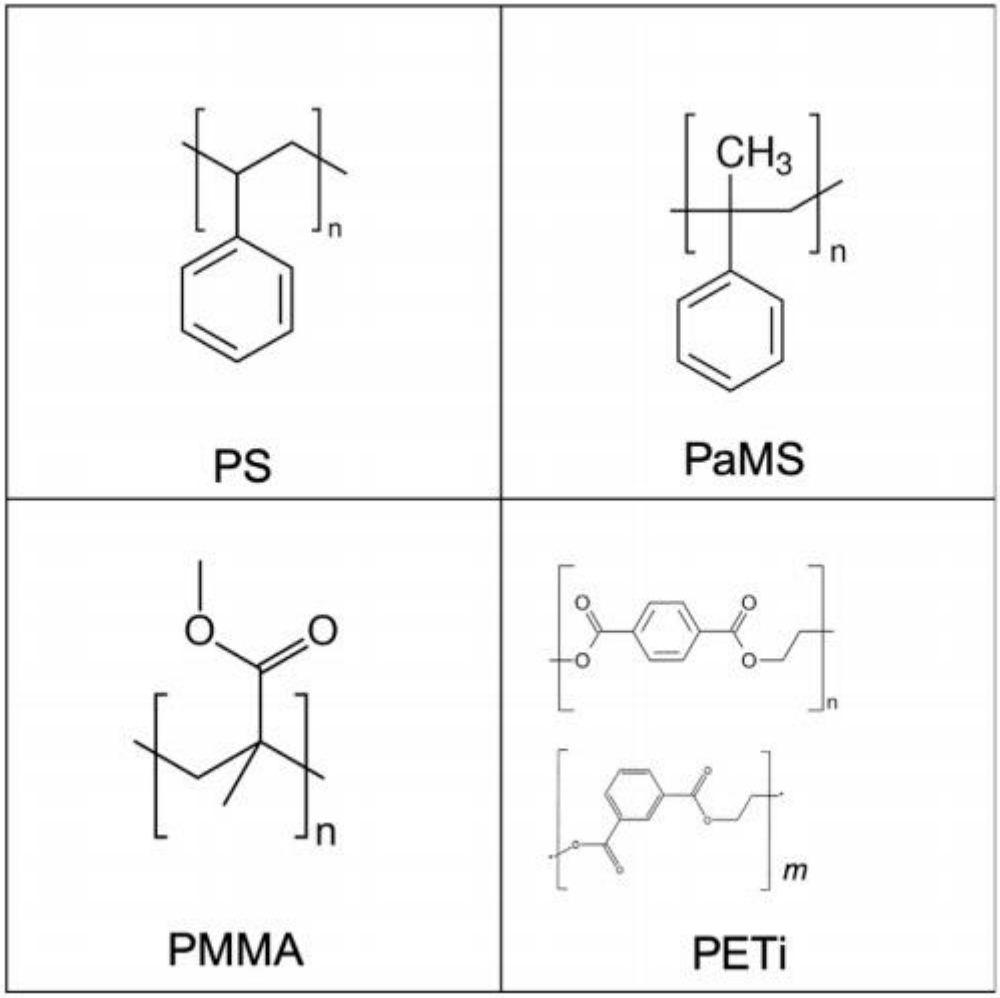


Figure 5.2: chemical structure of PS, (PMMA), (PaMS), and (PETi)

For each polymer, chloroform (Aldrich) solutions 1% w/w were prepared. The solutions were spin coated cast at 1500 rpm with acceleration 2000 rpm/s for 15 s, on Si substrates, which were previously treated with $UVO_3$ for 15 min and rinsed in ethanol (Aldrich).

For the ToF-SIMS analysis $Bi_3^+$ was used as analysing beam (25 keV, 0.1 pA) and for all samples an area of 300 × 300 $\mu m^2$ was investigated (128 × 128 pixel). For each pixel, only one shot was acquired. Low energy electron flooding was used to reduce surface charging. For each polymer film, 5 spectra were acquired. Each spectrum was exported in a generic readable format (ASCII) and handled through a Python script (a registered trademark of the Python Software Foundation). These single pixel spectra were supplied as input to the PNN for the training treatment.

The signal discrimination procedure is based on the presence of specific fragmentation patterns along the spectrum which each material generally gives rise to. In order to extract the chemical information for the signal classification from these very low-count data, it was necessary to perform a careful

analysis of the spectra to recognize the presence of specific counts sequences' repetition, which reveal a discriminating feature of the material. To highlight these features, the Fourier transform was applied on the acquired single pixel spectra. The information containing the specific counts' repetition can be embedded in the symmetry or asymmetry relationships of the distribution of the $\Delta m_i$ values in the Fourier transform domain.

The Fourier transform (FT) is a mathematical operator that decomposes a function (often a function of time, or a signal) into its constituent frequencies. More specifically, the Fourier transform gives rise from a time function to a complex-valued function of frequency, which is described by two factors: the magnitude (absolute value) representing the amount of that frequency present in the original function, and the argument which is the phase of the basic sinusoid in that frequency. Note that for this purpose, only the intensity (modulus) of the Fourier transform was considered, since its argument presents a high level of noise.

Figure 5.3 shows an example of the Fourier series representation of a single pixel ToF-SIMS spectrum (in this case PS spectrum) converted in terms of $\Delta m_i$. As we can see, the data now is described as a sort of Gaussian curve which shows its own distribution of the values around the mean.

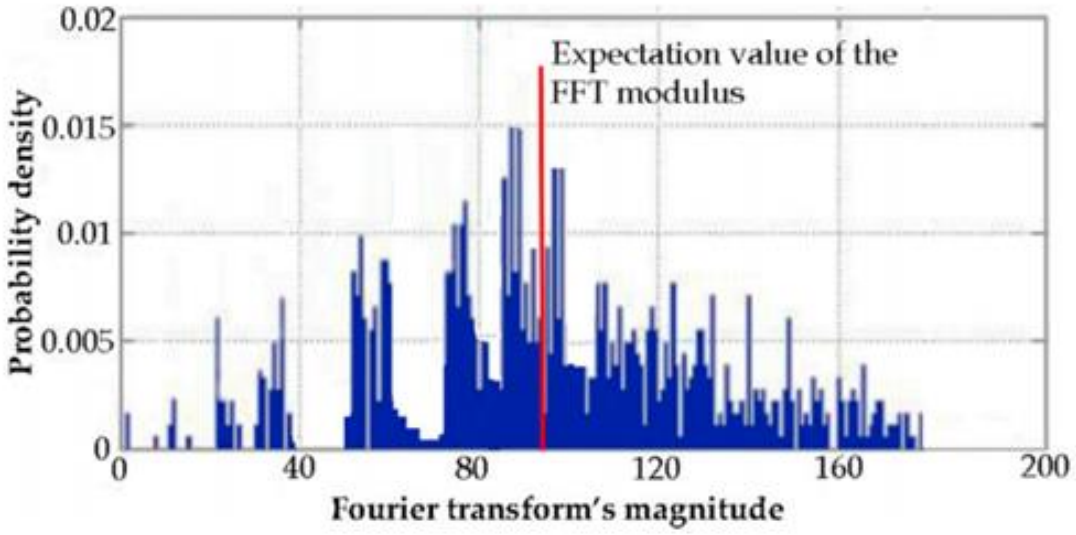


Figure 5.3: Fourier series representation of a PS single pixel ToF-SIMS spectrum

In order to evaluate the differences between these new representations of the data, a quantitative description of these features is necessary. In fact, it is fundamental to find a tool which allows the translation these features from the Fourier transform's domain to the images' pixels. Therefore, skewness, and kurtosis of the probability density distribution of the Fourier transform moduli were calculated to provide a quantitative description of the similarity between different pixels of an image. In fact, the evaluation of a dataset by means of location and variability is performed for almost all the

statistical investigation. For this purpose, in many cases, a further characterization of the data includes skewness and kurtosis.

In probability theory and statistics, skewness is a measure of symmetry, or more precisely, the lack of symmetry of the probability distribution of a real variable around its mean. A distribution, or data set, is symmetric if it looks the same to the left and right of the centre point. Kurtosis is a measure of the "tailedness" of the probability distribution of a real variable, relative to a normal distribution. Both skewness and kurtosis describe the shape of a probability distribution and they can provide a quantification of the theoretical distribution. Data sets with high kurtosis tend to have heavy tails, while data sets with low kurtosis tend to have light tails.

For univariate data $Y_1$, $Y_2$, ..., $Y_N$, the formula for skewness is expressed by equation 5.6:

$$\frac{\sum_{i=1}^{N}\left(Y_i - \overline{Y}\right)^3/N}{s^3}$$

Equation 5.6

where $\overline{Y}$ is the mean, *s* is the standard deviation, and N is the number of data-points. For univariate data $Y_1$, $Y_2$, ..., $Y_N$, the formula for kurtosis is expressed by equation 5.7:

$$\frac{\sum_{i=1}^{N}\left(Y_i - \overline{Y}\right)^4/N}{s^4}$$

Equation 5.7

where $\overline{Y}$ is the mean, *s* is the standard deviation, and N is the number of data-points.

These two vectorial components therefore represent two discriminating features for the different one-pixel count dataset of the four polymers. They represent a tool for the “numerical translation” of the differences in the Fourier transform’s domain. For this reason, they were employed as input for the artificial neural network classification training.

In other words, first the neural network has learned a numerical feature for the recognition of each polymer, which is represented by a certain value of skewness and kurtosis. This numerical feature includes a quite large range of values. This can yield misclassification errors especially in the case of similar datasets, like the ones obtained from polymers. Nevertheless, this approach can furnish useful results for a rapid identification of polymeric mixture.

## 5.3. Results and discussion

In Figure the ToF-SIMS PS 128×128 pixels scan from an area of 300×300 μm$^2$ static spectrum is reported. While it is easy to recognize specific molecular fragments from the spectrum in Figure 5.4

**a)**, it is not possible to identify any characteristic pattern from the spectrum in Figure 5.4 **b)**. Indeed, the signal in the lower spectrum looks more like a barcode rather than an interpretable mass spectrum. As a matter of fact, a correct interpretation of ToF-SIMS data is quite difficult when the signal counts are low. The lack of counts often manifests in the case of 3D analysis. In this type of the acquisition, the use can cause damage within the same which decreases the secondary ions emission and ultimately the intensity counts. Often, this issue is overcome by performing a binning of some neighbouring pixels in order to increase the signal and obtain comprehensible spectra. However, this strategy cannot be applied in the case of structured multi materials samples where each acquired pixel could contain signals from different components. Such binning can also dramatically decrease the lateral resolution, which limits the ability to discriminate between components.

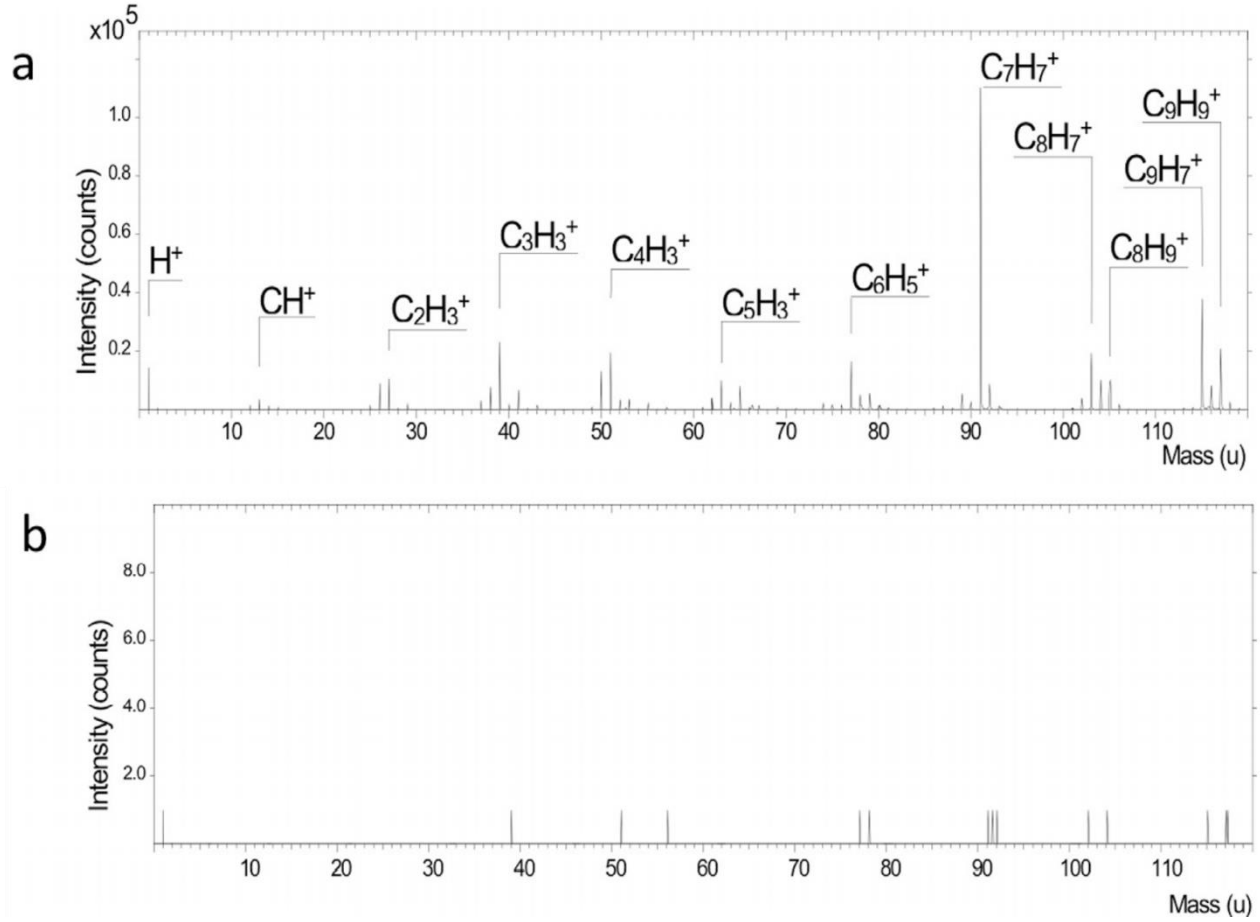


Figure 5.4: a) static mode ToF-SIMS spectrum of Polystyrene. The spectrum is obtained as the sum of the signals originating from 128 × 128 pixels. (b) typical single pixel spectrum

In this experiment, we had to deal with the co-presence of four different polymers. In addition, the PS and PaMS polymers have a remarkably similar chemistry and thus have similar mass spectra. Thus, the PNN approach can be extremely useful for the polymer recognition. In order to train and test the PNN a dataset composed of 450 single-pixel ToF-SIMS spectra was built such as the one reported in (Figure 5.4 **b**). The dataset was organized according to this procedure: from the entire dataset, 200 spectra (50 for each class) were randomly selected in addiction with 100 spectra of other different polymers (complementary class). The testing set consists of 150 spectra (30 for each class including the complementary class) which are not included in the training set.

Indeed, the training set is selected in order to find the model parameters for the neural network, that is, the number of neurons, the smoothing parameters $\sigma_i$ and the network's weights. Once trained, the PNN was tested on the test set, obtaining a misclassification error of 11.7%.

Figure 5.5 displays the decision boundaries for the classification of the four different polymers obtained with the trained network.

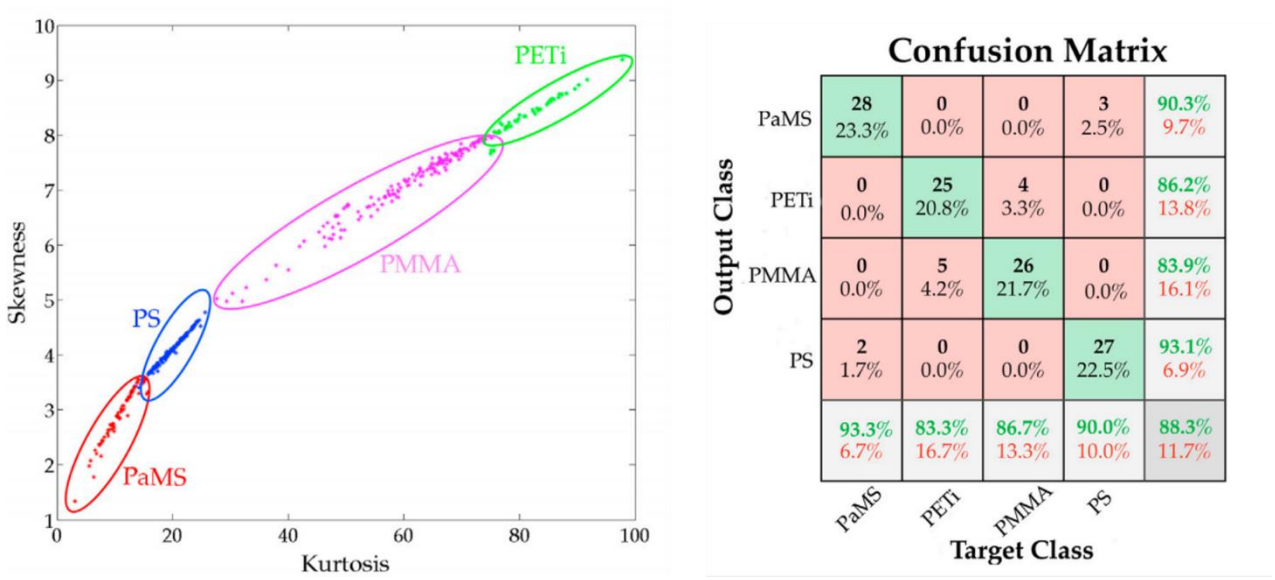


Figure 5.5: The decision boundaries for the classification of the four different polymers obtained with the used neural network (left) and the confusion matrix relative to the results of the neural classification (right).

More explicitly, as we can see from the confusion matrix, the misclassification error contributions come from the network mixing up between PS and PaMs (4.2%) and PETi and PMMA (7.5%) outputs.

Indeed, the misclassification between these two pairs of polymers, PS/PaMS and PETi/PMMA is easily explained from similarities of the polymers' molecular structures. More specifically, PS and PsMS are extremely similar to each other: both do not contain oxygen and simply differ in alpha-positioned methyl compared to phenyl. On the other hand, even though PETi and PMMA are not

particularly similar from a molecular point of view, they show a similar chemical composition, since they contain also oxygen in addition to carbon and hydrogen.

Therefore, we can affirm that this approach is capable of discriminating various polymers with an excellent approximation, simply by analysing the spectrum acquired from a single pixel, despite the scarcity of its data.

Although this thesis reports the PNN application only on polymeric thin films, this approach could be valid even with different chemical nature samples. More in general, the statistical approach can be widely applied to organic, inorganic, hybrid organic-inorganic samples and biological samples.

For the particular case of ToF-SIMS analysis, it could be extremely useful especially for depth profiling and 3D imaging. In fact, depth profiling and 3D imaging produce a huge amount of data, and the application of this method could allow to identify the chemical composition directly from a single pixel spectrum, simplifying and speeding the analyses of laterally structured samples, without any implementation of pixel-binning which would irremediably lower the lateral resolution.

## 5.4. Conclusions

This thesis shows a computer enhanced method capable to easily extract chemical information from single pixel ToF-SIMS spectra. This kind of spectra are not otherwise interpretable since they look like a bar code rather than a mass spectrum. The developed procedure is based on a probabilistic neural network and it operates directly on raw data without any data treatment. It could allow to automate the study of big data from ToF-SIMS analysis acquired in 3D-imaging mode from biological samples or complex hybrid materials of technological interest without any necessity to perform procedures, such as mass-binning, that cause the reduction of the analytical resolution of the technique.

*References*


1. Melissa K Passarelli, Alexander Pirkl, Rudolf Moellers, Dmitry Grinfeld, Felix Kollmer, Rasmus Havelund, Carla F Newman, Peter S Marshall, Henrik Arlinghaus, Morgan R Alexander, Andy West, Stevan Horning, Ewald Niehuis, Alexander Makarov, Colin T Dollery ISG. The 3D OrbiSIMS—label-free metabolic imaging with subcellular lateral resolution and high mass-resolving power. *Nature Methods*. 2017;14:1175–1183. doi:https://doi.org/10.1038/nmeth.4504
2. Demšar U, Harris P, Brunsdon C, Fotheringham AS, McLoone S. Principal Component Analysis on Spatial Data: An Overview. *Annals of the Association of American Geographers*. 2013;103(1):106-128. doi:10.1080/00045608.2012.689236
3. Tuccitto N, Zappalà G, Vitale S, Torrisi A, Licciardello A. A wavelet-PCA method saves high mass resolution information in data treatment of SIMS molecular depth profiles. *Surface and Interface Analysis*. 2016;48(6):317-327. doi:10.1002/sia.5943
4. Madiona RMT, Winkler DA, Muir BW, Pigram PJ. Effect of mass segment size on polymer ToF-SIMS multivariate analysis using a universal data matrix. *Applied Surface Science*. 2019;478(November 2018):465-477. doi:10.1016/j.apsusc.2019.01.242
5. Tuccitto N, Capizzi G, Torrisi A, Licciardello A. Unsupervised Analysis of Big ToF-SIMS Data Sets: A Statistical Pattern Recognition Approach. *Analytical Chemistry*. 2018;90(4):2860-2866. doi:10.1021/acs.analchem.7b05003
6. Heller D, ter Veen R, Hagenhoff B, Engelhard C. Hidden information in principal component analysis of ToF-SIMS data: On the use of correlation loadings for the identification of significant signals and structure elucidation. *Surface and Interface Analysis*. 2017;49(10):1028-1038. doi:10.1002/sia.6269
7. Tuccitto N, Bombace A, Torrisi A, et al. Probabilistic neural network-based classifier of ToF-SIMS single-pixel spectra. *Chemometrics and Intelligent Laboratory Systems*. 2019;191(April):138-142. doi:10.1016/j.chemolab.2019.07.002
8. Kruse R, Borgelt C, Klawonn F, Moewes C, Steinbrecher M, Held P. *Computational Intelligence: A Methodological Introduction*.; 2013. doi:10.1007/978-1-4471-5013-8
9. Testolin A, Zorzi M. Probabilistic models and generative neural networks: Towards an unified framework for modeling normal and impaired neurocognitive functions. *Frontiers in Computational Neuroscience*. 2016;10(JULY):1-9. doi:10.3389/fncom.2016.00073

10. Peng HW, Lee SJ, Lee CH. An oblique elliptical basis function network approach for supervised learning applications. *Applied Soft Computing Journal*. 2017;60:552-563. doi:10.1016/j.asoc.2017.07.019

# 6 Defining Contamination and Sequence of Overlapped Fingerprints by Unsupervised Treatment of Hyperspectral Secondary Ion Mass Spectrometry Dataset

In the previous chapters, a notable number of challenging samples, such as cells, particles for drug delivery, structured or hybrid samples, and cultural heritage objects, have been analysed with ToF-SIMS. Each of these samples represents an objective challenge for chemical imaging, and ToF-SIMS has demonstrated its ability to deal with such complicated analyses. In addition to all of these examples, this chapter will address another successfully applied, but challenging sample for analysis, the chemical imaging of invisible fingerprints. Indeed, ToF-SIMS can provide an enormous amount of forensic information when analysing such a sample and can therefore be fundamental for an investigation. The fingerprints, however, represent a challenge outside of the norm for ToF-SIMS for several reasons. Chemically, a large number of compounds can be present on the fingerprint sample, and oftentimes it is unknown which compounds to search for in the mass spectra. Accurate interpretation can be overwhelming. In addition to the challenge of identification, acquisition of the spectra for an entire fingerprint is problematic. An entire print covers an area in the millimetre scale. In comparison, typical ToF-SIMS analyses are acquired up to the micron scale. Having the instrumentation be able to accurately map the fingerprint without drifting is therefore vital. Finally, since the image will be made of thousands of pixels, the size of the dataset for such a large area will require a computational protocol to handle such complicated task.

Fingerprints originate from the friction of cutaneous finger crests to a surface because the physical secretions produced by cutaneous glands leave a strictly defined pattern. Dactyloscopy is the forensic chemistry technique[1] which studies the identification of minuscule conic papillae, which form thin crests divided by subtle furrows. Crests leave curves, bows and vortices, and have dimensions and relative distance characteristic of each human finger. For this reason, already at the end of 19th century it was clear that fingerprints are individual anatomic features.

Even though the major component of the glands' secretion is water, also inorganic, and organic substances are present in the surface of fingerprints. These substances can include drugs, physical signs, gun and explosive residues, poisons, and arsons. Thus, they can reveal what an individual has recently handled, and their detection can be fundamental in a forensic investigation. Fingerprints can be either visible prints, which are left because of the presence of coloured substances such as blood, ink, pollutants or other chemicals, or invisible prints which require specific treatments in order to be

revealed by specific substances. The choice of the revealing substance must be accurate to avoid damaging the surface on which the process needs being carried out. Unfortunately, many of these methods can destroy the trace because of the chemicals involved.

For this reason, another strategy has recently been experimented – using investigation techniques capable of performing a chemical imaging of latent fingerprints and collect their molecular signals. Mass spectrometry imaging techniques are strongly suited to accomplish this purpose. As a matter of fact, this approach is becoming increasingly more established, due to the enormous amount of forensic information that can potentially be extracted by using mass spectrometry techniques[2,3,4]. Among these, ToF-SIMS has been successfully applied for chemical imaging of invisible fingerprints on banknotes[5], to identify illicit drugs on fingerprints[6], as well as their dating age, following the diffusion of organic molecules or the chronology of the deposition on questioned printed documents , etc[7, 8].

Nevertheless, fingerprints imaging analysis can be difficult, since these traces cover such a large area of surface. When the spatial distribution of the analytes in the sample is much larger than the typical raster size of a ToF-SIMS primary ion beam, the acquisition of the images can be arduous. In order to solve this problem, some modern instruments, such as ToF-SIMS, provide macroraster mode that enable imaging analysis of such large areas. Despite the possibility that macroraster mode can offer, this kind of acquisition yields a huge amount of data, whose handling is almost impossible by the typical commercial software furnished by the vendors. Thus, these kinds of dataset require specific postprocessing treatments.

Recently techniques for automating data treatment have become increasingly popular. As previously discussed, the most common unsupervised approach to deal with big datasets is based on Principal Component Analysis, which is nowadays considered a standard protocol. In fact, it is now included in the vendors software dedicated to ToF-SIMS instruments. Meanwhile, the application of artificial intelligence and machine learning to ToF-SIMS data has received extensive attention over recent years[9]. Self-organizing map (SOM)[10], t-distributed stochastic neighbour embedding (t-SNE) and uniform manifold approximation and projection (UMAP)[11] have been applied to ToF-SIMS dataset to reduce the dimensions producing so-called similarity maps. In the literature, the ability of these methodologies to handle the complexity and dimension of such data sets has already been shown[12]. However, these methodologies have been applied to datasets with relatively small size in terms of pixels, although extraordinarily complex in terms of chemical composition. This thesis work presents a new strategy to deal whit big dataset, based on a preliminary training of the neural network on a binned dataset.

## 6.1. Thesis work

As stated previously, fingerprints represent an objectively challenging sample for analysis. In fact, the secretions left by the hands are a complex chemical mixture and thus many molecules with different chemical nature are present on the surface of fingerprints. Moreover, on the hands it is possible to find some residual substances coming from the products that have been handled during the day. Therefore, this chemical mixture is for the most part unknown.

Moreover, human fingerprints do not belong to the micro or nano categories of samples. Indeed, their prints are enough large to cover an area of millimetres. Most imaging techniques have been developed and designed in order to visualize objects under the micrometre scale. Therefore, the areal dimension of fingerprints is quite larger than usual samples analysed by imaging techniques. These instrumental issues in most cases can be easily overcome, however, this is not always true for the handling of the big dataset that can be obtained from such sample sizes. In this thesis work, it will be shown that ToF-SIMS imaging of overlapped fingerprints via macroraster modality yields a huge dataset which cannot be handled by the common software provided by the vendor. Moreover, the macroraster modality ToF-SIMS imaging requires long timescales to perform the analysis. These times prevent to acquisition of sufficient scans to obtain high intensities. Therefore, the images will contain insufficient counts and statistics.

In this thesis work, it will be demonstrated that relevant information can still be extracted from big datasets having poor statistics, such as those obtained from analyses performed in macroraster mode. The method involves first training a neural network on a binned dataset. This binning is required so that sufficient signal is present in the pixels so the network can be trained. However, using the binned dataset leads to a loss of lateral resolution. Therefore, the trained neural network is reapplied back to the original, non-binned dataset that contains the high lateral resolution data. The method has been applied to samples of relevant forensic interest, in this case fingerprints. However, this methodology can be exploited to other imaging experiments, such as 3D imaging analysis of biological samples for which the statistics are poor. Oftentimes, it is not possible to accumulate many scans for biological samples, since avoiding the of accumulation of damage is a priority. In this case, this new methodology could be used to enhance the signals obtained for such experiments. Thus, this technique of training the neural network represents an exciting new methodology for generating relevant information from previously considered poor or unusable analyses.

## 6.2. Uniform Manifold Approximation and Projection (UMAP) Mathematical Bases

For more than a decade, t-Distributed Stochastic Neighbour Embedding (tSNE) has been one of the most widely used dimensionality reduction techniques. However, Uniform Manifold Approximation and Projection (UMAP), which is based on Riemannian geometry and algebraic topology, has recently emerged as an alternative to t-SNE, offering better efficiency and applicability. In fact, recently it became a popular nonlinear dimensionality reduction technique[13]. UMAP stands out for its fast computation time. It is approximately three times faster than tSNE implementation and has a better stability between runs. It also has support for non-metric distance measures, such as the cosine distance and correlation distance. Since its introduction, UMAP has been quickly adopted by diverse disciplines, such as life sciences, physics, and computer science, attesting to its powerful performances.

In this thesis work UMAP is applied for the data reduction of ToF-SIMS imaging in macroraster modality of fingerprints. UMAP is used to extract certain parameters from each datapoint in the original dataset. These parameters, which represent the original data, are then projected in a lower dimensional space. In this way, it is possible to evaluate and discriminate each point of the dataset in a space with less dimensions. A detailed description of the underlying mathematics related to UMAP can be found in the literature[11]. Briefly, the algorithm first constructs a fuzzy topological representation of the dataset, then it optimizes the low dimensional representation to have as close a fuzzy topological representation as possible, measured by cross entropy. Although UMAP is grounded in a complex mathematical foundation, in the following paragraph a brief mathematic description is provided, in order to understand how this algorithm works.

The UMAP computation method can be divided into two parts. The first part aims to calculate the numerical features of each datapoint, which are then projected for a graph construction. The second part deals with the optimization of the computed parameters, in order to minimize the loss of information caused by the passage to a lowdimensional space. UMAP starts by generating a weighted k-nearest neighbour graph that describes the distances between the data points in the high-dimensional space. Given an input dataset $X = \{x_1,..., x_N\}$, defined are $k$, the number of neighbours to consider, and $d$, the distance metric. UMAP first computes $N_i$ , which is the $k$-nearest neighbours of $x_i$ respect to $d$. Then, UMAP computes two parameters, $\rho_i$ and $\sigma_i$ , for each data point $x_i$ in order to identify two numerical values which represent its local metric space. $\rho_i$ is a nonzero distance from $x_i$ to its nearest neighbour, and it is obtained according to Equation 6.1:

$$\rho_i = \min_{j \in Ni}\{d(xi, x\,j) \mid d(xi, x\,j) > 0\}$$

Equation 6.1

$\sigma_i$ must satisfy the condition below (Equation 6.2) and it is found using binary search:

$$\sum_{j \in Ni} \frac{\exp(-\max(0, d(xi, x\,j) - \rho i)}{\sigma i} = \log_2(k)$$

Equation 6.2

Using $\rho_i$ and $\sigma_i$ , UMAP computes $v_{j|i}$, which is the weight of the edge from a point $x_i$ to another point $x_j$. As well as for $v_{j|i}$, $v_{i|j}$ indicates the weight of the edge from point $x_j$ to point $x_i$. They are calculated according to Equation 6.3:

$$v\,j|i = \exp\frac{(-\max(0, d(xi, x\,j) - \rho i)}{\sigma i})$$

Equation 6.3

In order to obtain a symmetric result, UMAP computes a single edge combining the resulting weights of $v\,j|i$ and $vi|j$, according to equation 6.4:

$$v_{ij} = v_{j|i} + v_{i|j} - v_{j|i} \cdot v_{i|j}$$

Equation 6.4

The resulting parameter, $v_{ij}$, indicates the similarity between points $x_i$ and $x_j$ in the original space. Let $y_i$ be the projection of $x_i$ in a lowdimensional projection space. The similarity between two projected points $y_i$ and $y_j$ is given by equation 6.5:

$$w_{ij} = (1 + a||yi - y\,j||_2^{2b})^{-1}$$

Equation 6.5

where a and b are positive constants defined by the user. Then, it is necessary optimize the differences between the original space and the new lowdimensional space, or rather, UMAP has to find the $y_i$ that minimizes the difference (or loss) between $v_{i\,j}$ and $w_{i\,j}$. For accomplishing this, UMAP measures the cross entropy between $v_{i\,j}$ and $w_{i\,j}$ (equation 6.6):

$$C_{UMAP} = \sum_{i \neq j} [vi\,j \cdot \log(\frac{vi\,j}{wi\,j}) - (1 - vi\,j) \cdot \log(\frac{1 - vi\,j}{1 - wi\,j})]$$

Equation 6.6

Therefore, $y_i$ will be initialized through spectral embedding and iteratively optimized to minimize $C_{UMAP}$. The result of this computing procedure is 2D and 3D-coloured maps where the datapoints are localized according their similarity or dissimilarity.

## 6.3. Materials and Methods

The fingerprints used in this study were impressed on a Si surface from two volunteers. Purposely, the prints were partially overlapped to test the ability of the network to discriminate between them. Without any further treatment, the sample was analysed by ToF-SIMS. High-mass resolution static SIMS images were acquired with a TOF-SIMS IV spectrometer (ION-TOF) using a $Bi^+$ analysis beam (bunched mode, 25 KeV, ~0.1 pA, 256×256 pixels, single scan rastered over 500 µm × 500 µm, PI fluence < $3\times10^{11}$ ions×$cm^{-2}$). In order to analyse both fingerprints a macroraster modality was executed by collecting 30 × 30 stacked single raster scans, thus 15 mm × 15 mm was investigated. The workstation used was equipped with 16 cores i9 9900K processors and 256 GB of RAM. Datasets were exported from SurfaceLab software (IONTOF GmbH) to General Raw Data format and imported into Python 3.8 based scripts developed in our lab. NumPy was imported as linear algebra library, Matplotlib for data plotting, PIL for image editing and umap-learn for Uniform Manifold Approximation and Projection. The Python based "pseudo code" is reported below:

```
import umap
import numpy as np

def rebin(arr, new_shape):
    """Rebin 2D array arr to shape new_shape by averaging."""
    shape = (new_shape[0], arr.shape[0] // new_shape[0],
             new_shape[1], arr.shape[1] // new_shape[1])
    return arr.reshape(shape).mean(-1).mean(1)

 """load dataset"""
x = np.load('foo.npy').astype(np.uint8)
x = x.reshape(7000,7000,518)

"""binning dataset"""
binning_to = int(700) #binning factor
y = np.zeros((binning_to,binning_to,518))
for i in range (518):
```

```
    print (i)
    y[:,:,i]=rebin(x[:,:,i], (binning_to,binning_to))
y = y.reshape(binning_to**2,518)

"""learn on binned dataset"""
mapper = umap.UMAP(n_neighbors = 15, n_components=3, low_memory=True,
metric='cosine',init = 'spectral', spread = 1.0, min_dist = 0.1, verbose = 'true').fit(y)

"""transform NON binned dataset"""
x = x.reshape(7000*7000,518)
transformed = np.zeros((7000**2,3))
for i in range(0,1000*7000,100000):
       transformed[start*7000+i:start*7000+i+100000,:]=
mapper.transform(x[i:i+100000,:])
```

## 6.4. Results and Discussion

Figure 6.1 **a)** shows the spectrum of total ions relative to the sum of all the scans that make up the macroraster. Significant peaks up to *m/z* of about 400 are present. In particular, 518 peaks were identified in the spectrum, which were used to compose a dedicated peak list. Figure 6.1 **b)** shows the total ion map of the macroraster represented by 49 million pixels (7000 x 7000). Hence, a multispectral analysis of the raw file builds a data matrix consisting of 49 million times 518 elements. Such size falls within the category of big data and requires special data processing to handle the dimensions.

On the other hand, by looking at the colour bar in Figure 6.1 **b)** it is possible to notice that the maximum total intensity per single pixel of all integrated 518 sectors does not exceed 100 counts. This indicates that while the data to be processed is exceptionally large, the signal is very weak and does not have sufficient statistics. In fact, the typical spectrum of the signal acquired from a single pixel reports only single counts, as shown in Figure 6.1 **c)**. The statistical analysis shown in Figure 6.1 **d)** reveals that for the majority of the pixels, a maximum of a single count is obtained from integration of all 518 peaks. An example of this problem is shown in Figure 6.1 **e)** which displays the false-colour map associated with the signal integration of the peak assigned to carbon. Despite being one of the most intense peaks in the total ion spectrum (see Figure 6.1 **a)**), the image is in black and white because the counts are often either null (black colour) or unitary (white colours). This is a quite common condition when dealing with ToF-SIMS data acquired by means of macroraster or during 3D imaging with dual-beam mode of organic-based samples. In both these cases in fact, the acquisition time is compressed in order to either avoid damage accumulation phenomena and/or

decrease time duration needed for the entire analysis. This reduction of the acquisition time forces the operator to make conservative choices that create problems in the post-acquisition data investigation.

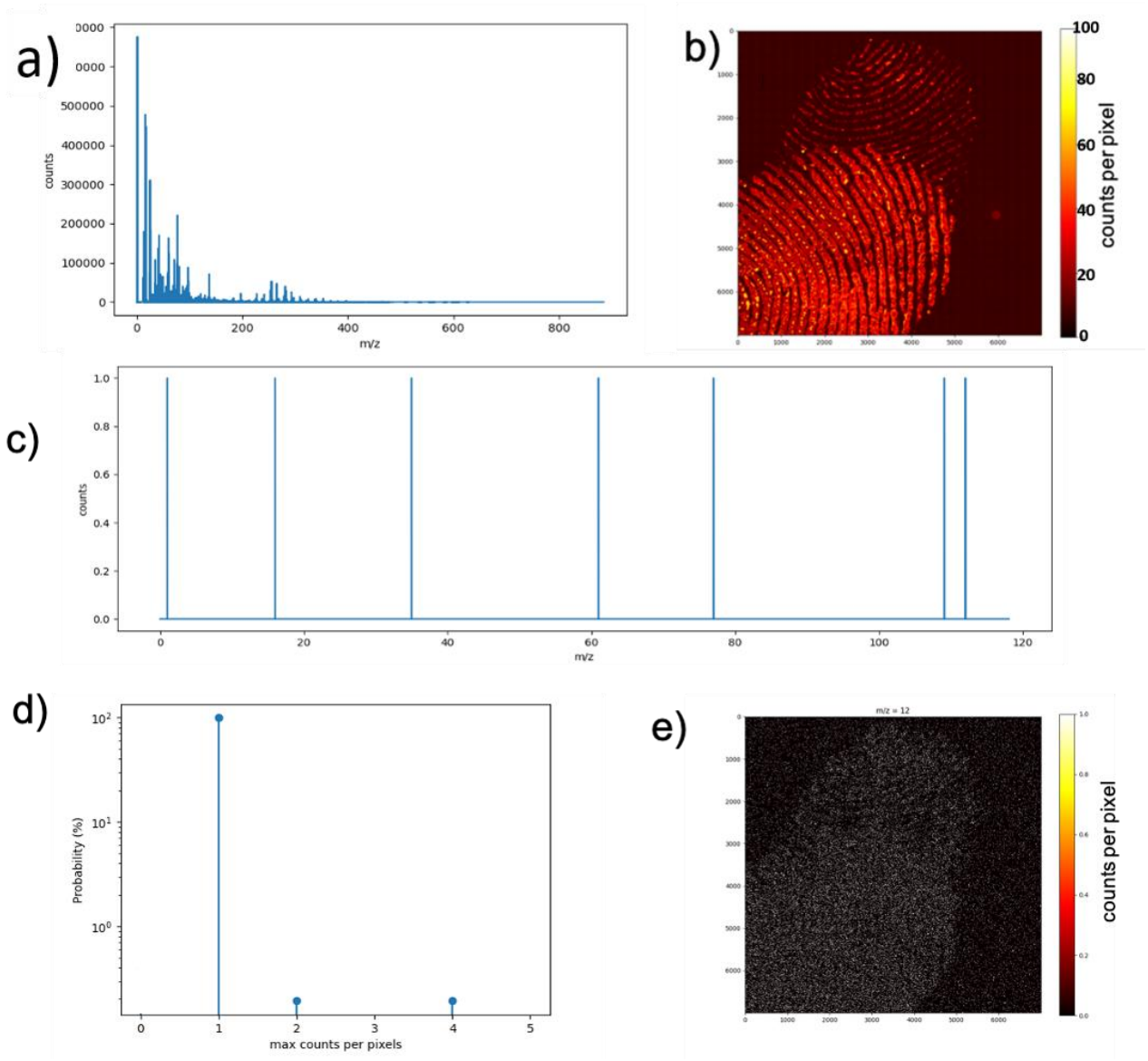


Figure 6.1: **a)** mass spectra of total ion count for the macroraster. **b)** total ion map for the fingerprint sample. **c)** typical spectra for a single pixel. **d)** statistical analysis of the number of counts acquired in individual pixels**. e)** signal integration for C peak for all pixels.

One solution could be to use analysis conditions that enhance the yield of secondary ions. Some examples have been reported in the literature. These include the enhancement of the secondary ion yield by means of reactive gases[14], metal nanoparticles[15], primary reactive beams[16], and others. However, these protocols are not always applicable since they are largely influenced by the chemical nature of the sample under investigation, and satisfactory results are not a guarantee. Hence, the most reliable procedure for increasing the secondary ion signal without relying on changes to the sample

or analysis environment is through post-analysis data treatment. In this study, the approach was to perform a binning of neighbouring pixels. This procedure aims to accumulate statistically significant signal by exploiting the information coming from the surrounding pixels and recalibrate an individual pixel with this additional signal.

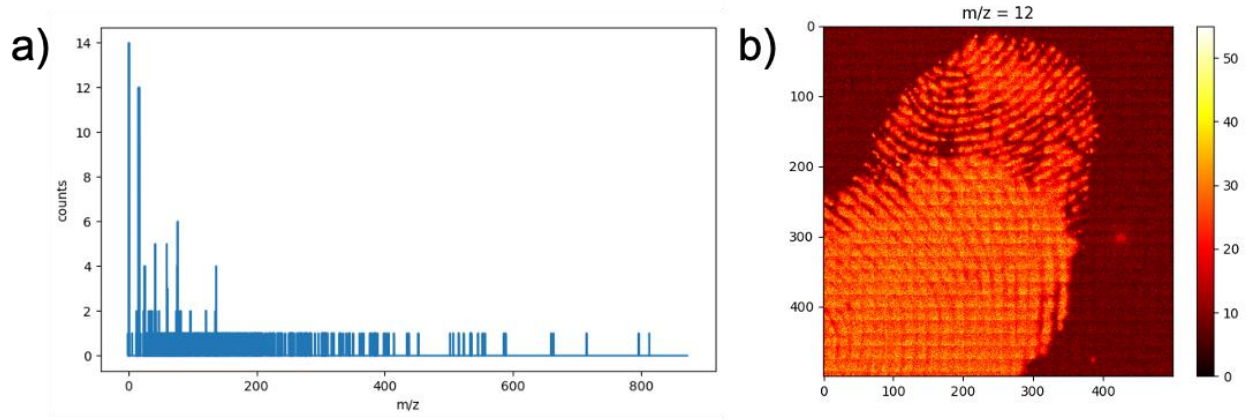


Figure 6.2: a) mass spectra of a 10x10 pixel binning. b) false color image after binning is applied to all pixels.

Figure 6.2 **a)** shows the spectrum related to a binning of 10×10 neighbouring pixels. The spectrum now appears richer in counts and looks much less like an unintelligible barcode. Figure 6.2 **b)** shows the false-colour image relative to the integration of the peak assigned to the C, which has the centre at *m/z* = 12. When comparing this image to the original un-binned image shown in Figure 6.1 **e)**, it is possible to notice that Figure 6.2 **a)** is undoubtedly richer in statistically relevant information. Overall, the binning procedure generates multispectral data matrices that are less massive and, at the same time, richer in useful information for data processing. On the other hand, pixel binning leads to a loss of lateral resolution, nullifying the high spatial resolution capabilities that ToF-SIMS could offer.
This thesis work demonstrates a new and exciting strategy based on machine learning methodologies to boost the signal intensity of a large dataset and generate an intelligible interpretation of the acquired data. Since the raw data was statistically poor, the pixel binning process results were used to enable the training of the neural network in order to then correctly recognize and clusterize the original non-binned data. Thus, the lateral resolution of the non-binned data was not sacrificed. The procedure is schematized in Figure 6.3.

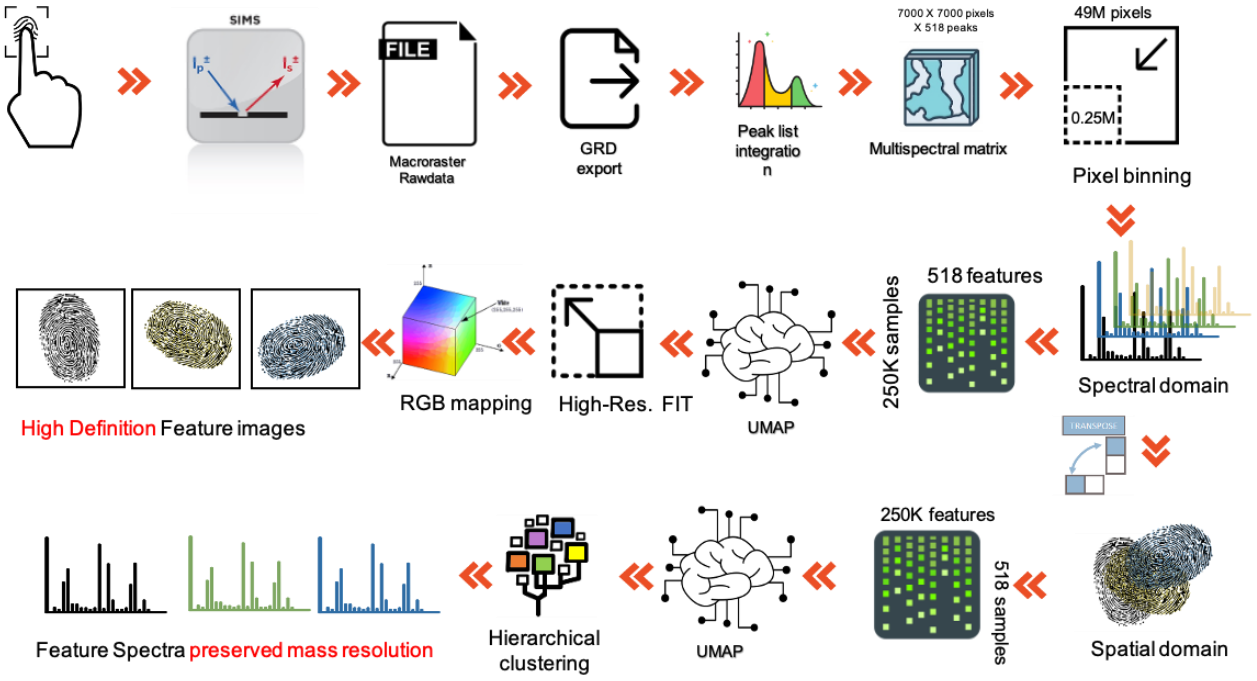


Figure 6.3: iconographic representation of the proposed data treatment method

First, the sample containing the fingerprints was analysed according to the macroraster procedure to obtain the raw data. The raw data was exported in a format readable by non-proprietary vendor software (nominally GRD)[17]. The total ion spectrum was summed (Figure 6.1 **a)**) and a peak list containing 518 peaks was assembled. The peak list integration gave rise to a hyperspectral array. Each of the 518 maps was binned by summing the data from neighbouring pixels, in order to reduce the size of the hyperspectral images from 49M pixels to 250K pixels (for example see Figure 6.2 **b)**). The binned matrix was then subjected to dimensional reduction in the mass domain (the time-of-flight) and, after transposition, in the spatial domain (the pixels). A manifold learning technique for dimension reduction called UMAP (Uniform Manifold Approximation and Projection) was employed for these purposes.

Uniform Manifold Approximation and Projection (UMAP) is a dimension reduction technique that can be used for visualisation, but it can also be used for general non-linear dimension reduction. Indeed, UMAP was recently applied to non-linear dimension reduction of hyperspectral data gathered from some mass spectrometry techniques, including ToF-SIMS[13]. A detailed description of the underlying mathematics related to UMAP can be found in [11]. In brief, the algorithm first constructs a fuzzy topological representation of the dataset, then it optimizes the lower dimensional representations to match. In this way, it was possible to apply a reduction in the mass domain up to three embeddings. The trained neural network was used to back fit the non-binned dataset. As a result, high-resolution similarity maps were achieved, showed in colour scale (RGB) mapping. Only two embeddings were sufficient for reduction in the spatial domain. Using a hierarchical clustering

algorithm, it was possible to map in false colours the peaks belonging to each cluster. Similar to the mass domain, the trained neural network enabled the reconstruction of the characteristic spectra for each cluster. The output is the product between the percentage belonging to the cluster (identified by the hierarchical algorithm), and the counts of the non-binned dataset.

Figure 6.4 **a)** shows the three-dimensional projection of the 49 million pixels resulting from UMAP embedding. It is evident that three dimensions are sufficient to identify four clusters. These four clusters of data are represented with a specific colour, in the RGB mapping, and each pixel belongs to one of these clusters. Three clusters are well-separated (green, blue, and light pink colour) while a fourth cluster (red) links the other three in the three-dimensional projection map. Since the index of each pixel in the dataset is known, it is possible to reconstruct similarity maps in false colours.

Figure 6.4 **b)** shows the reconstruction of the non-binned dataset. It is clear that this approach recognized the presence of two fingerprints characterized by different chemical features (specified by blue and light pink colour) placed on a substrate (green colour). Moreover, the lateral resolution is maintained, and it is possible to inspect in detail complex portions of the sample even in areas where the two fingerprints are overlapped. Figure 6.4 **c)**, for instance, shows one portion. By properly separating the colour channels it is possible to have a greater detail of the 4 clusters, as displayed in Figure 6.4 **d)**. In fact, that the fingerprint assigned to the blue colour is unequivocally placed under the other assigned to the light pink colour. The pixels clustered and represented by red are related to areas belonging to both of the fingerprints that probably have a similar, non-discriminable chemical composition.

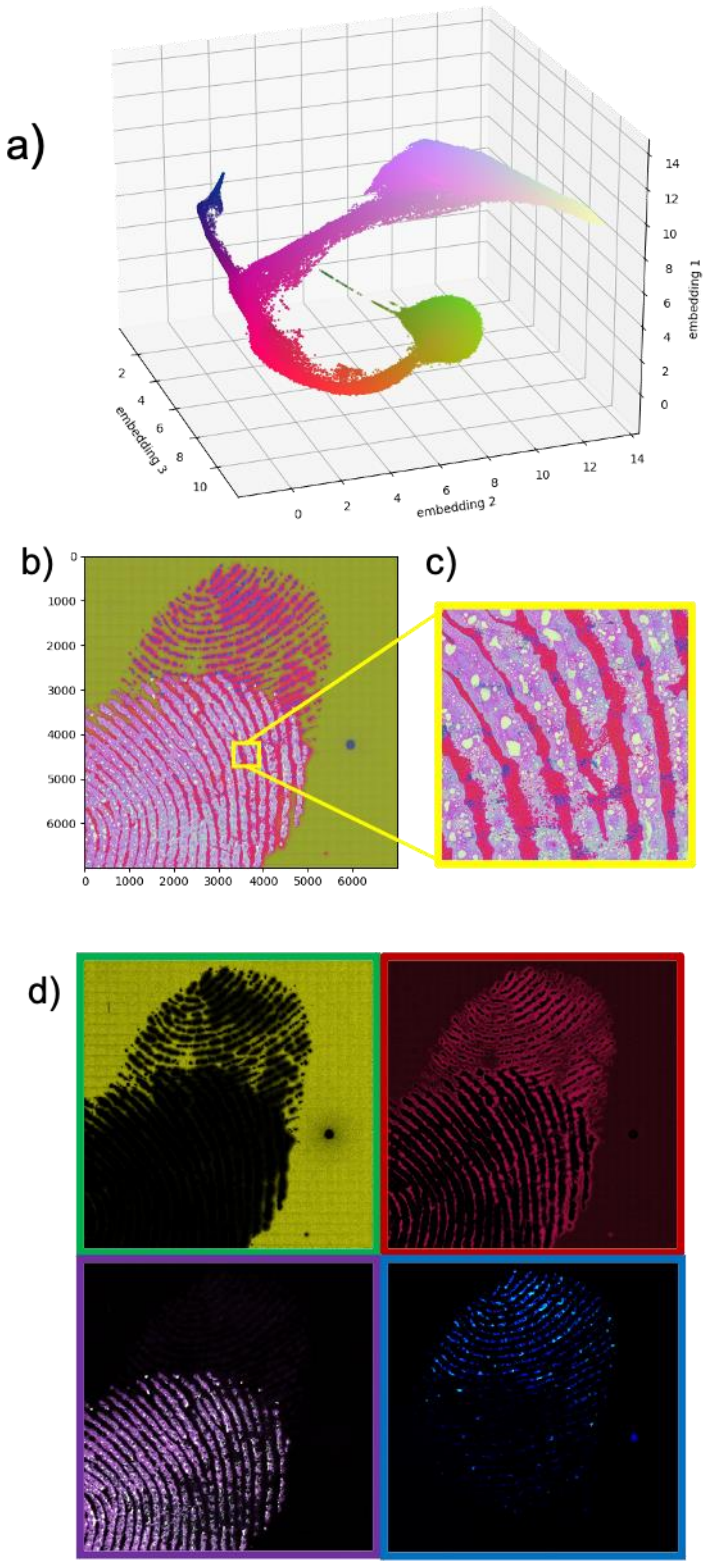


Figure 6.4: **a)** three-dimensional projection of the 49 million pixels as resulting from UMAP embedding **b)** false color image of the non-binned dataset coloring each pixel according to a RGB mapping of the 3 embeddings scaled normalizing between 0 and 255, **c)** zoomed portion of yellow portion, **d)** false color images of the non-binned dataset.

Figure 6.5 **a)** displays the two-dimensional embedding of the processed dataset after matrix transposition. We can see that the 518 selected values are divided in clusters and plotted with different colours, blue, pink, green and orange. In addition, the grey colour represents the noisy points which were not clustered by the algorithm.

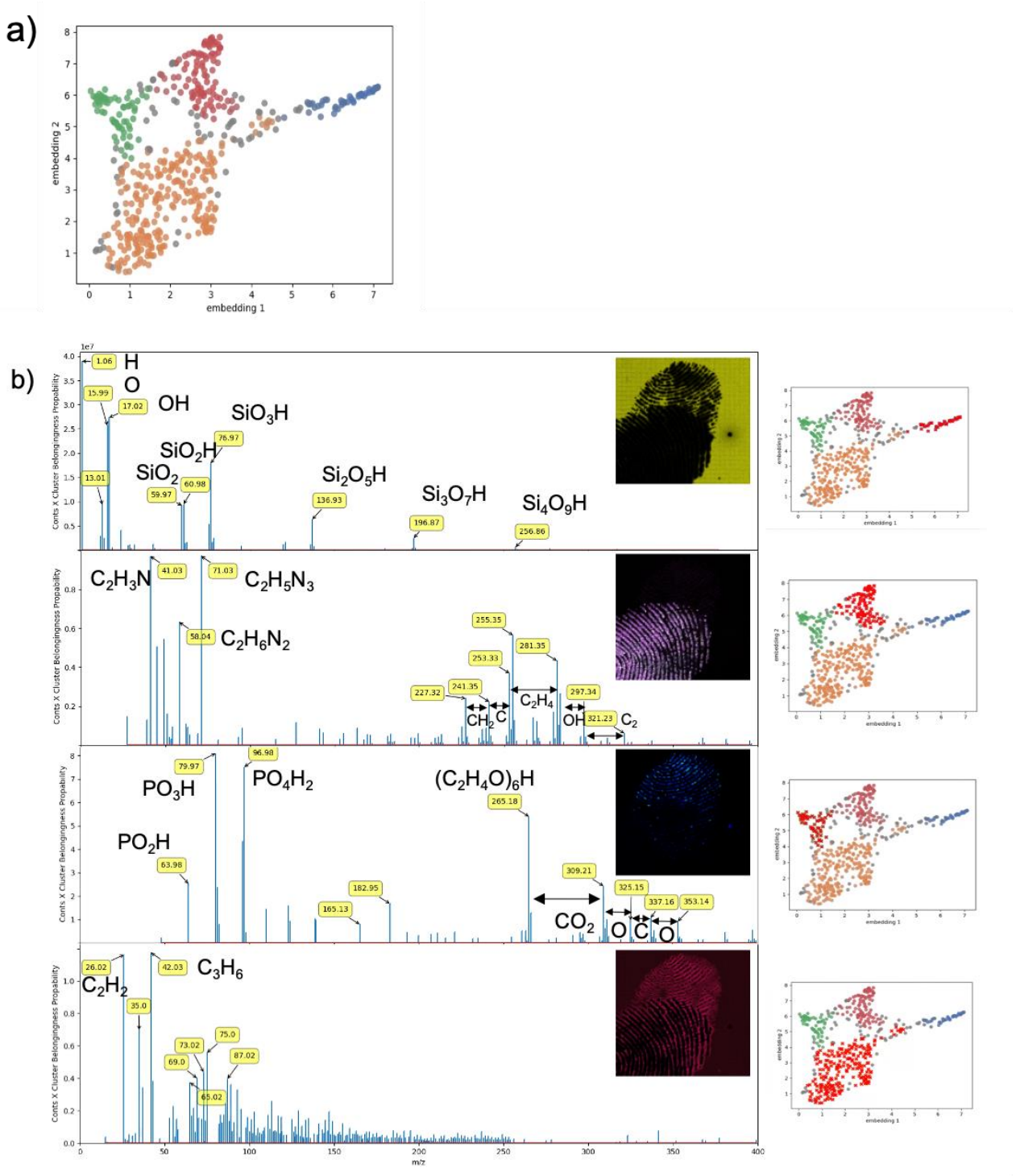


Figure 6.5: **a)** two-dimensional embedding of the transposed dataset, colour represents the belonging to a cluster as evaluated by the hierarchical clustering algorithm, **b)** mass spectra relative to each cluster coloured in red in the right panels and the corresponding false-colour map as depicted in Figure 6.4 d)

Figure 6.5 **b)** shows the mass spectra relative to each cluster and the corresponding false-colour map. Therefore, each cluster contains mass values which are characteristic of a certain area of the sample. The assignment of the peaks allowed the characterization of the chemical composition of the different areas. In particular:

- The blue cluster values belong to the pixels having the mass spectrum of the substrate (i.e., silicon oxide-based glass).
- The pink cluster values describe one fingerprint (coloured in violet in the false-colour map), which has characteristic peaks at low masses, assigned to nitrogen-containing organic fragments, and at high masses (between 250 and 350 m/z). These last peaks at high *m/z* show differences in masses assigned to small organic fragments.
- The green cluster contains mass values belonging to the other fingerprint (coloured in blue in the false-colour map), which presents a very peculiar mass spectrum characterized by peaks assigned to fragments of compounds containing phosphate ions at masses below 100, and fragments of compounds based on oligomers of ethylene oxide, a component normally used in cosmetics.
- The area clustered with the orange colour has a characteristic spectrum rich in high masses peaks and presents some hydrocarbon fragments peaks at low masses, confirming that these are not strongly discriminating zones.

A comparative analysis to databases or a more detailed assignment of the characteristic fragments of the various clusters would shed light on the origin of these chemical features. However, this rigorous forensic investigation was not the aim of this work. Here, the demonstration of the successful methodology or tool to enhance the sensitivity in ToF-SIMS and utilize the neural network to discriminate the features was the main goal. These results demonstrate that this bigdata processing procedure is applicable in an unsupervised mode to ToF-SIMS datasets, derived from analysis with high mass resolution and pixel definition in the order of tens of Megapixels. The only choice left to the analyst is the extent of binning between neighbouring pixels.

In fact, this binning parameter fact affects how UMAP balances local versus global structure in the data. It does this by constraining the size of the local neighbourhood UMAP will utilize when attempting to learn the manifold structure of the data. This means that low values of n neighbours will force UMAP to concentrate on very local structure. On the other hand, large values will push UMAP to look at larger neighbourhoods and lose the fine detail structure for the sake of the broader description of the data.

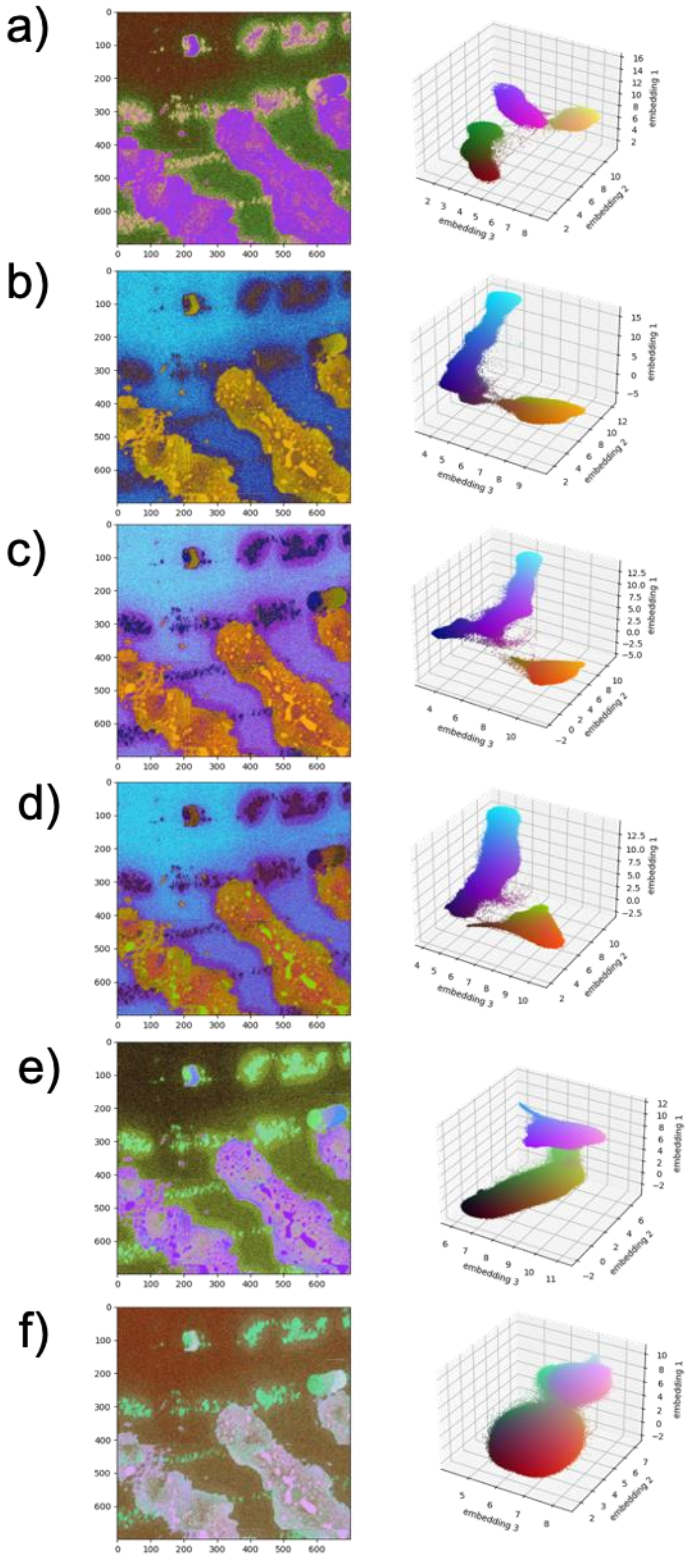


Figure 1: False colour image of a portion of the image with binning a) 70 × 70, b) 35 × 35, c) 14 × 14, d) 9 × 9, e) 4 × 4, f) 2 × 2

As a demonstration, Figure 6 shows the performance of this methodology for the same fingerprint dataset with neural networks trained by different binning levels. The results show that excessive compression of the initial data leads to a loss of the information needed to discriminate each

fingerprint. Indeed, by performing a strong binning between nearby pixels (Figure 6.6 **a)** 70×70 or Figure 6.6 **b)** 35×35) the neural network is able to discriminate the substrate pixels from the fingerprints. However, it is not able to distinguish between the fingerprints. By performing a coarser binning, the results are unsuitable for an appropriate training of the network since the initial data is poor in statistics (Figures 6.6 **c)** and **d)**, 14×14 and 9×9, respectfully). Figures 6.6 **e)** and **f)** show that by decreasing the binning to 4×4 or 2×2, the distribution of the dots in the 3D-embedding plot is very scattered. Thus, the substrate cannot be discriminated from the two fingerprints.

Therefore, the best condition is at intermediate binning values around 14×14, reducing the 7000×7000 whole hyperspectral images to 500×500. This value is utilized throughout the study shown above. Nevertheless, this value is sample-dependent and for any dataset the proper one must be found. Currently, a unique protocol is being developed. However, the procedure is easily automated, and the user can choose judiciously which is the best level of binning for his purposes in the same way as it is typically done applying any other compression methodology.

## 6.5. Conclusions

In this work, a new approach for big data treatment is presented based on data dimensional reductional algorithm. The uniform manifold approximation and projection (UMAP) algorithm was successfully applied on the dataset obtained from overlapped fingerprints acquired via ToF-SIMS macroraster imaging. As is known, macroraster mode enables imaging on an area much larger of the normal ToF-SIMS raster size. However, this larger raster area gives rise to huge dataset which cannot be interpreted with normal data processing protocols. The UMAP algorithm enabled the use of the big dataset obtained from two overlapped fingerprints and was able to extract important information from the sample. By a judicious extension of neighbouring pixel binning, it was possible to train a neural network with much smaller size dataset in order to prepare it for the discrimination of features in the true big dataset. Thanks to the embedding maps it was possible to “clusterize” a peak list of 518 *m/z* values and distinguish four areas of different chemical composition in the macroraster image. The spectra in each area of the image confirmed the obtained chemical features. In this way, the two fingerprints’ pixels were identified and compositionally characterized, as well as for the substrate. In fact, characteristic fragments were assigned to each component of the image. Moreover, it was possible to demonstrate that the best protocol performance was achieved with an intermediate binning values, but this choice can be different for each sample. Nevertheless, the procedure is easily automated, it can be applied beyond the fingerprint analysis in this study.

*References*


1. Vimi S. Mutalik, Aparna Menon, N. Jayalakshmi, Asha Kamath ARR. Utility of cheiloscopy, rugoscopy, and dactyloscopy for human identification in a defined cohort. *J Forensic Dent Sci*. 2013;5((1)):2–6. doi:doi: 10.4103/0975-1475.114535
2. Bai MJ. imaging of developed fingerprints using mass spectrometry imaging. *Analyst*. 2013;138(21):6246. doi:doi: 10.1039/c3an01204b.
3. R. Bradshaw, G. Wilson, N. Denison, and S. Francese. Application of MALDI MS imaging after sequential processing of latent fingermarks. *Forensic Sci*. 2021;319:110-643. doi:doi: 10.1016/j.forsciint.2020.110643.
4. Gorka, M. Augsburger, A. Thomas and AB. Molecular composition of fingermarks: Assessment of the intra- and inter-variability in a small group of donors using MALDI-MSI. *Forensic Chem*. 2019;12:99–106. doi:doi: 10.1016/j.forc.2018.12.002.
5. W.-J. LI, L.-H. SUN, W. YOU, L.-X. WANG, Y.-B. ZHAO, and Z.-P. LI. Chemical Imaging of Fingerprint on RMB Banknotes Using Time-of-Flight Secondary Ion Mass Spectrometry. *Anal Chem Chinese J*. 2020;48(11):1511–1518. doi:doi: 10.1016/S1872-2040(20)60059-7.
6. Muramoto, T. P. Forbes, A. C. van Asten, and G. Gillen. Test Sample for the Spatially Resolved Quantification of Illicit Drugs on Fingerprints Using Imaging Mass Spectrometry. *Anal Chem*. 2015;87(10):5444–5450. doi:doi: 10.1021/acs.analchem.5b01060.
7. S. Muramoto and E. Sisco. Strategies for Potential Age Dating of Fingerprints through the Diffusion of Sebum Molecules on a Nonporous Surface Analyzed Using Time-of-Flight Secondary Ion Mass Spectrometry. *Anal Chem*. 2015;87(16):8035–8038. doi:doi: 10.1021/acs.analchem.5b02018.
8. N. Attard-Montalto et al. Determining the chronology of deposition of natural fingermarks and inks on paper using secondary ion mass spectrometry. *Analyst*. 2014;139(18):4641–4653,. doi:doi: 10.1039/c4an00811a.
9. R. M. T. Madiona, D. A. Winkler, B. W. Muir, and P. J. Pigram. Optimal machine learning models for robust materials classification using ToF-SIMS data. *Appl Surf Sci*. 2019;487:773–783. doi:doi: 10.1016/j.apsusc.2019.05.123.
10. W. Gardner et al. Self-Organizing Map and Relational Perspective Mapping for the Accurate Visualization of High-Dimensional Hyperspectral Data. *Analytical Chemistry*. 2020;92(15):10450–10459. doi:doi: 10.1021/acs.analchem.0c00986.
11. McInnes L, Healy J, Saul N, Großberger L. UMAP: Uniform Manifold Approximation and Projection. *Journal of Open Source Software*. 2018;3(29):861. doi:10.21105/joss.00861

12. Tuccitto N, Bombace A, Torrisi A, et al. Probabilistic neural network-based classifier of ToF-SIMS single-pixel spectra. *Chemometrics and Intelligent Laboratory Systems*. 2019;191(April):138-142. doi:10.1016/j.chemolab.2019.07.002
13. Smets T, Verbeeck N, Claesen M, et al. Evaluation of Distance Metrics and Spatial Autocorrelation in Uniform Manifold Approximation and Projection Applied to Mass Spectrometry Imaging Data. *Analytical Chemistry*. 2019;91(9):5706-5714. doi:10.1021/acs.analchem.8b05827
14. G. Zappalà, V. Motta, N. Tuccitto, S. Vitale, A. Torrisi, and A. Licciardello. Nitric oxide assisted C 60 secondary ion mass spectrometry for molecular depth profiling of polyelectrolyte multilayers. *Rapid Commun Mass Spectrom*. 2015;29(23):2204–2210. doi:doi: 10.1002/rcm.7383
15. A. Marcus and N. Winograd. Metal nanoparticle deposition for TOF-SIMS signal enhancement of polymers. *Anal Chem*. 2006;78(1):141–148. doi:doi: 10.1021/ac0513921.
16. S. Sheraz, A. Barber, I. B. Razo, J. S. Fletcher, N. P. Lockyer, and J. C. Vickerman. Prospect of increasing secondary ion yields in ToF-SIMS using water cluster primary ion beams in Surface and Interface Analysis,. 2014;46(1):51–53,. doi:doi: 10.1002/sia.5606.
17. Wegnüller U, Werner C, Strozzi T, Wiesmann A, Frey O, Santoro M. Sentinel-1 Support in the GAMMA Software. *Procedia Computer Science*. 2016;100:1305-1312. doi:10.1016/j.procs.2016.09.246

# General Conclusions

The overall theme of this thesis project aimed at developing 3D and 2D characterization of non-conventional samples using ToF-SIMS. For this reason, some non-conventional "model" samples were selected in order to be investigated, and were chosen for the specific role in their respective application field. As a matter of fact, the strength of ToF-SIMS characterization in terms of the knowledge it can provide within these fields, and how it could be used to fill the gaps in the literature, was the driving force behind these efforts.

All the characterized samples had micrometre scale structures, which normally can be visualized by using electronic microscopies. These microscopic techniques provide optical information about a sample but omit any molecular information. Meanwhile, techniques which give the possibility to combine chemical mapping in the microscopy techniques, only provide elemental and not molecular information. By ToF-SIMS analysis, it was possible to extract molecular information thanks to the high mass resolution, as well as to study samples structure morphologies thanks to the high spatial resolution.

Moreover, the issue of big data handling was addressed. As a matter of fact, ToF-SIMS gives rise to hyperspectral images which represent a challenge dimension data-file for many software. For this reason, today more than ever, the imaging needs the support of computational and programming science. Many strategies, such as Principal Component Analysis or Machine Learning algorithms have been developed aiming to decrease the number of the file variables or reducing the data dimension. This thesis work has presented some computational data handling approaches which can be successfully applied for ToF-SIMS imaging datasets.

The first work in this thesis presented a demonstration of Solid Lipid Nanoparticles (SLNs) imaging. SLNs are lipidic particles used in drug delivery to release drugs in human body. In fact, they are generally loaded with pharmaceutic molecules and produced as aqueous solution by adding surfactants as stabilizers. This specific sample was characterized by the presence of an anti-inflammatory molecule PEA and a lipidic core structure. The particles dimension was around 2 microns. Considering the minimal literature focusing on this recent topic, filling the gaps especially in the chemical structure is essential to advancing the SLNs use.

In fact, spatial characterization could assist in the improvement of their design and consequently of their efficiency. ToF-SIMS surface analyses have been already reported in literature with successful results for efficiency evaluation. However, no ToF-SIMS imaging characterizations have been carried out. Therefore, this is the first specific study on ToF-SIMS imaging, and it has shown the usefulness of the knowledge obtained from this technique. For this study, a specific method for the sample

preparation was developed, avoiding the agglomeration phenomenon, and thus achieving single particles dispersed in a solid matrix. Typically, they are only stabilized in aqueous solution which is unsuitable for ultra-high vacuum. The use of trehalose "imprisoned" particles in a solid sample matrix, suitable for ultra-high vacuum. Both 3D and 2D high lateral resolution images were successfully carried out, which let us examine particles structure in space. Indeed, it was possible to detect some signals which are characteristic of the sample components and also detect the molecular peak of the drug inside the particles. Notwithstanding, this sample shows an extraordinarily complex matrix, whose composition is covered up by industrial patent and is made up of several mixtures of different chemical substances.

The second topic presented in this thesis was the use of ToF-SIMS analysis within the field of cultural heritage. As part of a research project submitted by LAMS (Laboratoire D'archéologie Moléculaire Et Structurale) led by Dr Alain Brunelle, ToF-SIMS characterization of dyes stemming from ancient $19^{th}$ century textiles was performed. In the field of cultural heritage, the sample preparation assumes a vital role. Dealing with valuable cultural heritage, often fragile, and limited in availability, it is essential that minimal sample fragments are used in order to preserve the integrity of the precious objects. To achieve this aim, ToF-SIMS is convenient because its high sensitivity precludes the need for large sample quantities. Moreover, ToF-SIMS allows the identification of molecular signals even when chemical composition is unknown, thanks to its high mass resolution. These advantages were essential to reveal and identify the chemical nature of the dyes. In addition, by using the multivariate analyses, it was possible to discover the ancient dying technique performed on these textiles. This research project and its successful results were presented in October 2019, during the $22^{nd}$ International SIMS Conference (SIMS 22) in Kyoto, Japan.

In the fourth chapter, a PET-PC blend ToF-SIMS study is shown. This polymeric blend has been extensively studied and nowadays the physical-chemical properties, as well as the miscibility conditions are known. Despite this system is not new, this chapter presents a novel investigation procedure. In fact, temperature-induced aging experiments are often carried out on polymeric blends (or more in general on materials) registering the results only before and after the procedure. In this thesis work, ToF-SIMS imaging was applied for a temperature programmed experiment which allowed to monitor in real-time the modification occurred on the blend surface. In particular, for the experiment presented in this thesis, the blend was prepared by spin-coating and it shows characteristic structured morphologies typical for this system. The obtained structures' changes were monitored during the whole temperature programmed experiment. This allowed to observe two different $T_g$ corresponding to those of the homopolymers, and to verify that no blending actually occurred, because of the absence of transesterification reactions. The results obtained through temperature

programmed ToF-SIMS imaging testify the capability of this technique for the investigation of material surface modification and demonstrate the interesting prospective of future applications for various organic structured systems.

The following chapter presented the application of a probabilistic neural network (PNN) for the identification of polymers. This approach provided the extraction of latent chemical information from ToF-SIMS data, working on uncompressed and un-binned raw data sets. It was demonstrated that this computational method, opportunely designed and trained, was capable of distinguishing and classifying four different polymers by recognizing some characteristic sequences of counts from their single pixel spectra. This approach could enable automated study of big data from ToF-SIMS analysis from other 3D-imaging analyses, such as biological samples or complex hybrid materials. It thus represents an exciting potential for ToF-SIMS to rapidly advance knowledge of these materials of technological interest, without any necessity to upgrade the instrumentation or alter the samples prior to study.

The last work presented in this thesis deals with the detection of contaminants on fingerprints with ToF-SIMS by means of an unsupervised machine learning treatment. Fingerprints represent an objective challenging sample because the human secretions left by the hands are a complex chemical mixture in addition to any residues from what a person has handled. Since fingerprints are enough large to cover an area of millimetres, macroraster analysis has to be performed. This in turn generates large hyperspectral files which are problematic with typical data processing. Therefore, a method to both boost the low sensitivity within the data acquisition, as well as interpret a big dataset, was developed. For this thesis work two overlapped fingerprints were analysed by ToF-SIMS in macroraster modality, obtaining an image of 49000×49000 pixels. The uniform manifold approximation and projection (UMAP) algorithm was successfully applied to reduce the dataset size so that a neural network could be trained. Once the training was completed, this network was capable of identifying like-mass spectra on the un-binned data, and discriminate the features and chemistry of each fingerprint on the sample substrate. The result is extremely promising for any number of ToF-SIMS applications, because it is capable of turning previously unusable data into an accurate intelligible characterization.

These results presented in this thesis work aimed to demonstrate that, among other imaging techniques, ToF-SIMS is quite versatile and can be utilized to advance the understand of materials many application fields. Despite the age of this technique and its widespread use in the literature, there are still unexplored fields of investigation in which ToF-SIMS can reveal information which could not be extracted by other techniques. Moreover, the support that computational methods can

provide to this technique, results in a powerful tool for imaging, which can be applied for any kind of challenging samples.